Czech Technical University in Prague

Faculty of Nuclear Sciences and Physical Engineering

Diffractive Processes in Antiproton-Proton Collisions at $\sqrt{s} = 1.96$ TeV in the DØ Experiment

Roman Otec

Doctoral Thesis

2006

Declaration

This thesis is the result of my own work, except where explicit reference is made to the work of others, and has not been submitted for another qualification to this or any other university.

Roman Otec

Diffractive Processes in Antiproton-Proton Collisions at $\sqrt{s} = 1.96$ TeV in the DØ Experiment

Roman Otec
Czech Technical University in Prague
Faculty of Nuclear Sciences and Physical Engineering

Supervisor: Vladislav Šimák

Abstract

A first study of single diffractive central high-p_T dijet events in $p\bar{p}$ collisions at center-of-mass energy $\sqrt{s}$ = 1.96 TeV is presented, using data recorded by the D0 detector at the Tevatron during RunIIa in 2002-2004. The total integrated luminosity corresponding to the data sample is 398 pb^{-1}. A diffractive sample is selected using a rapidity gap approach.

A precise definition of the rapidity gap constitutes the first part of the thesis. The rapidity gap is defined by means of two parts of the D0 detector - luminosity detectors and calorimeter. Luminosity detectors serve as a basic indicators of diffractive candidates and the calorimeter is used to confirm the low energy activity in the forward region (a rapidity gap). Presented studies of energy deposited in forward part of calorimeter by various types of events yield two rapidity gap definitions. Both of them use a fixed rapidity interval in calorimeter $|\eta| \in [2.6, 5.2]$ and introduce an upper limit on the energy deposited in this region. First definition, which corresponds to the lowest systematical errors, uses a limit of 10 GeV, an energy limit in the second definition is set to 3 GeV. This alternative definition corresponds to the lowest contamination of diffractive sample by non-diffractive events, on the other hand it is accompanied with rejection of high percentage of diffractive candidates.

Using the gap definition dijet diffractive data are then selected and compared to inclusive dijet events in various distributions. The main focus is to measure the difference in azimuthal angles between two leading jets in events with at least two high p_T central jets. This variable is sensitive to the dynamics of the process.

Indeed, the results show the different behaviour of $\Delta\phi$ distributions between the inclusive and diffractive samples. It is also shown that this difference is bigger for lower p_T jets.

Other distributions presented in the thesis show that most of the properties are the same for inclusive and diffractive events. The only observed difference is in the transversal properties of the jets, which could be explained as that diffractive jets are narrower than inclusive ones.

Results are compared to Monte Carlo Pomwig (for diffractive sample) and Herwig (for inclusive sample); both show a good agreement with the data.

Acknowledgment

The physical analyses of high energy physics are not possible without the contribution of many people. Therefore I would like to thank all people of the D0 collaboration at Fermilab. Without their hard work in designing, building and running the experiment, it would not have been possible to write this thesis. Especially, I would like to thank Duncan Brown, Christophe Royon, Andrew Brandt, Alexandr Kupčo or Brendan Casey, who directly led me through the understanding of detector and the physical analysis.

I would also like to thank Stanislav Pospíšil, who brought me into the world of experimental physics and really helped me at the beginning of my Ph.D. study.

In the end, I would like to thank my supervisor Vladislav Šimák, for his great support in my entire study, for giving me a chance to cooperate with the D0 experiment and for his help during the analysis.

This work is dedicated to my parents Irena Otcová and Jiří Otec, for their great, unselfish support and patience during my studies.

Contents

List of Figures

List of Tables

Chapter 1

Introduction

Understanding of nature has interested mankind since long ago. The main attention was always focused on astronomical observations and predictions but since the time of ancient Greece, philosophers have been trying to answer also basic questions about the structure of matter and forces acting between objects. Already at that time, philosophers like Epicurus, Democritus or Leucippus (5th to 3rd century BC) proposed that the matter consists of *atoms* - the smallest, indivisible parts of world, configurations and movements of which form everything in the world. This idea is believed to be right up to the present day. Even though there were other theories in the course of time, which dominated over the atomistic view[1], the systematic work of physicists (e.g. monumental work *Philosophiae Naturalis Principia Mathematica* by Isaac Newton, but many others as well) and mainly the developments of electromagnetism, radioactivity or atomic structure, and new experimental methods and equipment during 20th century have allowed physicists to extend the Democritus picture of the world in terms of elementary particles.

Nowadays understanding of nature is that matter is made up of 6 quarks, 6 leptons (electron, muon, tau and corresponding neutrinos) and their associated antiparticles. There are three types of forces - electroweak, strong and gravitational, each of which acts between different types of objects, at different distances and strengths, mediated by different particles. While gravitation is described by a standalone theory of relativity, the strong force is described by a comprehensive theory of Quantum Chromodynamics (QCD), now the most accepted theory of particle physics. This theory has excellent results in predictions of observations of high energy particle experiments. One area of interest physics, is *diffractive physics* via the

[1] Mainly the Aristotle's idea (3rd century BC) that all matter consists of four elements: earth, water, air and fire. This was accepted until approximately 16th century AD.

strong interaction.

Diffractive processes were experimentally first observed by experiments at HERA collider (e.g. [11, 12]) and experiment UA8 at CERN (e.g. [13, 14]), but they had been studied already before. Diffractive physics introduces for example interactions, in which two hadrons interact strongly with each other, yet one or both particles survive intact. It is possible to tag the diffractive events by detecting of these particles. At the D0 experiment a new detector subsystem - Forward Proton Detector (FPD) - has been installed to perform measurements of protons or antiprotons going out of the interaction under very small angles. Thus it provides a way to reconstruct the full kinematics of the diffractive events. At the time of writing of this thesis the FPD was not fully operational.

The most widespread approach to tag diffractive events is searching for a rapidity gap, or a region of low particle activity. It is a feature of a diffraction that comes from the diffractive event topology (see Chapter 2), and is used also in this thesis.

The goal of the dissertation is to provide a precise definition of such a rapidity gap for Run II data at the D0 experiment by means of the calorimeter and luminosity detectors. Using this definition dijet diffractive data are then selected and compared to inclusive dijet events in various distributions. The main focus was to measure the difference in azimuthal angles between two leading jets in events with at least two high p_T central jets.

The structure of the thesis is as follows. Chapter 2 contains a short overview of diffractive physics and kinematics, and of Regge theory. It also introduces experimental methods of jet physics. In Chapter 3.1, the description of the D0 detector subsystems with emphasis on the calorimeter is given. Chapter 4 shows the data selection and efficiency studies of kinematic cuts. Next chapter presents the derivation of the rapidity gap definition and Chapter 6 shows the comparison of $\Delta\phi$ distributions of diffractive and inclusive samples. The Pomwig Monte Carlo Event Generator is described and compared with diffractive data in Chapter 7. Several other physical distributions are shown in Chapter 8 and a precise description of luminosity measurement method at D0 is presented as an Appendix.

Chapter 2

Theoretical Framework

Since first particle experiments started, there has been a long way in searching for a theory, which would explain the fundamental properties of matter and basic forces. The current understanding of the particle world is combined in a compact form known as the Standard Model. This theory explains many aspects of measured properties for a lot of processes. While the precision of predictions is amazing for a big number of interactions, there are still areas that are less understood. One of them is diffractive physics in hadron-hadron interactions, which this thesis is focused on.

2.1 Diffraction

Diffraction in hadron-hadron interactions is usually defined as a process in which an object with the quantum numbers of the vacuum[1] is exchanged. The exchanged object is generally referred to as the *pomeron*. Diffractive processes contribute around 40% of the total cross-section as observed at the Tevatron [32]. Therefore it is necessary to understand these types of processes to have a complete theory.

A basic division of such processes is to *elastic* and *diffractive* scattering. A diffractive dissociation can be subdivided into *single diffraction*, *double diffraction* and *double pomeron exchange*. This is summarized in Fig. 2.1.

Elastic scattering: both incoming particles stay intact and no additional particles occur in the final state

$$a + b \rightarrow a + b$$

[1] no charge, no colour, zero spin, isospin and baryon number

Single diffraction: one of the incoming particles escapes from the collision scattered under small angle, the other dissociates into a cluster of final state particles,

$$a + b \rightarrow a + X$$

Double diffraction: pomeron is exchanged and both particles dissociate into two particle clusters,

$$a + b \rightarrow X + Y$$

Double pomeron exchange: a cluster of particles is produced in the center of the interaction

$$a + b \rightarrow a + b + X$$

Another possible division of diffractive processes is according to the final states of the interaction into *soft* (no jets or other hard objects in the final state) and *hard* (one or more jets in the final state) diffraction.

2.1.1 Scattering and the Cross Section

A generic 2→2 particle interaction is schematically plotted in Fig. 2.2. Two particles 1 and 2 collide and after the interaction two (generally different) particles 3 and 4 are produced. There are several kinematical Lorentz-invariant variables suitable for a description of a general 2→2 physical process. Using the four-momenta of the initial and final beam particles p_1 - p_4, we define the following Mandelstam variables:

$$\begin{aligned} s &\equiv (p_1 + p_2)^2 = (p_3 + p_4)^2 \\ t &\equiv (p_1 - p_3)^2 = (p_2 - p_4)^2 \end{aligned} \tag{2.1}$$

Variable s represents a center-of-mass energy squared, t is the negative square of the four-momentum transfer. The variables s and t are usually accompanied by a third variable $u \equiv (p_1 - p_4)^2 = (p_2 - p_3)^2$, which is dependent on the previous two through equation

$$s + t + u = \sum m_i^2$$

where the sum goes over all four particles.

One of the most important properties of a process, is its differential and total *cross-section*. It is related to the probability that the interaction can occur and

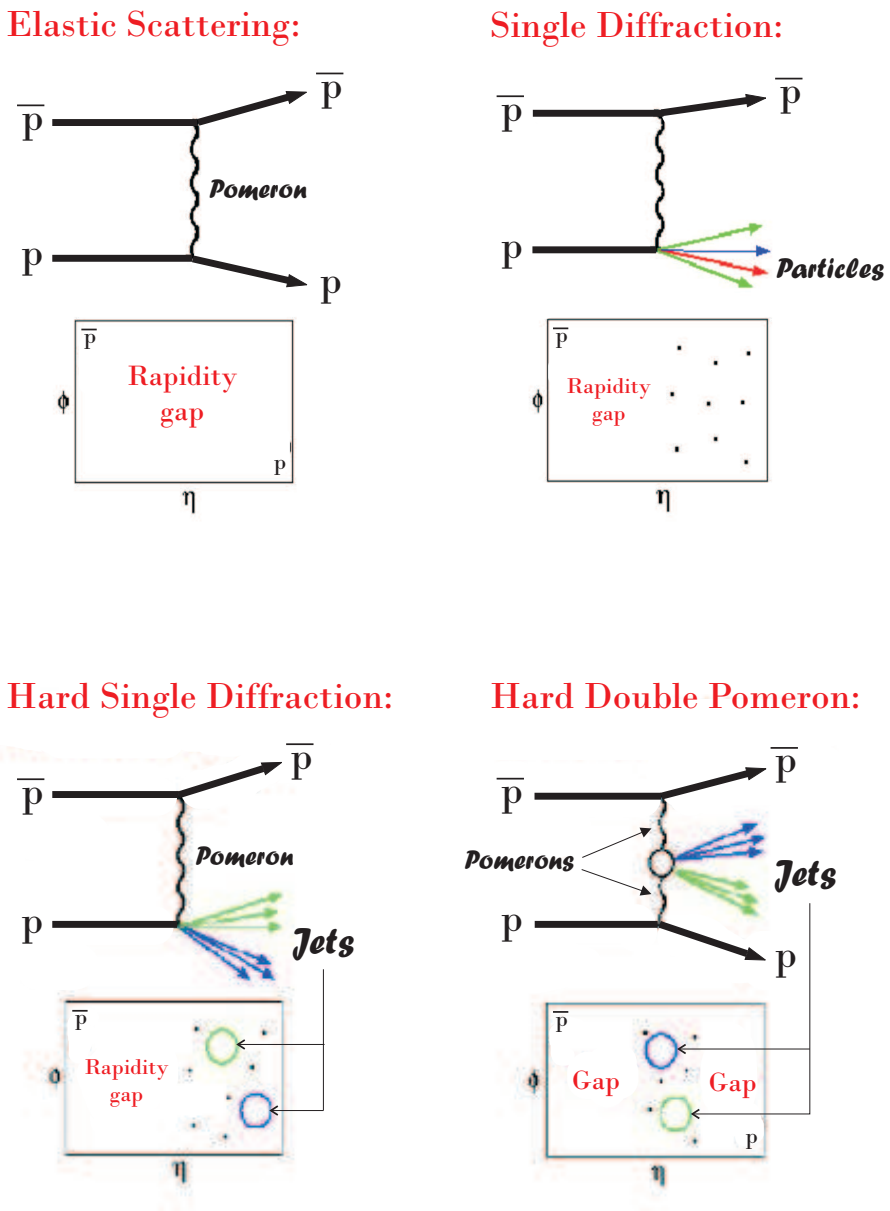

Figure 2.1: Illustration of diffractive processes.

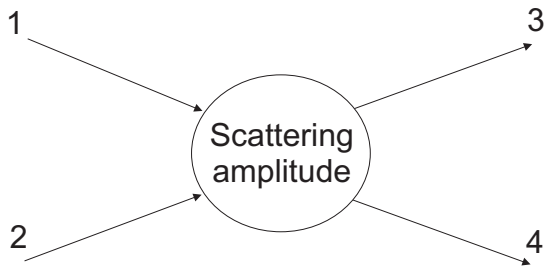

Figure 2.2: Generic 2→2 scattering process.

can be typically measured experimentally as well as predicted theoretically. While the expression for the differential cross-section using a scattering amplitude can be expressed as:

$$\frac{d\sigma}{dt} = \frac{\pi}{s^2}|A(s,t)|^2 \,, \tag{2.2}$$

the total cross-section and scattering amplitude of the process are related through the *optical theorem*:

$$\sigma_{tot} = \frac{4\pi}{s}\Im m\, A(s,0) \,, \tag{2.3}$$

where $\Im m\, A(s,0)$ means forward (momentum transfer $t = 0$) imaginary part of the scattering amplitude.

Because the total cross-section corresponds to probability, there must be a *unitarity condition*, which guarantees that the individual probabilities sum up to unity. The unitarity condition does not allow for the total cross-section to rise freely with increasing s and there is an important upper bound, called *Froissart-Martin bound* [7, 8]

$$\sigma_{tot} < \frac{\pi}{m_\pi^2}(\ln s)^2, \text{ for } s \to \infty \tag{2.4}$$

where m_π is a pion mass.

All processes can be viewed in a different interaction topologies. The *s-channel* and the *t-channel* of an individual process are shown in Fig. 2.3. When we calculate the scattering amplitude, and thus the cross-section, we must consider all possible Feynman diagrams, which contribute to the interaction with the same input and output conditions. The advantage of the different interaction topologies view is that once the amplitude A(s,t) is calculated for the s-channel process, the amplitude corresponding to the t-channel process can be obtained simply by interchanging s and t in the final expression even though the actual processes are quite different. This property is called a *crossing symmetry*.

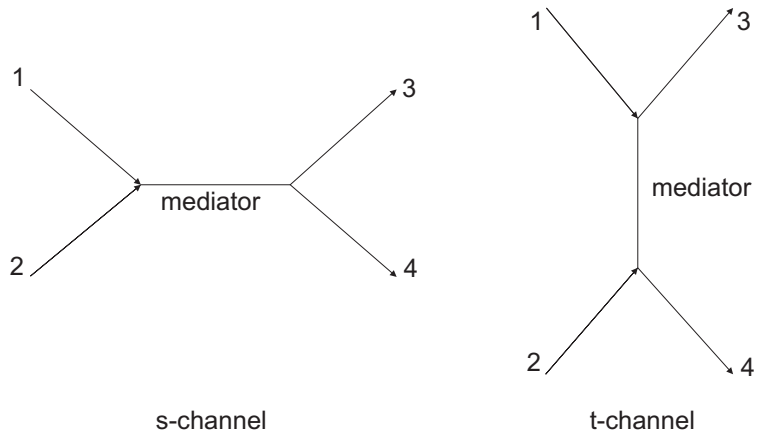

Figure 2.3: An s- and t-channel topologies for a 2→2 process.

2.1.2 Regge Theory

This theory of strong interactions, named after the Italian physicist Tullio Eugeno Regge, was found in the early 1960's and thus predates quark model and QCD by many years. A basic Regge idea was an extension of integer orbital angular momentum into the complex plane [1, 2]. With such angular momentum, the generalized scattering amplitude can have poles, where according to the theory all real particles are seeded. The poles, called *Regge poles* $\alpha_n(t)$, play a crucial role in the Regge theory. A complex function that connects poles corresponding to particles with the same quantum numbers, is then called *a Regge trajectory*. The concept of Regge theory is that strong interactions proceed via the exchange of particles falling along the trajectories $\alpha(t)$. A trajectory of particles with appropriate quantum numbers is applied in a given process. Using these basic assumptions, Regge came to the main result of the theory, which is an expression for the dependence of scattering amplitude at large values of s:

$$A(s,t) \sim s^{\alpha(t)}, \ for\ s \gg t\ . \tag{2.5}$$

Reader should notice that the theory was constructed without any knowledge or assumption about the underlying mechanism of the strong force and thus the results are applicable to *all* processes. It means that it can be applied also for description of diffractive processes.

In early 1960's Geoffrey Chew and his postdoctoral student Steven Frautschi decided to test the Regge theory with scattering data. The Chew-Frautschi plot [5, 6] is shown in Fig. 2.4 The plot shows the total angular momenta J versus the mass squared $t = M^2$ of particular sets of hadrons; in this case the meson resonances

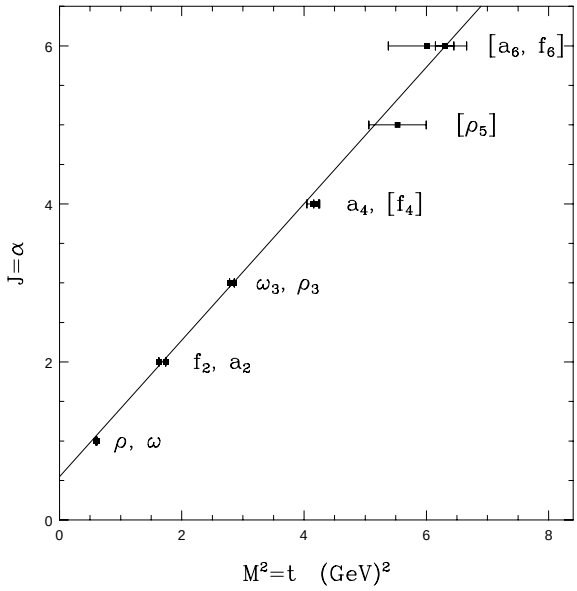

Figure 2.4: The Chew-Frautschi plot.

in $\pi^-\pi^0 \to \bar{p}n$ scattering.

The surprising result was that the regge trajectories appear to have a linear shape $\alpha(t) = \alpha(0) + \alpha' t$, where $\alpha(0)$ is the intercept and α' is a slope of the trajectory. So for hadrons with the *same* quantum numbers, J is proportional to M^2. For example, the pion trajectory in this scheme is $\alpha_\pi(t) \cong 0.9t$ and for generic Reggeon it is $\alpha_R(t) = 0.55 + 0.86t$.

Combining this result with Regge's prediction Eq. 2.5 and an optical theorem Eq. 2.3, we find a very interesting relation between the total cross-section and the center-of-mass energy squared s:

$$\sigma_{tot} \sim s^{\alpha(0)-1}, \tag{2.6}$$

i.e. only the intercept of the trajectory plays an important role for determining the total cross-section of the interaction.

The total cross-sections were measured for many processes with various center-of-mass energies. Fig. 2.5 shows the results from several experiments for pp and $p\bar{p}$ interactions. A fall of the curve for low CMS energies can be well fitted with the *Reggeon* trajectory, with intercept lower than 1, but the rise of the total cross-section with higher CMS energies is more complicated. I. Y. Pomeranchuk proposed already in 1958 [4] that the cross sections of a particle and an antiparticle on a given target are equal to each other at asymptotically high energies. According to today's understanding of nature, every interaction is mediated by an exchange of some ob-

ject. According to the *Pomeranchuk theorem* this object must couple equally to particles and antiparticles at high energies for the total cross section to be the same. Therefore this object (or maybe more objects) must have the quantum numbers of the vacuum. The particle(s) and corresponding Regge trajectory(es) was generally named *pomeron* after Pomeranchuk and according to the Regge theory it must have an intercept greater than unity.

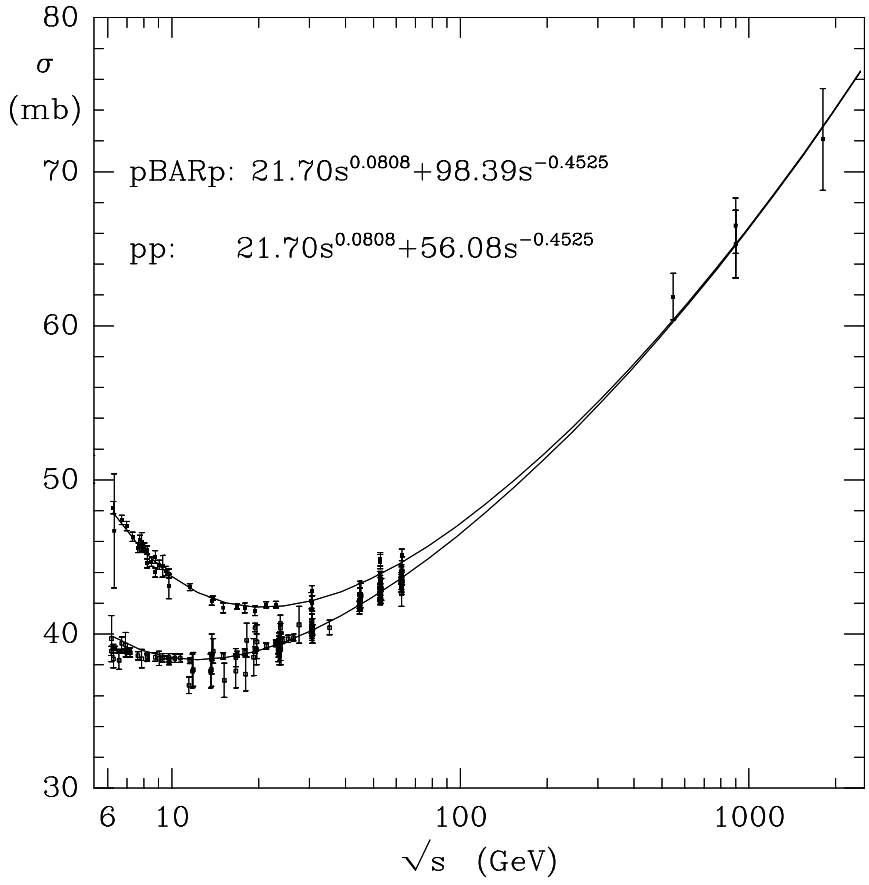

Figure 2.5: The dependence of total cross-section on center-of-mass energy in pp and $p\bar{p}$ collisions.

Donnachie and Landshoff [3] suggested a use of a fit

$$\sigma_{pp(p\bar{p})} = As^{\alpha_P(0)-1} + B_{pp(p\bar{p})}s^{\alpha_R(0)-1}, \tag{2.7}$$

where $\alpha_P(0)$ and $\alpha_R(0)$ are intercepts of pomeron and reggeon respectively. Coefficient A does not depend on the type of interaction because it is the same according to the Pomeranchuk theorem. The fit to the data yields

$$\alpha_P(0) = 1.08 \tag{2.8}$$

The gradient of the trajectory is

$$\alpha'_P = 0.25 GeV^{-2}, \tag{2.9}$$

which was determined from a fit to differential cross sections and the resulting Pomeron trajectory is thus $\alpha_P(t) = 1.08 + 0.25t$.

The rise of the total cross section for high CMS energies could violate unitarity condition. However this could be explained by exchange of more pomerons, because they contribute to the total cross section with alternating signs and increasing magnitude as $s \to \infty$.

The pomeron described above is called *a soft pomeron*. But there appears to be another - *hard* - pomeron. It was found at HERA experiment in 1997 in electron-proton interaction [9, 10] that the pomeron intercept increases with the virtuality of the emitted photon and the energy dependence of the total cross section falls accordingly. According to English physicists Sandy Donnachie and Peter Landshoff [15] such behaviour can be explained by introducing an additional pomeron trajectory with intercept $\alpha_P(0) \sim 1.4$.

Despite the fact that the Regge theory appears to describe well physical results, the real particles that would fall on the soft or hard pomeron trajectories were not found. A promising candidate for the pomeron could be a composite object of two or more gluons - *gluball* [16]. Such object with $J = 2$ and a mass of about 2 GeV was described in [17]. It could be a candidate for the lowest object on the soft pomeron trajectory.

2.2 Rapidity Gaps

2.2.1 Rapidity

The angle description of the final states is not always suitable in hadron collision experiments. Instead, the *rapidity y* is often used to describe the longitudinal properties of final state. The particle longitudinal rapidity is defined as

$$y \equiv \tanh^{-1}\beta_z = \frac{1}{2}\ln\left(\frac{E+p_z}{E-p_z}\right) = \ln\left(\frac{E+p_z}{m_T}\right), \tag{2.10}$$

where $\beta_z (= v_z\ /c = p_z\ /E)$ is the relativistic longitudinal velocity, p_z is the longitudinal momentum, and m_T is the transverse mass ($m_T^2 = m^2 + p_T^2$); p_T denotes the transverse momentum. When the system is boosted along the longitudinal direction

with velocity β'_z, the rapidity is transformed as

$$\begin{aligned} y' &= \ln\left(\frac{E'+p'_z}{m_T}\right) = \ln\left(\frac{\gamma'(E-\beta'_z p_z)+\gamma'(p_z-\beta'_z E)}{m_T}\right) \\ &= y+\ln\left(\gamma'(1-\beta'_z)\right) = y+\frac{1}{2}\ln\left(\frac{1-\beta'_z}{1+\beta'_z}\right) \\ &= y-\tanh^{-1}\beta'_z \end{aligned} \tag{2.11}$$

so it is an additive variable under longitudinal Lorentz transformations. This is the reason why rapidity is used in high energy hadron-hadron experiments, because here the center-of-mass system is generally boosted along the longitudinal direction.

In the low energy (non-relativistic) limit, when $\beta_z \ll 1, p_z \approx mv_z$ and $E \approx m$, the rapidity reduces to the standard longitudinal velocity.

2.2.2 Kinematics of Single Diffractive Scattering

The kinematics of a single diffraction process $p+\bar{p} \to \bar{p}+X$ is described in this section. The variables assigned to the initial and final states are as follows:

$$\begin{aligned} p_p &= (E_p, \vec{p}_p) = (E_{beam}, 0, 0, p_{beam}) \\ p_{\bar{p}} &= (E_{\bar{p}}, \vec{p}_{\bar{p}}) = (E_{beam}, 0, 0, -p_{beam}) \\ p_X &= (E_X, \vec{p}_X) = (E_X, p_X^x, p_X^y, p_X^z) \\ p_{\bar{p}'} &= (E_{\bar{p}'}, \vec{p}_{\bar{p}'}) = (E_{\bar{p}'}, p_{\bar{p}'}^x, p_{\bar{p}'}^y, p_{\bar{p}'}^z) \end{aligned}$$

There are several other kinematical variables used to describe a physical process and which are useful for single diffraction processes as well. Using the four-momenta of the initial beam particles p_p and $p_{\bar{p}}$ and the final systems $p_{\bar{p}'}$ and p_X, we rewrite the Mandelstam variables (Eq. 2.1):

$$\begin{aligned} s &\equiv (p_p+p_{\bar{p}})^2 = (p_{\bar{p}'}+p_X)^2 \\ t &\equiv (p_{\bar{p}'}-p_{\bar{p}})^2 = (p_X-p_p)^2 \\ M_X^2 &\equiv p_X^2 = (p_p+p_{\bar{p}}-p_{\bar{p}'})^2 \end{aligned}$$

Variable s represents a center-of-mass energy squared, t is the negative square of the four-momentum transfer, and M_X is an invariant mass of the final diffractive system X.

Variable s can be modified as

$$\begin{aligned} s &= (p_{\bar{p}'}+p_X)^2 = (2p_X+p_{\bar{p}'}-p_X)(p_{\bar{p}'}+p_X) = \\ &= 2p_X(p_{\bar{p}'}+p_X)+(p_{\bar{p}'}-p_X)(p_{\bar{p}'}+p_X) = \\ &= 2E_X\sqrt{s}+m_p^2-M_X^2 \ , \end{aligned}$$

where m_p is the proton mass, E_X and M_X are energy and mass of the system X respectively. In previous derivation, we use a property $(p_{\bar{p}'} + p_X) = (p_p + p_{\bar{p}}) = (2E_{beam}, 0, 0, 0)$. This leads to the expression of the energy of the system X

$$E_X = \frac{s + M_X^2 - m_p^2}{2\sqrt{s}} \ . \tag{2.12}$$

An absolute value of the 3-momentum of the leading antiproton $p_{\bar{p}'}$ can be expressed using Equation 2.12

$$\begin{aligned} |\vec{p}_{\bar{p}'}|^2 &= |\vec{p}_X|^2 = E_X^2 - M_X^2 = \\ &= \frac{(s + M_X^2 - m_p^2)^2}{4s} - M_X^2 \ . \end{aligned} \tag{2.13}$$

In the high energy limit, where $s, M_X^2 \gg m_p^2$, equation 2.13 implies

$$|\vec{p}_{\bar{p}'}| = |\vec{p}_X| \approx \frac{s - M_X^2}{2\sqrt{s}} \ . \tag{2.14}$$

We now introduce two frequently used variables, the Feynman variable x_F and variable ξ

$$x_F = \frac{p^z_{\bar{p}'}}{p^z_{\bar{p}}} \approx -\frac{p^z_{\bar{p}'}}{E_{beam}}, \quad \xi = 1 - x_F \ . \tag{2.15}$$

x_F means a fractional longitudinal momentum carried out by outgoing antiproton, ξ is an antiproton longitudinal momentum loss, carried out by pomeron. If we assume the transverse momentum of the outgoing antiproton small, and neglect antiproton mass, we can write

$$p^z_{\bar{p}'} \approx |\vec{p}_{\bar{p}'}|, \quad p^z_{\bar{p}} \approx E_{\bar{p}} = \frac{1}{2}\sqrt{s}. \tag{2.16}$$

Using 2.14 - 2.16, we arrive at

$$x_F \approx \frac{|\vec{p}_{\bar{p}'}|}{\sqrt{s}/2} = \frac{2|\vec{p}_{\bar{p}'}|}{\sqrt{s}} \approx 1 - \frac{M_X^2}{s} \tag{2.17}$$

$$\xi \approx \frac{M_X^2}{s} \tag{2.18}$$

The generated particles in general $p\bar{p}$ collisions can be produced only in some interval of rapidity. The maximum and minimum rapidities can be calculated from (m is the particle mass)

$$\begin{aligned} y &= \frac{1}{2}\ln\frac{E + p_z}{E - p_z} = \frac{1}{2}\ln\frac{(E + p_z)^2}{E^2 - p_z^2} = \frac{1}{2}\ln\frac{(E + p_z)^2}{m^2 + p_T^2} \ , \text{ i.e.} \\ y_{max} &\approx \frac{1}{2}\ln\frac{(2E_{beam})^2}{m^2} = \ln\frac{\sqrt{s}}{m} \end{aligned} \tag{2.19}$$

where in the second equation we assumed that $p_z > 0$ and that maximum rapidity is achieved when $p_z \approx E_{beam}, |p_T| \approx 0$. Similarly, we find (with $p_z \approx -E_{beam} < 0$)

$$y_{min} = -\ln \frac{\sqrt{s}}{m} \,. \tag{2.20}$$

The rapidity of the recoil $\bar{p}$ can be calculated in the same way as above by using $E_{\bar{p}'} = (1-\xi)E_{beam}$, $\vec{p}_{\bar{p}'} \approx (1-\xi)\vec{p}_{\bar{p}}$

$$y_{\bar{p}'} = \frac{1}{2}\ln\frac{E_{\bar{p}'} + p^z_{\bar{p}'}}{E_{\bar{p}'} - p^z_{\bar{p}'}} = \frac{1}{2}\ln\frac{E_{\bar{p}'} - |p^z_{\bar{p}'}|}{E_{\bar{p}'} + |p^z_{\bar{p}'}|} \approx \frac{1}{2}\ln\frac{E_{\bar{p}} - |\vec{p}_{\bar{p}}|}{E_{\bar{p}} + |\vec{p}_{\bar{p}}|} \tag{2.21}$$

and thus

$$y_{\bar{p}'} \approx y_{min} = -\ln \frac{\sqrt{s}}{m_p} \,. \tag{2.22}$$

The rapidity of the center of the system X can be obtained similarly, using Equations 2.12 and 2.14, and for p^t_X small

$$\begin{aligned} y_X &= \frac{1}{2}\ln\frac{E_X + p^z_X}{E_X - p^z_X} \approx \frac{1}{2}\ln\frac{E_X + |\vec{p}_X|}{E_X - |\vec{p}_X|} = \\ &= \frac{1}{2}\ln\frac{(E_X + |\vec{p}_X|)^2}{M^2_X} = \frac{1}{2}\ln\left(\frac{1}{M^2_X}\,\frac{4s^2 - 4sm_p^2 + m_p^4}{4s}\right) \approx \\ &\approx \frac{1}{2}\ln\frac{s}{M^2_X} = \frac{1}{2}\ln\frac{1}{\xi} \,. \end{aligned} \tag{2.23}$$

Using Equations 2.18, 2.19 and 2.23, we can calculate width of the system X

$$\begin{aligned} y^{width}_X &= 2(y_{max} - y_X) = 2\left(\ln\frac{\sqrt{s}}{m_p} - \frac{1}{2}\ln\frac{1}{\xi}\right) = \\ &= \ln\left(\frac{s}{m_p^2}\cdot\xi\right) \approx 2\ln\left(\frac{M_X}{m_p}\right) \,. \end{aligned} \tag{2.24}$$

And from the last two equations, the size of the rapidity gap between cluster and the recoil $\bar{p}$ is obtained,

$$\begin{aligned} \Delta y &= y_X - \frac{1}{2}y^{width}_X - y_{\bar{p}'} = \frac{1}{2}\ln\frac{1}{\xi} - \ln\frac{M_X}{m_p} + \ln\frac{\sqrt{s}}{m_p} = \\ &= \ln\left(\frac{1}{\sqrt{\xi}}\cdot\frac{m_p}{M_X}\cdot\frac{\sqrt{s}}{m_p}\right) = \ln\left(\frac{1}{\sqrt{\xi}}\cdot\frac{\sqrt{s}}{\sqrt{\xi s}}\right) = \\ &= -\ln\xi \,. \end{aligned} \tag{2.25}$$

2.3 Jets

Even the most sophisticated detectors are not able to examine directly the primary partons leaving the high-energy interaction. Therefore we use *jets* as a tool for probing the properties of the partons. Jets are described in perturbative QCD and thus we can characterize parton final states back from the jets properties. The concept of QCD description, where there are hadrons coming from the primary parton, can be extended to the particles, detected by the D0 detector. Therefore we can define several levels of the jet propagation. Fig.2.6.

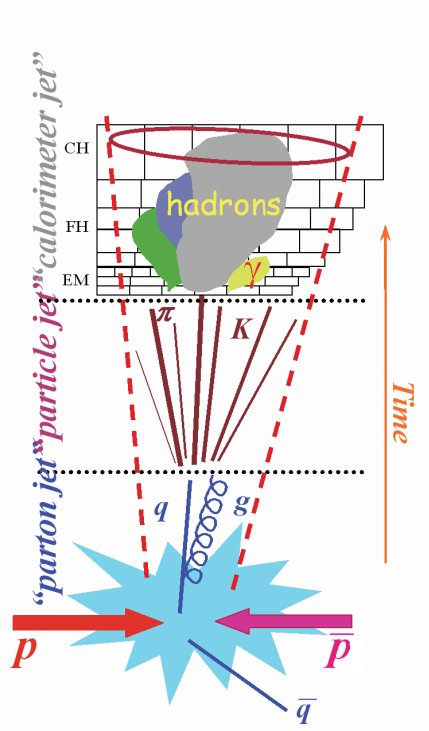

Figure 2.6: Jet propagation through different definition levels.

1. *parton jets* - jets formed from partons after parton showering as described in perturbative QCD

2. *particle jets* - physical jets, which are formed from particles made of basic partons

3. *detector jets* - jets, which are formed from the particles as detected and reconstructed by the detector.

Parton showering can be described with theory and we can thus calculate cross sections to some order of perturbative Quantum Chromodynamics. When we proceed from parton to particle level, we have to use a *hadronization model*. There are many models, which describe hadronization. All of them must satisfy basic feature that they preserve the original properties of the parton level jet (like momentum and energy) and thus of the original partons. This makes the jet concept a useful tool for examining the physical processes. Hadronization models will not be described here, we will concentrate on how jets are defined in practice (on the detector level).

2.3.1 Jet algorithms

Jets are not fundamental objects, so we can use various ways to define them. A prescription, how to make a jet from detected particles, is called *a jet algorithm*. Each jet algorithm should obey some basic rules. Similarly to hadronization models an algorithm should preserve the properties of fundamental partons, it should be independent on the detector and it should be insensitive to soft or collinear emission of partons. There are two considerable types of the jet algorithms; the *cone algorithms* and k_T*-algorithms*.

Cone algorithms are based on geometrical interpretation. We assume the showering particles to propagate within a cone with fixed radius R. The radius of the cone is defined as a radius of the circle in $\phi - \theta$ plane, where ϕ and θ are azimuthal and polar angles respectively. This definition has disadvantage because it is based on polar angle θ, which is not Lorentz invariant. Therefore it is suitable for example for e^+e^- interactions but not for hadron-hadron interactions, where the center of mass system of the incident partons is moving along the beam axis. In this case, the polar angle is replaced with pseudorapidity $\eta = -\ln\ \tan(\theta/2)$. A jet radius R is then defined as

$$\Delta R = \sqrt{(\Delta\phi)^2 + (\Delta\eta)^2}$$

and this definition assures that R is an invariant under Lorentz transformations along the beam. Jets in the D0 experiment use radius R=0.5 or R=0.7, all jets used in this analysis are defined with cone radius 0.7. These values are the most common used in data analyses and are based both on theoretical and observed properties of jets.

Particles detected within this distance from the center of the cone are combined together to calculate properties of the final jet[2]. Particles within a cone are combined

[2]Only a general overview of cone algorithms is given in this section. The detailed description, how the cone centers are found, how particles are combined and how problems with jet definition

according to certain rules, which are called *a recombination scheme*. The most widespread scheme used by experiments is a *Snowmass scheme (E_T-scheme)* ([28]), where

$$E_T^{jet} = \sum_i E_T^i, \quad \eta^{jet} = \frac{\sum_i \eta_i E_T^i}{\sum_i E_T^i}, \quad \phi^{jet} = \frac{\sum_i \phi_i E_T^i}{\sum_i E_T^i} \tag{2.26}$$

By definition, jets in this scheme are massless. This scheme was used for jets during Run I in the D0 experiment. The way of particle combination was changed in Run II to *E-scheme*, where not transverse energies, but the momenta of the 'particles' (calorimeter towers) are directly summed up. The mass of the jet is thus relevant in the E-scheme.

Cone algorithms usually use a concept of *starting seeds*, i.e. the points where the procedure of jet reconstruction starts. They are used to reduce the time spent to find all jets in an event. On the other hand, they bring other problems described in the next paragraph.

The cone algorithms generally suffer from sensitivity to soft radiation, which is introduced in NNLO QCD calculations ([27]). An example of such bad behaviour is shown in Fig. 2.7. Consider two separated partons which propagate on the opposite sides of a single cone. If these two partons form the only starting seeds for algorithm, there will be two reconstructed jets, corresponding correctly to the partons. But at NNLO, there can be a soft gluon radiating between the two separated partons, which can serve as another seed. In this case, there could be only one jet in the end because of merging/splitting procedure, with both partons inside. Thus the outcome of a cone algorithm with seeds is apparently sensitive to infrared parton emission. Similar examples can be used to show the sensitivity to collinear parton emission. The sensitivity to soft radiation was a problem also for Run I cone algorithm and therefore additional starting seeds in the middle of overlapping jets were introduced in a new Run II algorithm. This algorithm is called *Improved Legacy Cone Algorithm (ILCA)* or a *midpoint algorithm*.

A solution, which could solve the problem, is not to use the starting seeds at all. We could do the procedure using all calorimeter towers (not only towers with energy above some threshold), but this is not possible in practice. There are approximately 5 000 towers in D0 detector. Reconstructing jets using all towers would lead to such a computation time per event, which would not be usable in an analysis. The introduction of starting seeds significantly speeds up the algorithm and the concept is essential to be able to reconstruct the jets in the event in an acceptable time. While,

---

are avoided in the D0 Run II cone algorithm, is given in the chapter on data selection

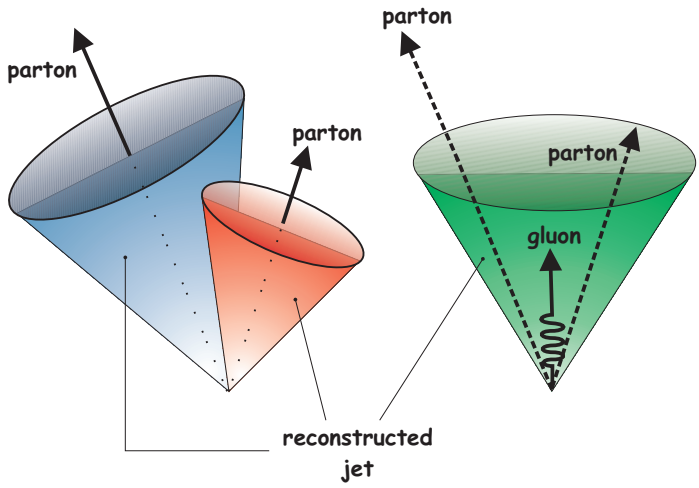

Figure 2.7: The picture illustrates the influence of the soft radiation to the jet reconstruction. The clustering begins in the starting seed partons, shown here as arrows, which lengths are proportional to the partons energy. The presence of the soft gluon causes (in this example) a merging of the jets (on the right), which would not be present in the case without the gluon (on the left).

as pointed out, the algorithm scheme used in Run I brought a soft radiation sensitivity, studies of ILCA showed that the IR sensitivity is considerably reduced. This algorithm produces very similar results as seedless algorithms [27] and simultaneously does not significantly slow down the reconstruction time.

k_T-algorithms are inspired by the perturbative development of parton shower. Partons radiated in the direction far from the original course are usually soft and most of the partons in the shower goes along the original direction. The k_T-algorithm is an iterative procedure, which combines together the two closest particles during each iteration step. The distance between particles is defined so that soft and collinear particles are close to each other. The procedure ends when the closest particles are further than some given distance, which is a parameter of the algorithm. All remaining particles, recombined from the original partons, are called *jets*. Such jets are hard to imagine as they do not have a fixed geometrical shape.

These algorithms are not used in the D0 experiment and in this analysis. Although they have big advantages to cone algorithms because they are, by construction, infrared and collinear safe, they are not wide-spread in hadron-hadron experiments (a good review on cone as well as k_T algorithms can be found in [27]).

Chapter 3

The D0 Experiment at the Tevatron

The Tevatron, about 40 miles west of Chicago, is a synchrotron accelerator that collides protons (p) and antiprotons ($\bar{p}$). At $\sqrt{s} = 1.96$ TeV, it has the highest centre-of-mass energy of any accelerator currently operating in the world, and it generates collisions at an average rate of 1.7 million times per second. The Tevatron accelerator components are housed in a tunnel with a circumference of about 6 km underneath the restored prairie lands at the Fermi National Accelerator Laboratory (Fermilab) in Batavia, Illinois. Two collider experiments, CDF (Collider Detector at Fermilab) and D0 (named after the location along the Tevatron ring) study the products of interactions of the colliding beams. In addition, Fermilab is the home to several accelerator-based neutrino experiments.

3.1 The Tevatron Accelerator

The Tevatron at Fermilab started operations in 1983 with a 512 GeV proton beam. In 1984, it first attained 800 GeV beams. The first $p\bar{p}$ collisions were observed at CDF with a $\sqrt{s} = 1.6$ TeV center-of-energy in 1985. Collisions with $\sqrt{s} = 1.8$ TeV were first attained in 1986. Collider Run I, which included the D0 detector, began in 1992 and in its 4 years of collisions delivered luminosities of approximately 130 pb^{-1} to each collider detector. The accelerator and detectors underwent upgrades after the end of Run I and in March 2001, Collider Run II began with a center-of-mass energy of $\sqrt{s} = 1.96$ TeV

The accelerator complex[1] is a chain of particle accelerators at increasing energies and is shown in Fig. 3.1. It is made up of 8 individual (linear and circular)

[1]The following information are primarily drawn from references [19] [20] [23].

accelerators with a total length in excess of 9000 meters and consuming energy at a rate of 30 MW.

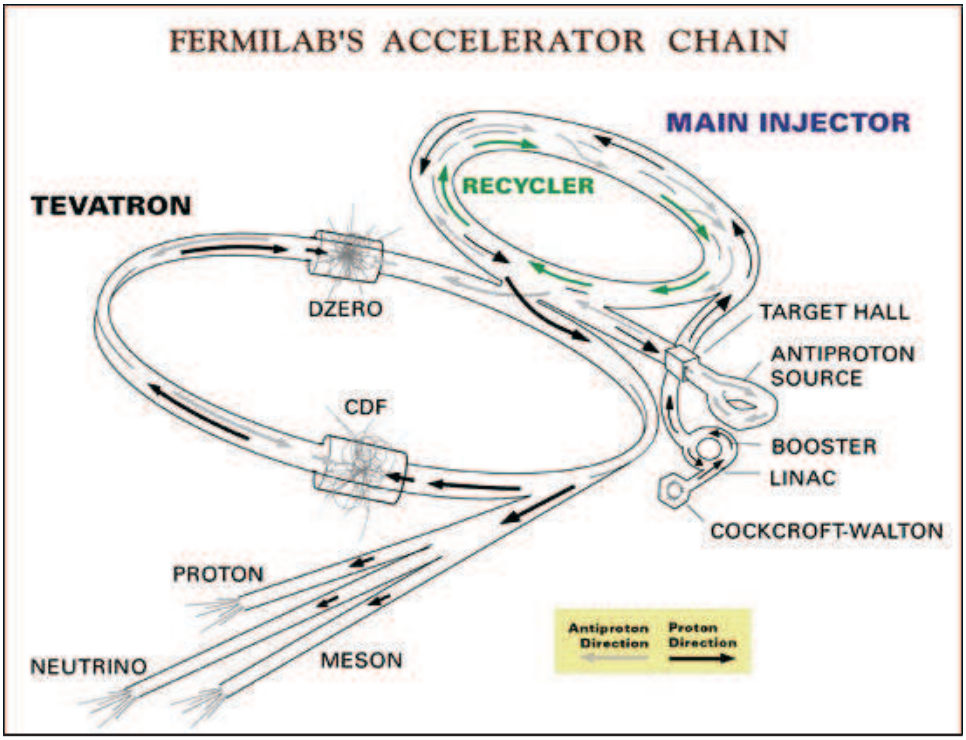

Figure 3.1: Fermilab chain of accelerators

Tevatron chain starts inside a *Cockcroft-Walton pre-accelerator*, where a small amount (several liters) of hydrogen gas is placed. Hydrogen gas is ionized here by adding an extra electron to the hydrogen atom and H^- ions are then accelerated through a series of electrical potential differences to the energy of 750 keV. After this they are sent to Linac, an approximately 130m long line of radio frequency (RF) cavities. Here the ions go through tubes separated by gaps, and are accelerated with an alternating low frequency electric field. The electric field gives a positive gradient in the gaps and forces the accelerated particles to form discrete groups of so called bunches. The bunched ions are accelerated by the Linac to 400 MeV, and at the end they are passed through a carbon foil which strips both electrons from the ions leaving bunches of bare protons. These are then injected into the Booster, which is a small synchrotron accelerator that accelerates the protons to 9 GeV.

The proton bunches then enter the Main Injector, a larger synchrotron, 3 kilometers in circumference, with several modes:

- at first, it accelerates protons to 120 GeV and sends them to the $\bar{p}$ source, and

the fixed target and neutrino experiments

- in the second, protons are accelerated to 150 GeV and injected into the Tevatron ring
- in the third, it receives antiproton bunches from the Accumulator or the Recycler, accelerates them to 150 GeV and prepares for injection into the Tevatron

Antiprotons are created by firing protons onto a Nickel target, using tens of thousands of protons to produce each single antiproton. The antiprotons are accumulated and stored at 9 GeV until they are needed for a period of collisions, known as a store, for which they are sent to the Main Injector for acceleration to 150 GeV and injection into the Tevatron ring. Inside the Tevatron a set of RF cavities accelerates the p and $\bar{p}$ beams to 980 GeV by boosting the particles when they pass; the field frequency is matched to the increasing rotational frequency of the beam. The Tevatron magnets are superconducting. Dipole magnets hold the beam in a circular orbit by exerting a horizontal Lorentz force $F = qv \times B$, where q is the charge and $v \times B$ is the vector cross product between the beam velocity and magnetic field. The magnetic field is increased to match the increasing particle energy. Quadrupole magnets focus the beam by deflecting stray particles back into the correct path in either the vertical or horizontal planes. There are also sextupole magnets for higher order corrections. Each beam has a 36 bunch structure. The bunches are divided into three groups of 12 bunches and each group is referred to as a *superbunch*.

3.1.1 Beam Structure

Tevatron beam is divided into 159 *ticks* (reader should assume ticks more like *time* units than *space* units). Ticks are evenly spaced along the beam and protons and anti-protons are located in these ticks. Tevatron revolution frequency is 47713 Hz, which gives a length of 132 ns for each tick. Within a superbunch there is always a gap of two *empty* ticks between two subsequent bunches, i.e. the space between two bunches within a superbunch [2]is $3 \times 132 = 396$ ns, spacing between two superbunches is about $2.5\mu s$.

The basic beam properties, like number of protons and anti-protons in the bunch, vary between different bunches (different ticks) and depends on time as well. Consequently, the instantaneous luminosity corresponding to the crossing

[2]Because of the increased energy, the time space was decreased since Run I, where it was 3.5μs. This decrease had consequent demands on electronics upgrade, e.g. for calorimeter, as described in next chapters.

of two bunches depends on the tick number. Therefore the luminosity in the D0 experiment is measured on tick-by-tick basis. The typical value for number of protons in a bunch is 2×10^{11} particles while a typical antiproton bunch carries about 2×10^{10} particles. A typical instantaneous luminosity at the beginning of the store during RunIIa was about $1 \times 10^{32} cm^{-2} s^{-1}$.

Proton and anti-proton beams are *held apart* in helical orbits everywhere except the two interaction regions. These are named by their locations on the ring; D0, where there is a detector of the same name, and B0, where there is the CDF detector.

3.2 The D0 Detector

The D0 detector is nearly four storeys high and surrounds a 20 m section of the beam on the east side of the Tevatron ring (3.3). Surrounding the interaction point are several concentric detector layers, including a tracking system (with two detectors) and a solenoidal magnet; luminosity monitors; a calorimeter; and a muon detector system with a toroidal magnet. There is a forward proton detector to detect outgoing intact beam particles located several meters off the main detector along the beam line in either direction. D0 uses a right-handed coordinate system in which the *z*-axis points along the proton beam direction, toward the south end of the detector. North and south are used to denote the outgoing p and $\bar{p}$ directions respectively. The *x*-axis is in the horizontal plane, pointing out of the Tevatron ring (east) and the *y*-axis points upwards. The azimuthal angle ϕ ranges from 0 - 2π radians. The detector coordinate system is centered on (x, y, z) = (0, 0, 0), and the physics coordinate system is centered on the measured interaction vertex. The detector subsystems are described in the following sections. More details on all aspects of the D0 detector can be found in [18].

3.2.1 Tracking System

The tracking system is typically the first system encountered by particles that emerge from the interaction point, measuring the trajectories of charged particles in a magnetic field. There is an inner detector, the silicon microstrip tracker (SMT), an outer detector, the central fiber tracker (CFT) and a superconducting solenoid magnet which encloses them (Fig. 3.3). The SMT is a high resolution detector surrounding the interaction region. It is constructed in two parts: barrels, which are cylinders around the beam pipe, and discs, which are transverse to the beam (Fig. 3.2). The six barrels are arranged longitudinally along the interaction region. Each has four

concentric detector layers, of which some are single-sided and some double-sided. There are 12 small discs with double-sided detector wedges called F-disks in the central region and four large discs with back-to-back single-sided wedges, H-disks, in the forward region. The outer radius of the barrel sections and F-disks is about 10 cm, and for H-disks it is 26 cm. The pseudorapidity coverage is $|\eta| < 2.5$. Each detector layer is a thin wafer of silicon with parallel strips across its surface. Single sided layers have only an n-side, a surface with a positive voltage bias and n-type doping to increase the number of mobile electrons. Double sided layers also have a p-side, which are doped to increase the number of positive electron holes and have a negative voltage applied. When a charged particle passes through the silicon it creates electron-hole pairs: the electrons collect on the n-side and the holes on the p-side. The charge is sampled by SVXIIe chips mounted directly on the central fiber tracker. The SMT is cooled to less than about 5°C to reduce radiation damage.

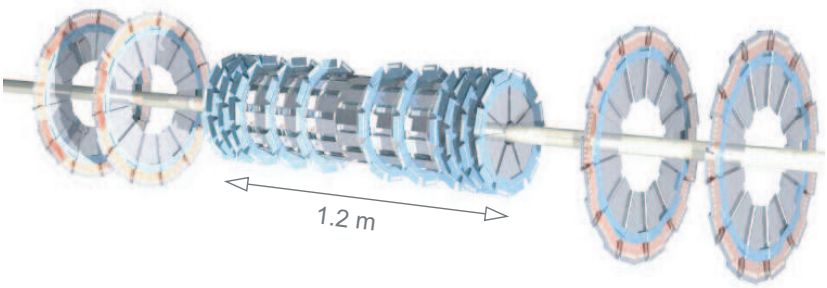

Figure 3.2: D0 tracking system.

The CFT spans the region 20 - 50 cm radially outwards from the beam pipe and $|\eta| < 1.7$. It has scintillating fibers arranged in doublet layers: two layers of fibers, where one is offset from the other so as to leave no gaps. There are eight concentric cylinders in the CFT, each of which has an axial doublet layer and a stereo doublet layer at either $+3^{\circ}$or -3°. The scintillating fibers are made of polystyrene and double clad in acrylic and fluoro-acrylic, with mirrored coating at one end. The cladding materials have lower refractive indices than the polystyrene. Excited atoms in the fibers emit yellow-green light, which is trapped and reflected to the read out ends and taken by clear waveguides to the visible light photon counters (VLPCs). These are avalanche photodiodes that convert the photons into a charge signal, which is read out with SVXIIe chips. The superconducting solenoid is nearly three meters long, with an inner diameter of about a meter. The field is about 2T, axial and uniform over most of the tracking volume. The detector signals (hits)

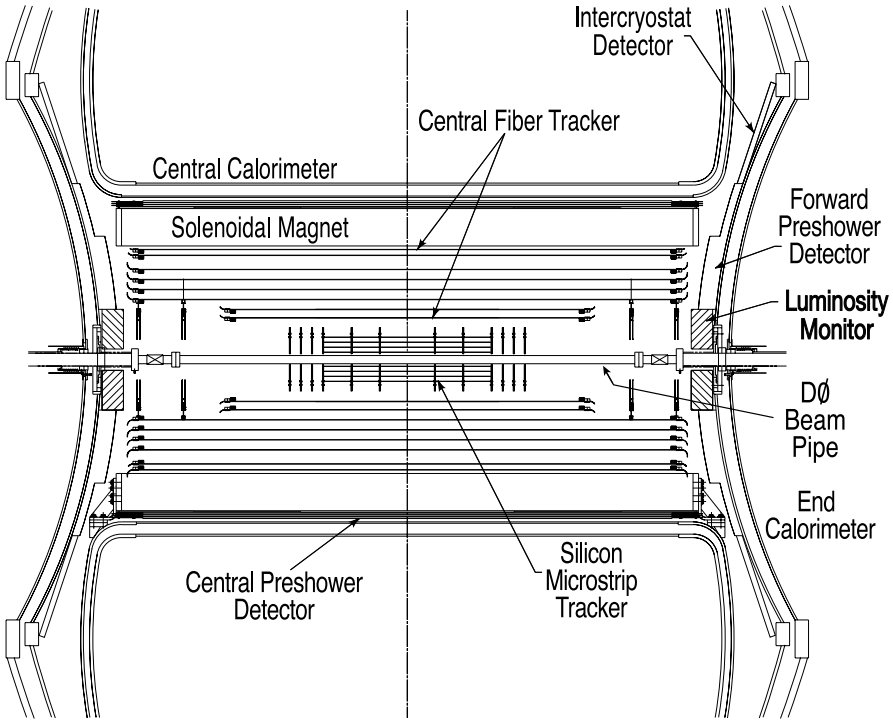

Figure 3.3: Layout of D0 inner systems.

in the tracking system are used to reconstruct the paths of charged particles, for calculation of particle momenta, particle identification and reconstruction of the position of the interaction vertex or vertices. The tracking system can measure the z position of the primary vertex with a resolution of about $35\mu m$. The momentum of a particle with charge e in a magnetic field B can be determined from the radius of curvature of its trajectory R by equating the Lorentz force and the centripetal force mv^2/R. This yields the relationship $p = eBR$.

High momentum charged particles have almost straight tracks, so it is more difficult to determine R and the momentum uncertainty is greater.

3.2.2 Central and Forward Preshowers

The central and forward preshower detectors measure the energy and position of particles before they enter the calorimeter, improving the energy resolution and detecting low p_T electromagnetic showers. The central preshower is mounted on the outside of the solenoid ($|\eta| < 1.3$), and the forward preshower on the calorimeter end caps ($1.5 < |\eta| < 2.5$), as shown in Fig. 3.3. The detectors are made of scintillating strips read out by VLPCs (Visible Light Photon Counters), which provide

higher quantum efficiency and higher rate performance in comparison to standard photomultipliers. The preshower detectors are not used in this analysis and are described elsewhere [25] [26].

3.2.3 Calorimeter

The D0 calorimeter system measures particle energies by inducing showering in its dense material layers. The three main parts are the central calorimeter (CC), which encircles the interaction region up to $|\eta| < 1$, and the two end calorimeters, End Cap North (ECN) and End Cap South (ECS), extending to $|\eta| \approx 5$ at the north and south ends. Each is enclosed in a separate cryostat. There is some detector coverage between the main calorimeters provided by the massless gap detectors and intercryostat detector (ICD). All of the calorimeter detector systems are from Run I except the ICD.

Calorimeter geometry

The fine segmentation of the calorimeter allows shower position and shape measurement. Radially, it is several layers deep: starting from the inside these are the electromagnetic section (EM) which has 4 layers; the *fine hadronic* section (FH) with 2 - 4 layers; and the coarse hadronic section (CH) which has 1 - 3 layers. Each layer is divided into small units called cells. Most cells have an area $\Delta\eta \times \Delta\phi = 0.1 \times 0.1$. This geometry, with towers of cells radiating from the center of the detector, is reffered to as pseudo-projective because the cells lie along lines of pseudorapidity but their boundaries do not (Fig. 3.5). Each cell has unique detector coordinates (layer, ieta, iphi), where ieta and iphi are integers corresponding to location in η and ϕ. In general, each ieta value corresponds to a detector η width of $\Delta\eta = 0.1$. The range is from -37 to 37 (with no null value). Similarly, iphi ranges from 1 - 64 and each integer corresponds to a detector ϕ width $\Delta\phi = 2\pi/64 \approx 0.1$. There are two regions where the cells have different sizes. In the forward region $|\eta| > 3.2$ the cells are larger in $\Delta\eta$ because of the diminishing physical size of pseudorapidity units (Table 3.2.3), and their azimuthal width doubles to $\Delta\phi = 0.2$. In the central region $|\eta| < 2.6$ the third EM layer is divided more finely with $\Delta\phi \times \Delta\eta = 0.05 \times 0.05$. This is to define the EM showers more precisely at the depth of their maximum energy deposition. Figure 3.6 illustrates the calorimeter geometry. Towers are drawn as an ieta-layer projection, demonstrating the correspondence between ieta and detector η and the coverage of the various layers. The CCCH is the central calorimeter coarse hadronic region. The end calorimeter hadronic region has three concentric

$\|ieta\|$	$\|\eta\|$ interval
1	0.0 - 0.1
2	0.1 - 0.2
3	0.2 - 0.3
...	...
32	3.1 - 3.2
33	3.2 - 3.42
34	3.45 - 3.7
35	3.7 - 4.1
36	4.1 - 4.45
37	4.45 - 5.2

Table 3.1: Conversion between calorimeter towers ieta and corresponding pseudo-rapidity interval.

cylinders around the beam pipe: the inner module (End Cap Inner Hadronic Module) at highest pseudorapidity, which has up to four hadronic layers and one coarse hadronic layer, the middle module (End Cap Middle Hadronic Module) which has four fine hadronic layers and one coarse hadronic layer, and the outer module (End Cap Outer Hadronic Module) which has up to three coarse layers. As shown in Figure 3.6, the calorimeter EM layers extend to $|\eta| = 4.1$, the first two FH layers to $|\eta| = 4.45$, and the last two FH layers and one CH layer extend to $|\eta| = 5.2$.

Calorimeter Cells

A typical calorimeter cell is shown in Figure 3.7. The cell is filled with liquid Argon, with an absorber plate connected to ground and a readout plate at +2.0 kV. A charged particle passing through the cell leaves a trail of ionisation in the liquid Argon, and the free electrons then drift to the readout plate. The dense absorber induces showering so all the energy of the incident particle is measured. The absorber in EM cells is uranium, for FH cells it is uranium-niobium alloy, and in the central and end CH cells copper and stainless steel are used. The liquid argon gaps are 2.3 mm wide, with an electron drift time of 450 ns. The absorber plates are 3-6 mm wide in the EM and FH layers and about 47 mm wide in the CH so as to ensure all the energy is sampled within the calorimeter. For the readout, drift electrons induce a charge on copper pads etched onto a G10 fiberglass board with a resistive coat of epoxy.

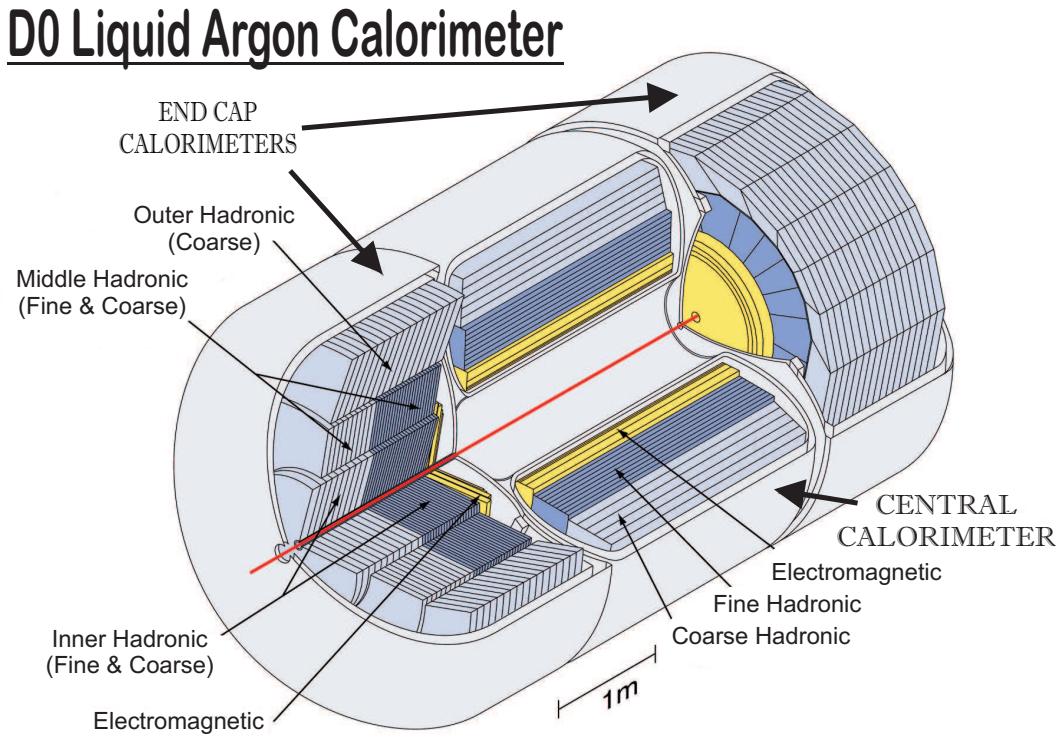

Figure 3.4: D0 calorimeter

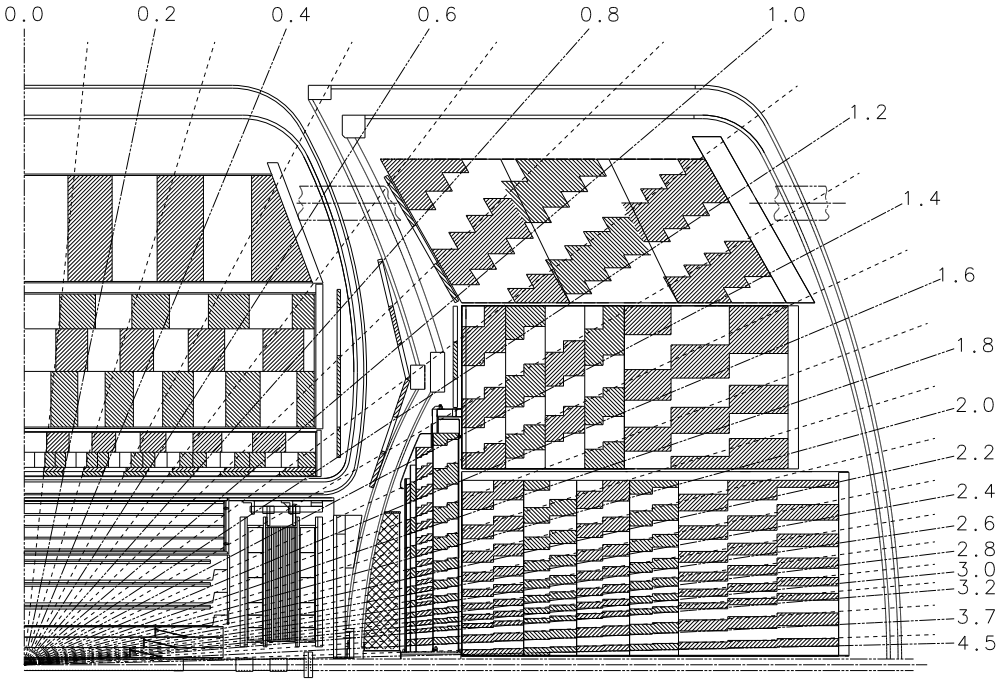

Figure 3.5: Layout of the D0 calorimeter cell division. Cells are arranged according to η and ϕ intervals into *towers*. Picture shows the η towers of the cells.

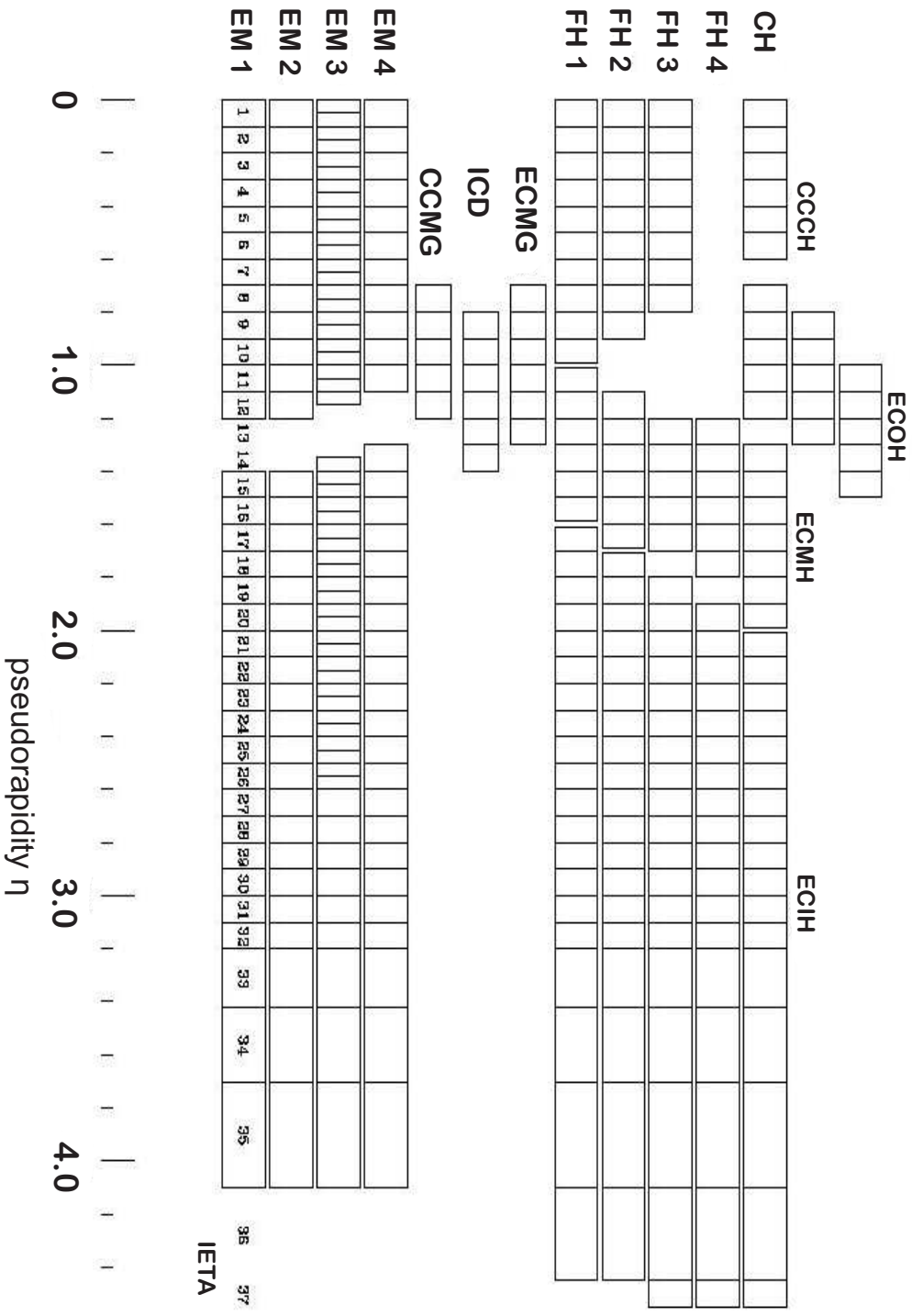

Figure 3.6: Layout of ieta $\times$ layer plane of the calorimeter. Detector η coverage is shown at the bottom and corresponding ieta values in the EM1 section.

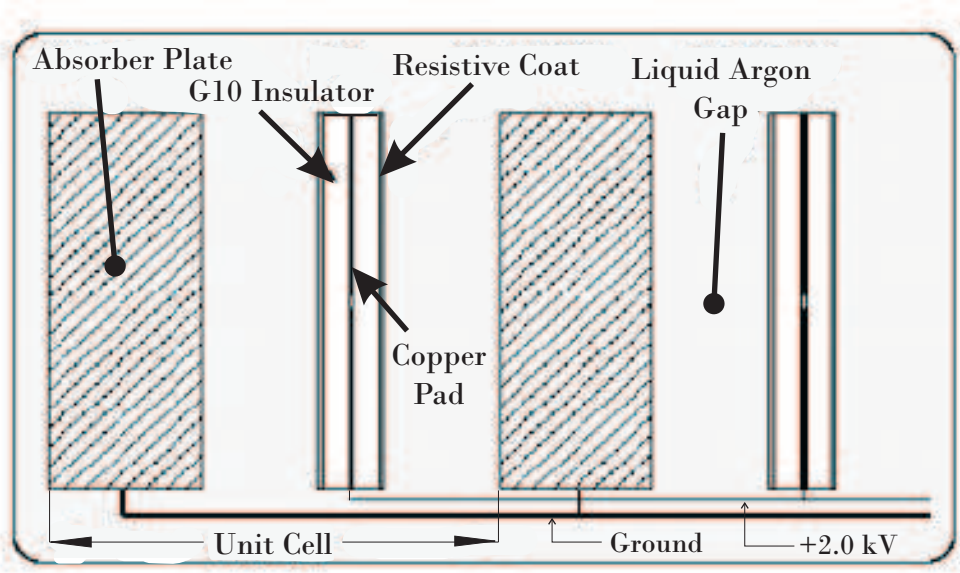

Figure 3.7: The layout of single calorimeter cell.

Electronics

Each calorimeter cell is a capacitor. The charge is sent to a preamplifier which amplifies and shapes the signal so that all channels have a similar shape: the charge rises during the drift time 450 ns and decays over a period of about 15 μs, which is about three quarters of the Tevatron cycle. The drift time is longer than the bunch spacing (396 ns). All of the calorimeter electronics are new for Run II to meet the demands of the increased crossing rate. The preamplifier output is sent to a baseline subtractor (BLS) board, which performs several functions. A shaper circuit takes the first two thirds (260 ns) of the signal and produces a shorter signal that peaks 320 ns after the interaction and decays over three bunch crossing periods. The shaper signal is sampled every tick (132 ns) with every third sample occurring at the peak. The samples are used for baseline subtraction. Baseline subtraction compensates for remaining calorimeter pile-up signals from previous interactions. The baseline is the stored sample from the previous bunch crossing, three ticks before the current signal. The subtraction can result in negative energy signals for the channel. The BLS board sends the signal to be digitized for readout. Cells are subjected to zero suppression to reduce the amount of information recorded for each interaction. Each cell is monitored during beam collision time, and the signal is only stored if it is at least 1.5σ from the mean of the noise. During off-line data processing the T42 algorithm performs a more sophisticated level of suppression [24]. In this

algorithm, most of isolated cells are considered *noisy* and as such discarded. Also all cells with negative energies are discarded. Cells are kept only in two cases:

- the signal is higher than 4σ from the mean
- the signal is between 2 and 4σ from the mean and there is a direct neighbour cell (in 3D space) with signal above 4σ

Mean values and σ's for each calorimeter cell are measured during pedestal runs, taken usually after each store, in the time between two stores when there are no (anti-)protons in the beam-pipe.

3.2.4 Massless Gaps and Intercryostat Detector

The massless gaps are individual calorimeter cells positioned inside the cryostats before the first absorber layers. They cover the region $0.8 \leq |\eta| \leq 1.4$. The intercryostat detector (ICD) is mounted on the calorimeter end caps (see Fig. 3.3) in the region $1.1 < |\eta| < 1.4$. It is made of scintillating tiles, which are read out by wavelength shifting fibers connected to photomultiplier tubes (PMTs). The massless gaps and ICD provide information on shower energy in the regions between the central and end calorimeters.

3.2.5 Luminosity Monitor

The Luminosity Monitor (LM) is used to detect charged particles in the forward region and to determine the luminosity of the experiment. It is made up of two detectors and a logic system. Each of the detectors is an array of 24 plastic scintillator wedges and photomultiplier tubes (Fig. 3.8) situated near the beam pipe at approximately ± 140 cm from the center of D0. One detector is mounted on the south and one on the north calorimeter end caps (Fig. 3.3). Each covers the pseudorapidity region $2.7 < |\eta| < 4.4$.

The LM makes use of the time difference between hits in the north and south disks to distinguish real collisions from the halo interactions. When proton halo interacts with north disk, a muon is produced which passes through the interaction region and hits the south disk about 9 ns later. Similarly for anti-proton halo. The outgoing particles from regular interactions arrive at both disks at roughly the same time. The time difference between the hits is also used to determine the z-coordinate of the interaction vertex.

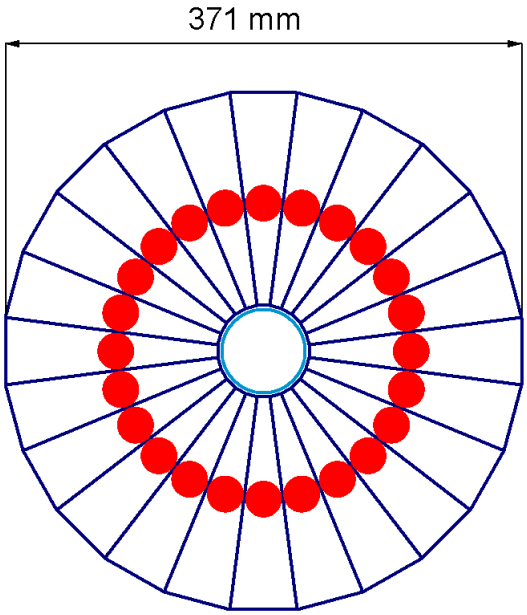

Figure 3.8: Simple layout of one part of the Luminosity Monitor. There are 24 detector wedges, red circles correspond to photomultiplier tubes.

3.2.6 Muon Detector

The muon system was upgraded for Run II and now has full coverage and triggering out to $|\eta| = 2.0$. It is divided into the wide angle muon system (WAMUS) which covers the region $|\eta| < 1.0$ and the forward angle muon system (FAMUS) which covers the region $1.0 < |\eta| < 2.0$. A toroid magnet with a field of 1.9 T bends muons in the r-z plane and either proportional or mini drift tubes are used to identify muon trajectories. In addition, scintillator counters aid in triggering and in reducing backgrounds such as cosmic rays.

The WAMUS system consists of three layers of proportional drift tubes (PDTs), one of which is inside (A-layer) and two of which are outside (B and C layers) the central toroid. The PDT layers are typically 2.79×5.59 m^2 and made of rectangular extrude aluminium tubes. Each drift chamber is subdivided in most cases into 24 cells with each cell $\approx$10.1 cm across with a gold clad, tungsten anode wire down the centre, The gas used (mixture of argon(84%), methan (8%) and CF_4(8%)) provides a velocity of 10 cm/μs and a maximum drift time of 500 ns.

The FAMUS system consists of three layers of mini drift tubes (MDTs) similarly arranged to the PDT layers, with the A-layer inside the toroid (four decks of cells) and the B and C layers outside the toroid (three decks of cells). They are

aligned along the magnetic field lines. Since the maximum drift time is shorter than the bunch crossing time, scintillators are not needed to match drift tube hits to events. However, the scintillators can reduce backgrounds such as cosmic rays and aid in triggering.

3.2.7 Forward Proton Detectors

The Forward Proton Detector (FPD) is used to detect intact protons and antiprotons from elastic and diffractive scattering processes. Schematic layout of FPD is shown in Fig. 3.9.

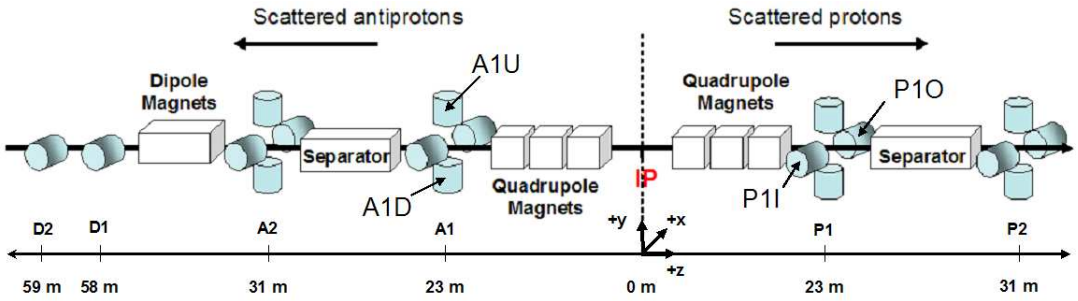

Figure 3.9: The Forward Proton Detector layout.

It is a series of momentum spectrometers that make use of accelerator magnets in conjunction with position detectors along the beam line. In total the FPD has nine spectrometers, each comprising two scintillating fiber tracking detectors, that can be moved to within a few millimeters of the beam. Reconstructed particle hits are used to calculate the fractional momentum loss (ξ) and the four-momentum transfer squared (t) of the scattered protons and antiprotons at the interaction point.

3.3 D0 Trigger System

Triggers serve for quick decision about a type of event. They use hardware and software tools to read basic event attributes. They serve as a tool for reducing the number of interactions written to disks. D0 trigger system consists of three levels, which are successively used to decrease the rate of interactions from $\sim$ 2.5 MHz to $\sim$ 50 Hz.

Level one (L1) is a fast hardware trigger that makes decisions on every possible beam crossing, i.e. with frequency of 7.586 MHz, and is designed to reduce the

event rate up to 10 kHz. There are 256 binary channels in this level, which use basic information from the detector (such as energy from part of the calorimeter, tracking hits, luminosity monitor information, ...) to be set either to zero or one, when given conditions are satisfied or not; therefore the channels are named L1 And/Or terms. Different triggers use different combinations of several And/Or terms in L1. Discrimination based only on physical conditions of the event would still lead to a very high rate of interactions passed to level two. Therefore there is another control of the L1 trigger rate by applying a *prescale*. The prescale drives the L1 to keep every N-th event, where N is a number depending on the physics trigger. The more common interactions the trigger chooses, the higher the prescale is. N ranges from 1 to tens of thousands (hundreds of thousands for zero and minimum bias triggers).

Level two (L2) reduces the L1 rate by factor of 10 (to $\sim$ 850Hz). It is made up of a combination of hardware and firmware tools. Physics objects from the subdetectors are reconstructed here and the information about these objects is collected and passed to the global processor which makes the final decision.

If the event passes L2, the detector signal is digitized and the full detector is read out by Level three (L3). L3 trigger is software trigger that is running on dedicated PC cluster. The output rate of L3 during RunIIa was set at typically 50 Hz. Events selected with L3 are stored on tapes.

Chapter 4

Event Selection

4.1 Data Selection

Data used in this analysis were taken by the D0 detector during the period from August 15, 2002 to August 23, 2004 (run numbers 161973-196584). The definition of physics triggers changed from version GLOBAL_CMT 8.10 to version 13.21. All data were reconstructed using the D0 reconstruction software. This software contains many packages to reconstruct various physical aspects (primary vertices, tracks, jets, missing E_T,..) and is still under development. The version used in the thesis was p14.fixtmb2. This version was very stable and it was used to reconstruct most of the data recorded during RunIIa.

All runs were required to satisfy several conditions on data quality as stored in the D0 Run Database. Each run had to be marked as 'good' in the database for calorimeter, SMT and CFT.

Other quality cuts were applied on each event to remove non-standard operating conditions (e.g. electronics faults, calorimeter hot cells) and background processes (cosmic rays, beam halo interactions, ...). The selection requirements, including triggers used, geometrical and kinematical conditions, are described in detail in next subsections.

4.1.1 Hot Cell Killing

Each calorimeter cell is a complicated electronic system, and as such it can malfunction from time to time. As there are about 50 000 cells and thousands of events per second, the probability that some of them will not work well all the time is very

high. The number of such *bad* cells is measured electronically during the data taking and if this number at the end of the run is too high, the whole run is marked as *bad* and is usually not used for a physical analysis.

In principle, there are two possibilities when a cell is marked as bad - the frequency (multiplicity) and/or energy with which the cell is hit, is either too low or too high. The latter option may be caused when the cell displays a hit each and every event. Such behaviour can be dangerous in data analysis, because those cells can influence reconstruction of tracks and jets - they may serve as starting seeds in jet algorithm, or may change the direction or energy of the jet. These cells are called *hot*.

The uncorrect behaviour is handled by offline software before the data are written to the disks. There are two steps in hot cell killing in the D0 experiment [29]. A pedestal calibration is running usually after each store. Cells satisfying the criteria to be hot (cells with a pedestal value < 400 or > 800) are tagged straight on the calibration taking and are automatically suppressed for use in next store. After the pedestal run ends, the calorimeter is analyzed and cells with pedestals > 1 GeV, sigma > 1 GeV and an occupancy $> 30\%$ for energies greater than 500MeV, are tagged and then suppressed using the *hot cell killer* software.

In case of diffractive analysis using gap approach, we look for regions 'with no energy' and thus any extra energy disrupts our measurements. Therefore for the purpose of this thesis, we reanalyzed the general hot cell killer used in the D0 experiment.

In Figures 4.1 to 4.3, an example of one run measurement of the calorimeter tower multiplicity and of the deposited tower energy is shown. All runs, marked as *bad* for calorimeter problems (e.g. because of high number of hot cells), were removed and all runs are reconstructed with the p14 release software. *Towers* of cells[1] are used separately for electromagnetic (EM) and fine hadronic (FH) parts of calorimeter, instead of using the individual cells or whole calorimeter towers (EM+FH). An analysis of the multiplicity and energy distributions of each cell showed that the occupancy of whole towers is not uniformly spread within the tower, but individual layers of cells have the same properties within EM and FH respectively. This observation rapidly decreases the computer time during the analysis by a factor of ~ 7.

It is clear that some towers are 'out of average', the corresponding bins are

[1] A tower is a group of cells with the same pseudorapidity and azimuthal angle with respect to the center of the calorimeter.

many times higher than their neighbors. These towers should be removed, because they are hot. Zoomed picture on the right side of Fig. 4.1 and 4.2 shows that there are even more bins that seem to be out of average. The procedure of finding all hot towers, used in the analysis is as follows:

1. Overall energy deposited in cells is computed for each run separately.
2. Energy of cells with the same ieta and azimuthal angle within EM (FH) part of calorimeter is summed.
3. For each ieta (which corresponds to some pseudorapidity region - see Table 3.2.3), the mean value and the dispersion is computed over the azimuthal angle.
4. Towers which are more than 3σ from mean value for corresponding ieta are marked as *hot*. These towers (cells) are removed from our analysis.

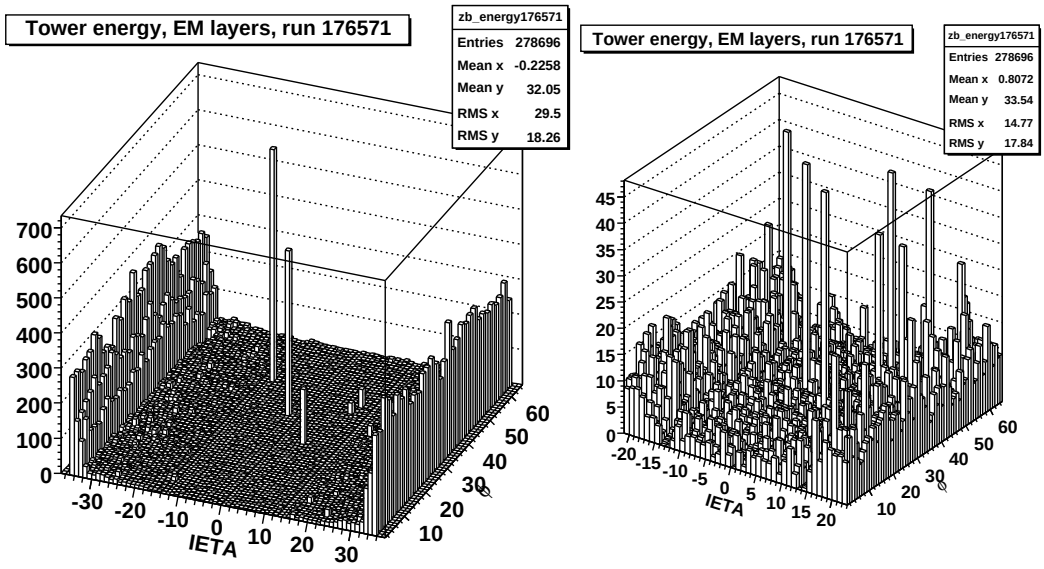

Figure 4.1: Sum of the energy for fine hadronic calorimeter towers during run 176571. A zoomed cut of the central part is shown on the right side.

4.2 D0 Run II Cone Algorithm

During Run I, the D0 collaboration used a recombination scheme which was called $E_T - scheme$. The important property of this scheme is that jets were assumed massless. For Run II, the jet physics group and the Jet Definition Group Les Houches

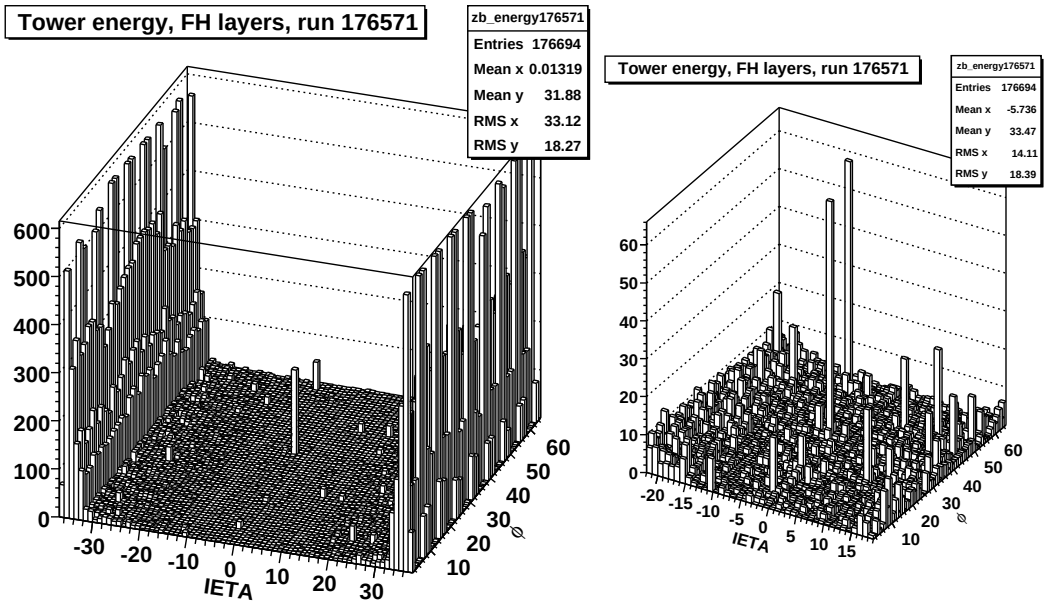

Figure 4.2: Sum of the energy for electromagnetic calorimeter towers during run 176571. A zoomed cut of the central part is shown on the right side.

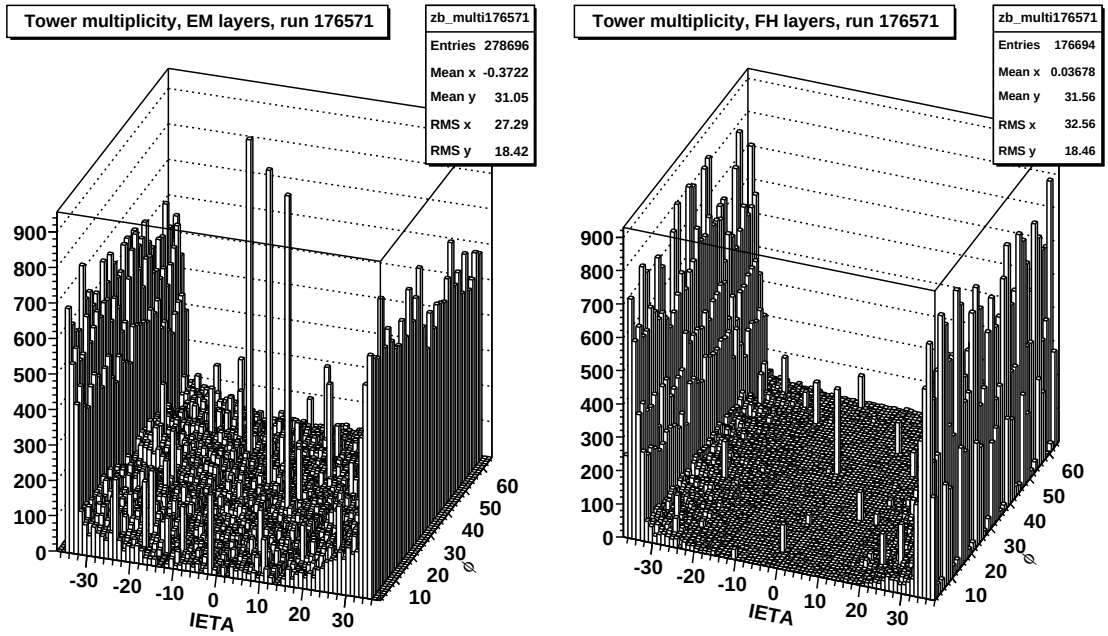

Figure 4.3: Multiplicity of electromagnetic and fine hadronic calorimeter towers during run 176571.

recommended to change the jet definition. Changes are small in definition but important in resulting properties of the jet. Comparing to the old scheme, there are additional starting seeds where jets are looked for, and the jets are no longer massless. The detailed description of the D0 Run II algorithm is given further in this chapter.

Jets are generated from calorimeter towers only and there is no track information used anymore. Each calorimeter tower is assigned a momentum and energy as a 4-momentum sum of momentum and energy of cells contained in the tower. Cell 4-momentum is defined as

$$\mathbf{P}_{cell} = E_{cell}(1, \vec{n}_{cell}), \qquad |\vec{n}_{cell}| = 1. \tag{4.1}$$

where E_{cell} is energy measured by the cell, and $\vec{n}_{cell}$ is a unit directional 3-vector pointing from the primary vertex of the interaction to the cell position. The energy of tower is thus defined as

$$\mathbf{P}_{tower} = (E_{tower}, \vec{p}_{tower}) = \sum_{cells} \mathbf{P}_{cell} \tag{4.2}$$

and energy (momentum) of the jet is

$$\mathbf{P}_{jet} = (E_{jet}, \vec{p}_{jet}) = \sum_{towers} \mathbf{P}_{tower} \tag{4.3}$$

Whereas $\|\mathbf{P}_{cell}\| = 0$, for tower 4-momentum it is no longer valid $\|\mathbf{P}_{tower}\| \neq 0$ and mainly for jet 4-momentum generally holds $\left\|\mathbf{P}_{jet}\right\| \equiv M^2_{jet} \neq 0$. This forms the basic difference between D0 Run I and D0 Run II cone algorithms, jets in Run II E-scheme are in general massive. The main reason for the algorithm change was the simplicity of the definition. We directly sum up 4-momenta of detected 'particles' within a cone and thus obtain energy and momentum of the jet. On the other hand, E_T-scheme used during Run I defined jets as massless and jet properties were computed as a sum of cell E_T and a weighted sum of ϕ and η, as described earlier in the text (Eq. 2.26).

The new recombination scheme introduces massive jets, and so rapidity y and pseudorapidity η are no longer equal[2]

$$y = \frac{1}{2}\ln\frac{E + p_z}{E - p_z}, \qquad \eta = -\ln\tan\frac{\theta}{2}$$

where θ is a polar angle. The jet angle characteristics in the D0 experiment are completed with detector pseudorapidity η_{det}, which is computed as a pseudorapidity

[2]For massless jets (particles), it holds $E = |\vec{p}|$ and thus $\frac{p_z}{E} = \frac{p_z}{|\vec{p}|} = \cos\theta$, which means that $y = \eta$.

using the angle of a calorimeter cell with respect to the geometrical center of the detector.

The D0 Run II jet algorithm iterates in the following steps:

1. As a starting seed, calorimeter towers with the transverse energy higher than $E_T^{seed} = 0.5GeV$ are used.

2. A cone of radius R=0.3 is used to define a seed protojet. Seed protojets are formed from calorimeter towers within a radius R in $\phi \times y$ plane as described by Eq. 4.3.

3. A 4-momentum for the protojet is obtained and a cone is formed around this direction together with the sum of the towers included within this cone. Again, a new direction is obtained, a new cone is formed and the sum of the tower energies is calculated. This is repeated until the direction is stable.

4. There can be more protojets that result in the same direction. These protojets are treated as one.

5. The resulting directions of protojets with this small radius are used as starting points for searching for the jets with the given radius R (usually 0.5 or 0.7). Steps 3 and 4 are repeated to get the new (proto)jets.

6. Resulting protojets can overlap and so we introduce additional starting seeds in the middle of two (three or more) protojets. Only combinations of jets which are within a separation 2R are used. The direction of midpoint is defined as
$$P_{midpoint} = \sum_{i=1}^{N_{protojets}} P_i$$

7. Stable positions for midpoint seeds are found in the same way as in steps 2 (with new R), 3 and 4.

8. All found protojets are ordered according to transverse momentum. If two neighbouring protojets share more than 50% of transverse momentum of the softer one, they are merged. Otherwise they are split and considered as two distinct objects. Calorimeter towers from both protojets are assigned to the new merged protojet and so it does not keep a cone shape anymore. When protojets are split, towers contained in intersection are joined to the closer (in $\eta \times \phi$ space) protojet. 4-momenta of new protojets in both cases are recomputed according to Eq. 4.3 and reordered. This step is repeated until there are no overlapping jets remaining.

9. Protojets with transverse momentum smaller than 8 GeV are removed from the list of protojets.

10. The protojets in the final list are then called jets.

4.2.1 Jet Energy Scale

Although jet algorithms preserve the properties of the primary parton as good as possible, the resulting jet energy must be corrected to the particle level. The corrections come from the detector influence of the measurement and from the topology of the algorithm itself. The procedure is called *a jet energy scale* (JES). Its determination is a complicated process, but each jet analysis must use the JES corrections and also in this thesis they are used with every jet.

The jet energy E_{det}, as reconstructed by the cone algorithm, is corrected to the particle level E_{ptcl} according to the formula

$$E_{ptcl}(E_{det},\eta,R,L) = \frac{E_{det} - \Omega(R,\eta,L)}{R_{jet}(E_{det},\eta,R)S(R,\eta,E_{det})} \tag{4.4}$$

where η, R, and L are the jet pseudorapidity, the cone radius, and the instantaneous luminosity respectively. The correction is managed by 3 parameters (Ω, R_{jet} and S) that are discussed bellow.

Offset $\Omega(R,\eta,L)$ changes the jet energy by energy, which was deposited in the cone and was not directly associated with the $p\bar{p}$ interaction itself (uranium noise, pile-up from the previous beam crossings or additional minimum bias interaction in the current beam crossing). In general, it depends on the place where the jet hits the calorimeter (η), the cone size R, and the instantaneous luminosity L. It is determined from the measured average transverse energy density deposited in the calorimeter during a special minimum bias run. This correction is important mainly for low-p_T jets while it is small for jets above 100 GeV.

Response $R_{jet}(E_{det},\eta,R)$ R_{jet} corrects the jet energy for the response of the calorimeter to particles that constitute the jet. Although the D0 calorimeter is nearly compensated, the response to jets is smaller than one, due to non-linear calorimeter response to particles with low energy and dead material in front of the calorimeter.

The correction is determined from the transverse energy imbalance in photon+jet events using the so called missing E_T projection fraction method. It requires the calorimeter to be calibrated for electromagnetic objects. This EM scale

is obtained independently of the jet energy scale. D0 collaboration uses the known masses of resonances like Z, J/Ψ, or π_0 for this purpose.

Showering $S(R,\eta,E_{det})$ corrects the energy that dissipates from the cone during the shower development in the detector. The correction is determined from the jet profiles in the photon+jet sample. It is larger for smaller cones. It also increases with jet pseudorapidity because the forward cones have smaller absolute sizes (expressed in units of length - meters). The correction is small for the case of central jets (used in this analysis).

4.3 Triggers

A trigger system at D0, as described in general in chapter 3.1, contains a lot of individual triggers, each of which is suitable in different physical analysis. Those used in this thesis are described in following sections.

4.3.1 Zero Bias Trigger

A basic trigger that ensures data to be taken only when there are proton and antiproton bunches crossed within the D0 detector. There is no requirement on beam collision, so this trigger is especially suitable for detector noise studies. In addition to the basic zero bias trigger there is another one, which has an additional condition on the type of calorimeter read-out and which is used in this analysis.

zero_bias trigger at Level 1 requires a Live Beam Crossing. There are no restrictions at Level 2 and 3.

zero_bias_NCU trigger at Level 1 requires a Live Beam Crossing and not unsuppressed calorimeter read out. No conditions at Level 2 and 3.

The prescale for zero bias trigger is $\sim$ 3 400 000.

4.3.2 Inclusive Jet Triggers

There are several main triggers usually used in jet analyses. Their names as used in the D0 experiment are JT_15TT, JT_25TT_NG, JT_45TT, JT_65TT, JT_95TT and

JT_125TT. Their basic purpose is to trigger out events, which contain at least one jet with a given p_T (15, 25, ...).

Level 1 of jet triggers use directly an analog signal from BLS calorimeter boards. This differentiate L1 calorimeter readout from the regular one. The coverage of this trigger is $|\eta| < 3.2$. In L1 stage, the 2×2 towers are grouped together, and thus the size of L1 calorimeter tower is $\eta \times \phi = 0.2 \times 0.2$. On the first level, jet triggers vary in requirements on several towers with some threshold on E_T.

When L1 trigger is set on, the event is passed to Level 2. The information about the towers which made the L1 trigger to fire is also propagated and very simple jets are constructed around these seeds. These 'jets' are formed of 3×3 or 5×5 towers(according to time, when data were taken), the E_T's of which are summed up. For most common jet triggers, there is no Level 2 requirement, for JT_65TT and JT_95TT at least one of these simple jets must pass some transverse energy threshold.

At Level 3, the calorimeter is already precisely read out and a fast simple cone algorithm is processed. It follows the cone procedure with a radius R=0.7. There are starting seeds identified by L1, but there is no splitting or merging in this simple algorithm.

An example of conditions for all trigger levels for most common jet triggers are shown in Tab. 4.3.2. The definitions changed through the time period of data taking. Starting with trigger list global_CMT version 11 all level one conditions are accompanied with a requirement of not calorimeter unsuppressed readout. Also the number of level one towers and the thresholds were changed several times. Before global_CMT version 10, there were no level 2 conditions. Since version 10, the level 2 requirements were applied for triggers JT_65TT and JT_95TT, since version 13 for trigger JT_125TT as well.

4.3.3 Diffractive Jet Triggers

In addition to inclusive jet triggers, there are several other jet triggers, which are suitable for diffractive analysis. They differ from the inclusive ones in level 1 conditions and in prescale values.

The diffractive trigger names are JT_15TT_GapS, JT_15TT_GapN, JT_15TT_GapSN, JT_25TT_GAPS, JT_25TT_GAPN, JT_25TT_GAPSN, JT_45TT_GAPS, JT_45TT_GAPN and JT_45TT_GAPSN. Triggers JT_25TT_GAPS/N were used in older trigger list versions, later they were replaced with JT_15TT_GapS/N and JT_45TT_GAPS/N.

Trigger name	**Level 1**	**Level 2**	**Level 3**	**Prescale**
JT_15TT	2 towers with $E_T > 3$ GeV	none	1 jet with $E_T > 15$ GeV	1.6k-240k
JT_25TT_NG	2 towers with $E_T > 5$ GeV	none	1 jet with $E_T > 25$ GeV	200-22k
JT_45TT	2 towers with $E_T > 5$ GeV	none	1 jet with $E_T >$45 GeV	14-3 000
JT_65TT	3 towers with $E_T > 5$ GeV	1 jet candidate with $E_T >$20 GeV	1 jet with $E_T >$65 GeV	2-400
JT_95TT	3 towers with $E_T > 5$ GeV	1 jet candidate with $E_T >$50 GeV	1 jet with $E_T >$95 GeV	1-20
JT_125TT	3 towers with $E_T > 5$ GeV	1 jet candidate with $E_T >$70 GeV	1 jet with $E_T >$125 GeV	1

Table 4.1: Jet triggers used in inclusive jets analyses. Trigger definitions on Level 1 and Level 2 were modified a little bit during the time and prescales are shown only approximately, because they change strongly with luminosity changes. Jet candidate in L2 is computed as a sum of 3×3 or 5×5 towers (the size was changed during the time period when the data sample was taken). L3 jets are defined using simple cone algorithm, where no splitting/merging is used.

As mentioned, the conditions on these triggers are the same as for the corresponding inclusive triggers except the condition on level 1. Diffractive level 1 trigger is extended by the requirement on the luminosity counter on the corresponding side of the detector (on both sides for GapSN triggers), which must be switched off.

The prescales for all diffractive triggers are usually 1, for higher luminosity they can rise up to few tens. The prescales for south diffractive triggers are higher than for north diffractive triggers.

4.3.4 Trigger Turn-On Points

Triggers are not 100% efficient directly above the threshold given in their definition. The inefficiency comes from level one or two, where 'good' jets can be rejected even when they could be reconstructed on level 3 with p_T above the given threshold. The p_T values, above which we consider the trigger sufficiently efficient, are called *trigger turn-on points*. Only jets which pass the trigger with p_T above its turn-on point, are used in this analyses.

The idea of finding the turn-on point for a given trigger is to compare the p_T spectrum of jets, which passed the trigger, with p_T spectrum of jets, which passed the lower p_T trigger. The higher is the jet p_T, the higher is the probability that the jet turns on one of the triggers. In principle, all events that pass a given trigger, should also pass a trigger with lower p_T cut (if there was no prescale).

The p_T spectrum of the leading jet for various jet triggers is shown in Fig. 4.4. The jets after JES corrections are used. Each spectrum is scaled by the luminosity for a given trigger, which takes into account the trigger's prescale; the luminosities are shown in Table 4.2. It is clear that from some point the p_T spectra of all triggers are the same. The p_T point where the trigger starts to behave similarly to other triggers is the searched turn-on point.

Trigger	Luminosity
JT_15TT	118.2 nb^{-1}
JT_25TT_NG	2 077 nb^{-1}
JT_45TT	33 868 nb^{-1}
JT_65TT	171 884 nb^{-1}
JT_95TT	387 402 nb^{-1}
JT_125TT	398 087 nb^{-1}

Table 4.2: Measured luminosity for jet triggers.

The ratio of two subsequent triggers is shown in Fig. 4.5. A fit was made using the error function:

$$\begin{aligned} f(p_T) &= \frac{1}{2}\left[1+erf(a_0 p_T + a_1)\right] \\ erf(x) &= \frac{2}{\sqrt{\pi}}\int_0^x d\xi e^{-\xi^2} \end{aligned} \tag{4.5}$$

The turn-on points are defined so that the triggers were sufficiently efficient. But the number of events in the diffractive sample is low, so it is necessary that the p_T cut keeps as many of them as possible. This was taken into account in the diffractive turn-on point definition. The diffractive p_T spectra are shown in Fig. 4.6. The luminosity for diffractive triggers was not measured during the data taking for the period used in this analysis. Therefore the luminosity can not be used to scale the spectra as in the case of inclusive jets and it must be scaled artificially. As in the inclusive case, it is assumed that in p_T area much higher than the p_T threshold, the trigger is fully efficient. The parameter x, used in the plot, is set so that the consequent trigger spectra correspond to one another above a p_T value much

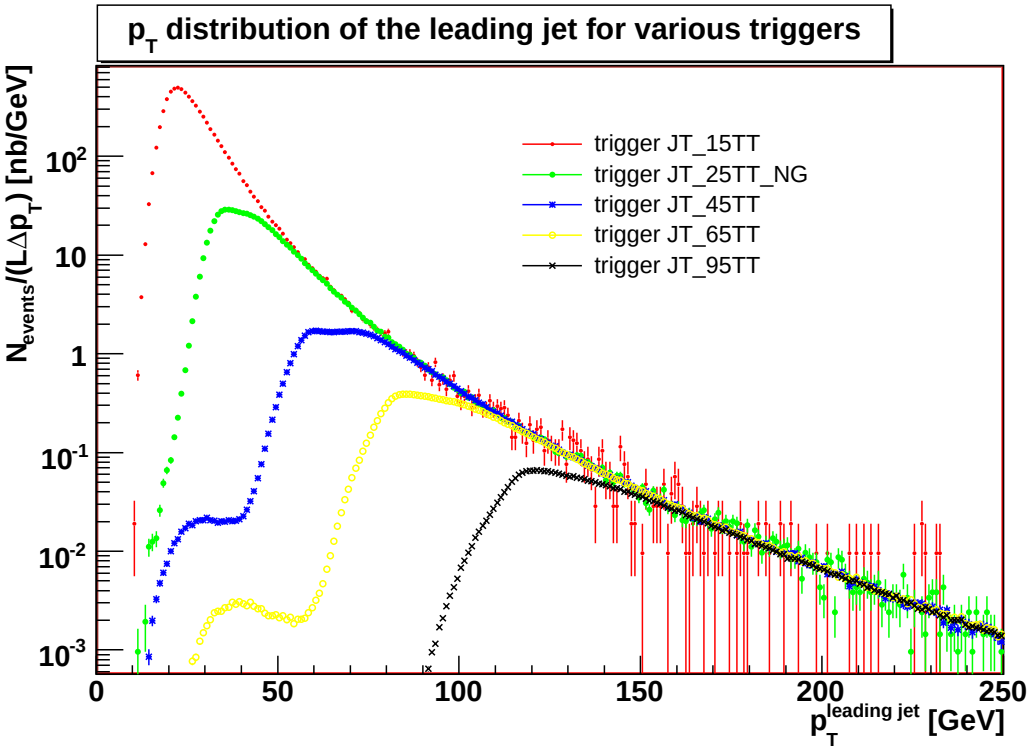

Figure 4.4: The inclusive leading jet p_T spectra for various jet triggers.

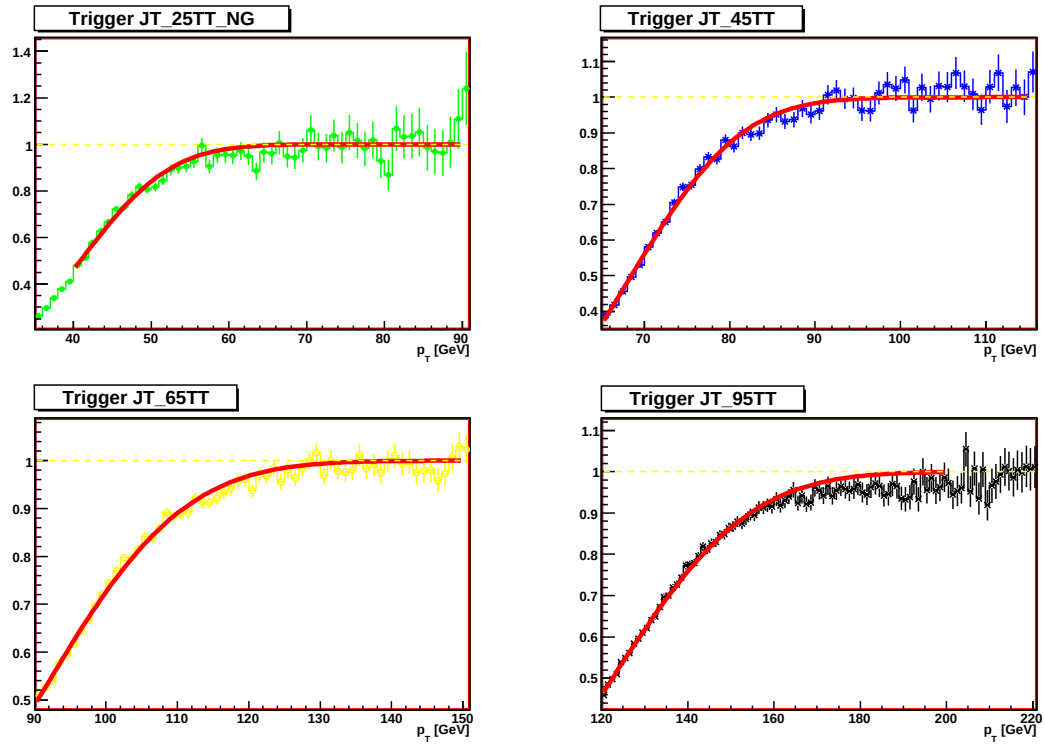

Figure 4.5: The ratio of p_T spectra for two subsequent triggers.

higher than the threshold of the higher one. The ratio of two subsequent triggers for diffractive events is shown in Fig. 4.7.

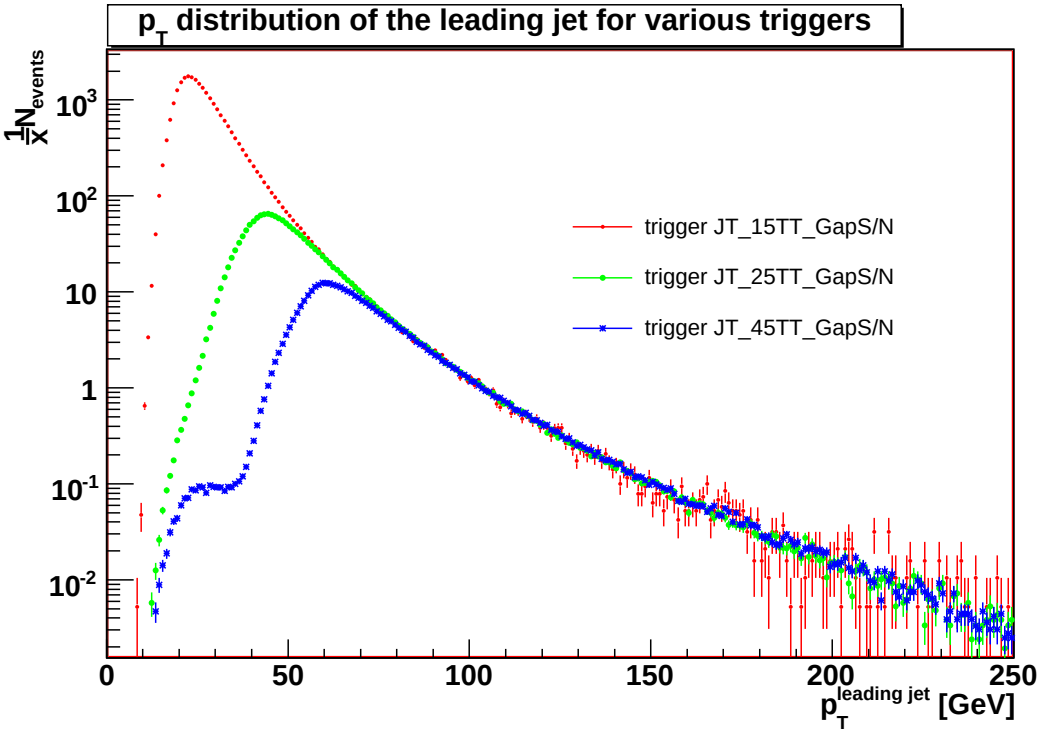

Figure 4.6: The diffractive leading jet p_T spectra for various jet triggers. x is a normalization constant to fit the spectra for different triggers.

To compare the physical results for inclusive and diffractive samples, the same leading jet p_T cuts should be used.

1. The turn-on point for trigger JT_25TT (diffractive or inclusive) is set to 61 GeV, which corresponds to 99% efficiency.

2. Analyzing the plots for trigger JT_45TT, we find a reasonable turn-on point at $\sim$ 85 GeV. However, this p_T cut rejects most of the diffractive events that pass the trigger. Therefore a lower turn-on point of 75 GeV was used. The Fig. 4.8 shows the $\Delta\phi$ distributions for events above a threshold of 75 GeV and 85 GeV. The difference is negligible and the change in the cut increases the number of diffractive events which pass the trigger, more than twice.

3. Trigger JT_15TT (diffractive as well as inclusive) brings the biggest complications. For the inclusive sample, there is a trigger JT_8TT, which could be used as a comparative trigger, but the efficiency of it is very poor. The

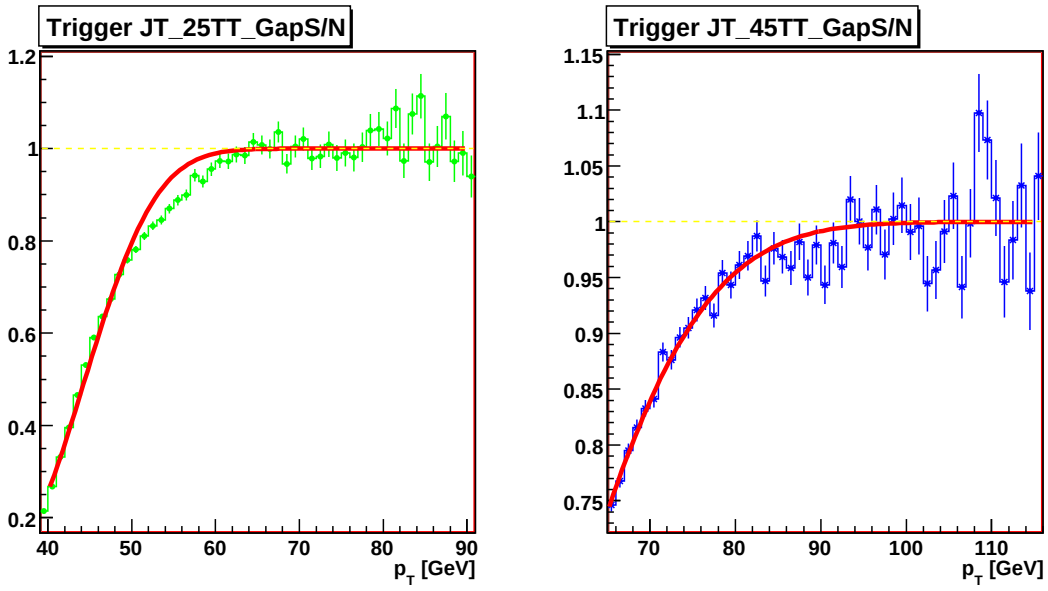

Figure 4.7: The ratio of two subsequent diffractive triggers spectra.

problem is that the threshold of this trigger is the same as the cut on the jet acceptance in the D0 jet reconstruction software. Therefore it is usually not used in QCD analyses in the D0 experiment. For diffractive triggers there is no JT_8TT trigger at all. Therefore the turn-on point for trigger JT_15TT is artificially set to 25 GeV in relation to trigger JT_45TT (where the cut is set to 75 GeV).

All inclusive and diffractive triggers turn-on points used in this analysis are shown in Table 4.3.

Trigger	Turn-on point
JT_15TT(_GapS/N)	25 GeV
JT_25TT(_NG, _GapS/N)	61 GeV
JT_45TT(_GapS/N)	75 GeV

Table 4.3: Trigger turn-on points for triggers used in the thesis.

4.4 Event Selection Criteria

Every event must pass the basic selection criteria. It had to be recorded during the good runs (according to D0 Run Database) and must be included in the Luminosity

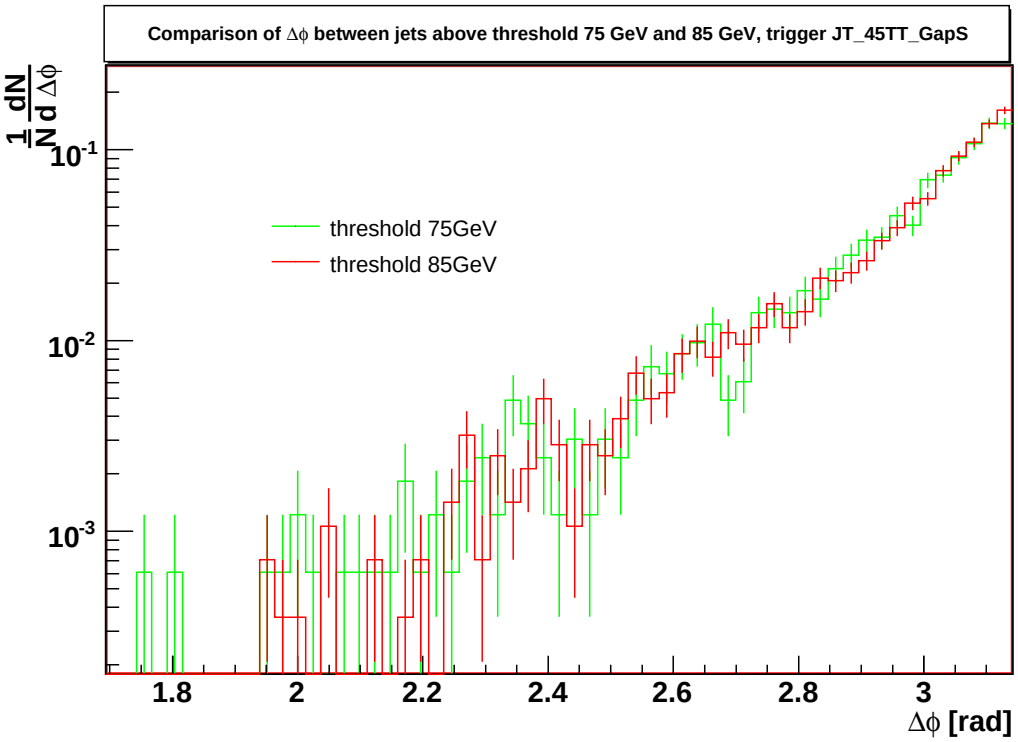

Figure 4.8: The comparison of $\Delta\phi$ spectra for jets passing the trigger JT_45TT_GapS with two different cuts on p_T.

Block (LBN) marked as good, i.e. time interval where the luminosity was correctly measured. Although the luminosity was not measured for diffractive jet triggers during the time period of data taking used in this analysis, events coming from these triggers are always associated to an LBN. We require all events, diffractive as well as inclusive, to come from good LBNs.

These basic criteria do not ensure yet, that the data are correctly reconstructed and that they come from hard $p\bar{p}$ collision. They only select events, which were taken with properly working detector. Therefore there must be additional selection criteria, which take into account the physical aspects of the collision and the reconstructed decay products. In this analysis, we follow the previous inclusive jet data $\Delta\phi$ studies done by the D0 collaboration ([33]) and the D0 Jet ID group recommendations on jet quality cuts ([31]) to ensure that jets are correctly found and reconstructed.

The event cuts used are:

- At least two jets within $|\eta| < 0.8$ must be reconstructed.
- Missing E_T must obey $\not{E}_T < 0.7 p_T$
- Primary vertex must be found within 50 cm from the center of the detector, $|z_{vtx}| < 50$, and number of tracks associated with this vertex is at least 3.

The jet ID cuts recommended by Jet ID group:

- Electromagnetic fraction: $0.05 <$ EMF < 0.95
- Coarse hadronic fraction: CHF < 0.4
- Hot cell fraction: HotF < 10
- n90 variable: n90 > 1
- Level 1 confirmation: $\frac{\text{l1set}}{p_T^{jet} * (1-\text{CHF})} > 0.4$ for EC and CC regions; > 0.2 for ICD region

EC region is defined as		|detector rapidity|	$>$	1.5
CC region as		|detector rapidity|	$<$	0.8
ICD region as	0.8 $<$	|detector rapidity|	$<$	1.5

All criteria are described in detail in next chapters.

Missing E_T Missing E_T ($\not\!\!E_T$) is a transverse energy which was not measured by the detector. This can be caused by neutrinos or other particles coming from hard interaction that escape from the detector without leaving their energy in it. In this case $\not\!\!E_T$ is usually small compared to the overall energy of the interaction. But missing E_T can also be used as an indication of non-hard processes, such as cosmic rays, hot cells or other electronics malfunctions, where $\not\!\!E_T$ can be very large. Cut on $\not\!\!E_T$ is introduced to remove such events from the analyzed sample.

Missing E_T is measured using calorimeter cells; it is computed as a sum of their energy, taken as a vector with direction from the calorimeter center to the cell position:

$$\begin{aligned} \not\!\!E_T &= |\sum \vec{E}_T^{cell}| \\ \vec{E}_T^{cell} &\equiv (E^x_{cell}, E^y_{cell}) = E_{cell}\ \sin\theta_{cell}\ (\cos\phi_{cell}, \sin\phi_{cell}) \end{aligned} \tag{4.6}$$

E_{cell}, θ_{cell} and ϕ_{cell} are energy deposited in the cell, polar and azimuthal angles of the cell, respectively. All cells with positive energy were used in the sum.

The cut is quite loose, it requires the missing E_T in the event to be less than 70% of the leading jet p_T. The distribution of missing E_T for inclusive and diffractive samples is shown in Fig.4.9 - 4.11. The green area is for events that passed all selection criteria, black line shows events that pass all criteria except the cut on $\not\!\!E_T$. The number of events which do not pass the cut is very low. This is mainly caused by the fact that other selection criteria (e.g. demand of two high p_T central jets) already remove most of the background. The efficiencies, measured as the ratio of number of events that pass all cuts and number of events that pass all criteria but the $\not\!\!E_T$ cut are shown in Table 4.4. All of them are almost 1 and so, it is not necessary to consider them in the analysis.

	$p_T > 25$ GeV	$p_T > 61$ GeV	$p_T > 75$ GeV
inclusive	0.9953	0.9989	0.9991
diffractive south	0.9995	0.9998	0.9997
diffractive north	0.9994	0.9995	0.9990

Table 4.4: Efficiencies for cut on missing E_T for different p_T regions in inclusive and diffractive samples.

Primary vertex selection The D0 tracking system allows to distinguish *primary* as well as *secondary* vertices in an event. Primary vertices comes directly from the $p\bar{p}$ interaction, secondary vertices are connected to decays of long-living particles.

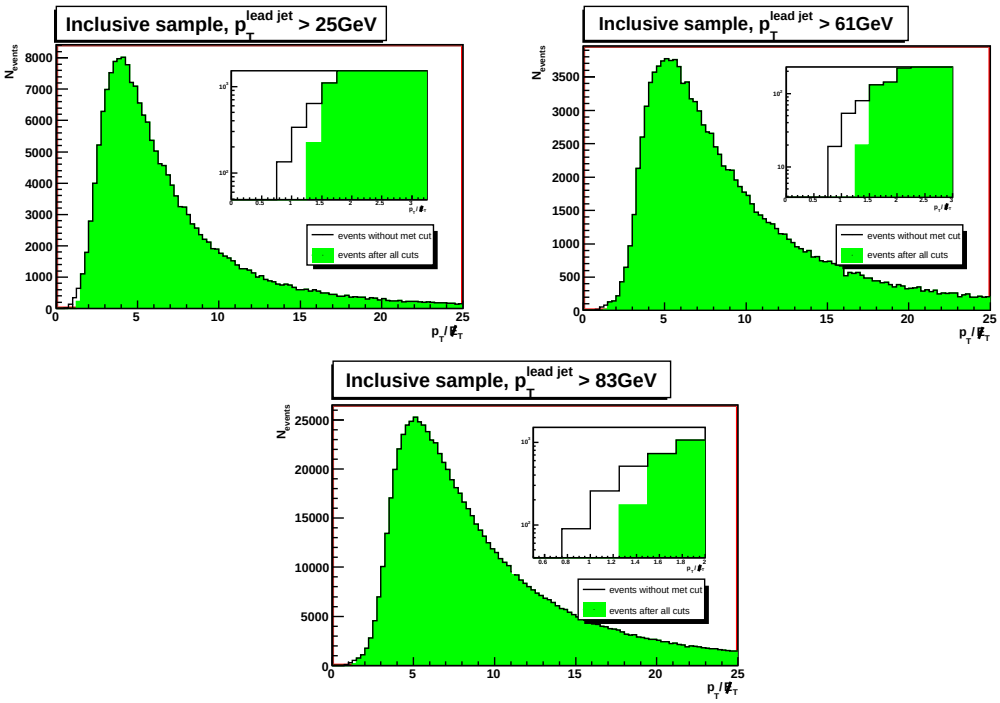

Figure 4.9: Distribution of missing $\not\!\!E_T$ for inclusive sample.

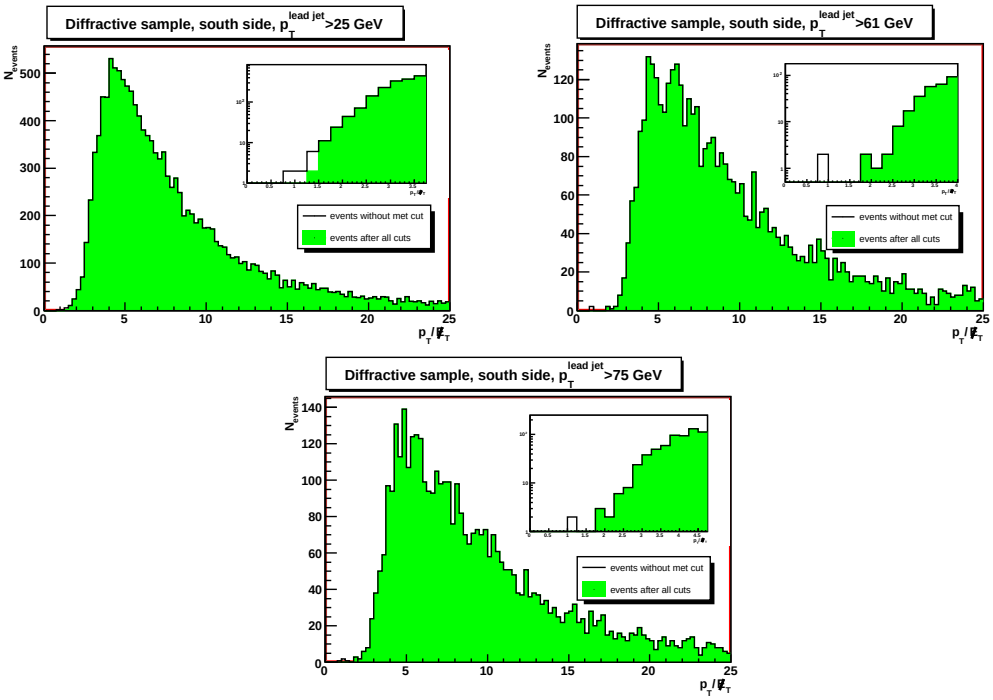

Figure 4.10: Distribution of missing $\not\!\!E_T$ for diffractive events with gap on the south side of the calorimeter.

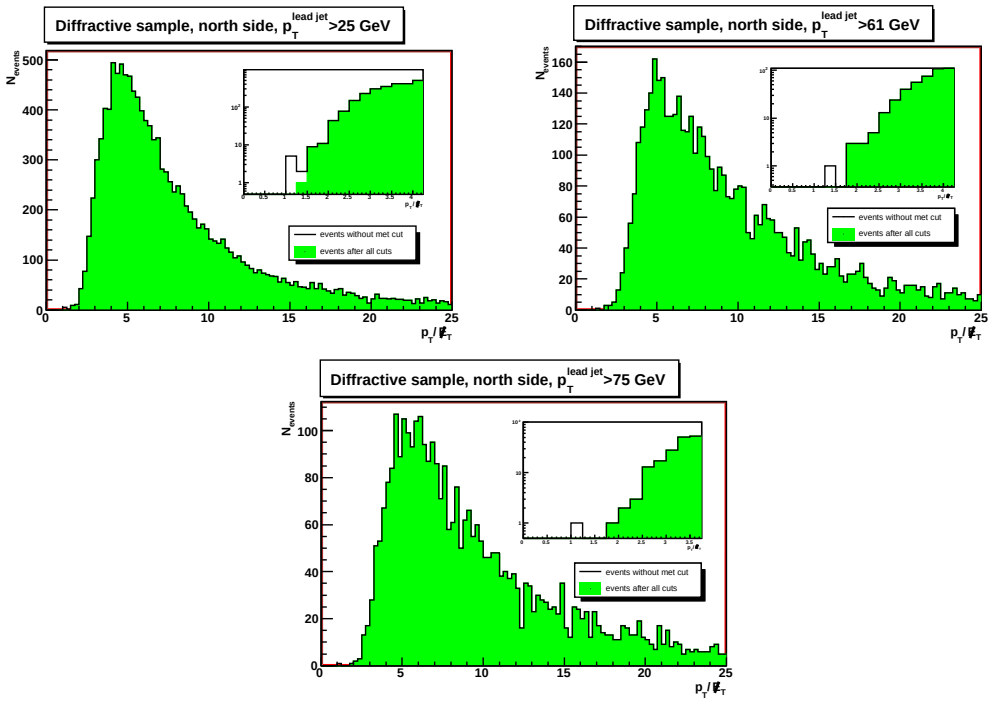

Figure 4.11: Distribution of missing $\not\!\!E_T$ for events with gap on the north side of the calorimeter.

Requirement of presence of a good primary vertex enhances the event selection by better detector read-out and computing correct jet properties (rapidity, transverse momentum).

Two independent cuts are applied on the primary vertex. The first one removes events, the primary vertex of which occurs at the end of central Silicon Microstrip Tracker, by cutting all events further than 50 cm from the center of the detector. This also helps to improve projection of calorimeter towers to the primary vertex. The second cut ensures a good quality of found primary vertex. It requires some number of tracks reconstructed by the D0 tracker associated with the vertex. For data, reconstructed with p14 PASS 2 release used in this analysis, the cuts are set to $|z_{vtx}| < 50cm$ and $n_{tracks} \geq 3$.

Figures 4.12 - 4.14 shows the distribution of primary vertex position. The influence of the cut on $\Delta\phi$ distribution is shown in Fig. 4.15-4.17. The plots show that the cut does not change the $\Delta\phi$ distribution.

EMF Jets are propagated through calorimeter and, in general, they are spreaded in both electromagnetic and hadronic parts. Electromagnetic fraction variable gives a ratio of jet transverse energy, which was deposited in electromagnetic part of

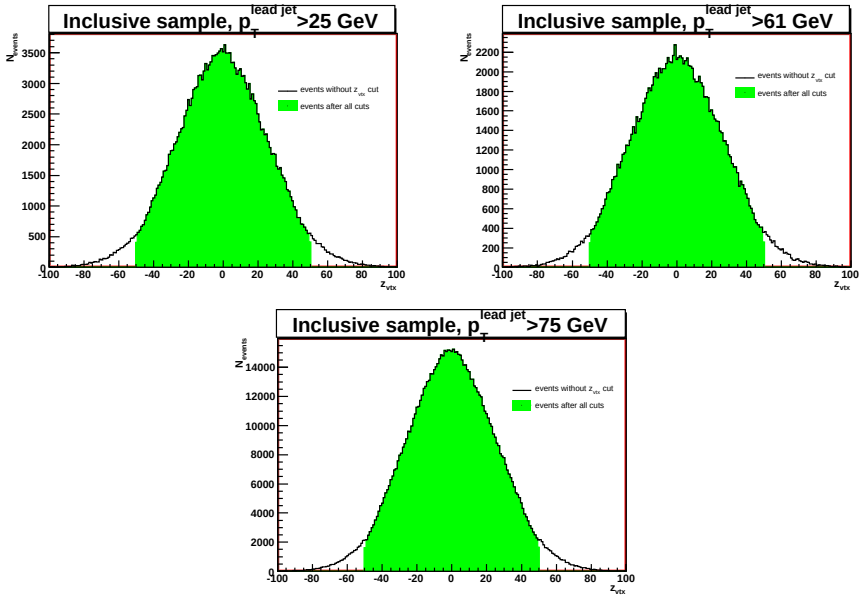

Figure 4.12: Distribution of z-coordinate of primary vertex. Green area shows events after both primary vertex cuts (number of vertices and z cut) for events from inclusive sample. Black curve shows the distribution for inclusive events without any primary vertex cut.

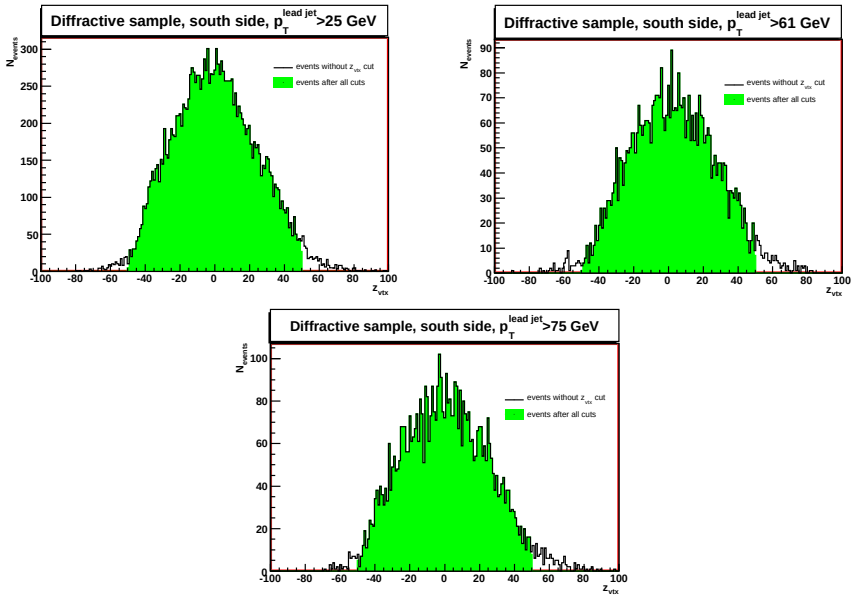

Figure 4.13: Distribution of z-coordinate of primary vertex. Green area shows events after both primary vertex cuts (number of vertices and z cut) for events with gap on the south side of the calorimeter. Black curve shows the distribution for south diffractive events without any primary vertex cut.

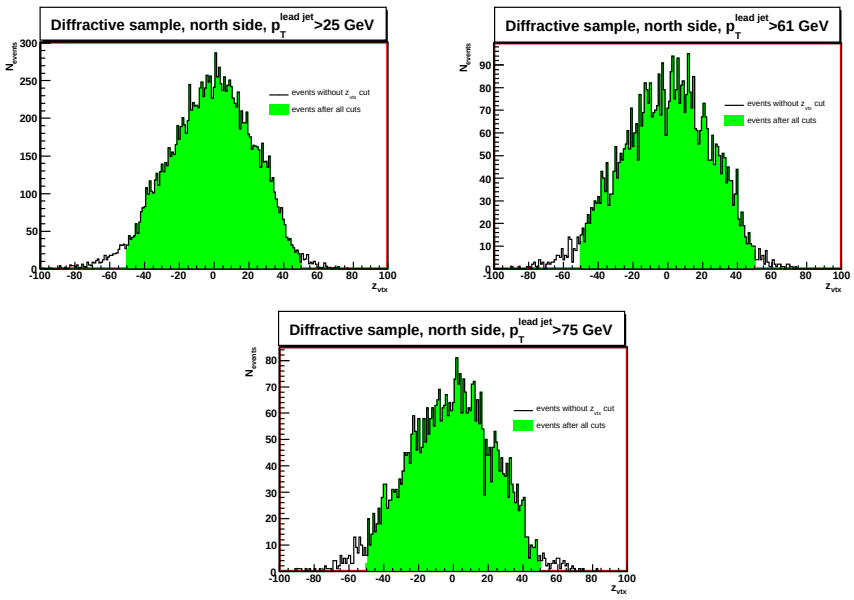

Figure 4.14: Distribution of z-coordinate of primary vertex. Green area shows events after both primary vertex cuts (number of vertices and z cut) for events with gap on the north side of the calorimeter. Black curve shows the distribution for north diffractive events without any primary vertex cut.

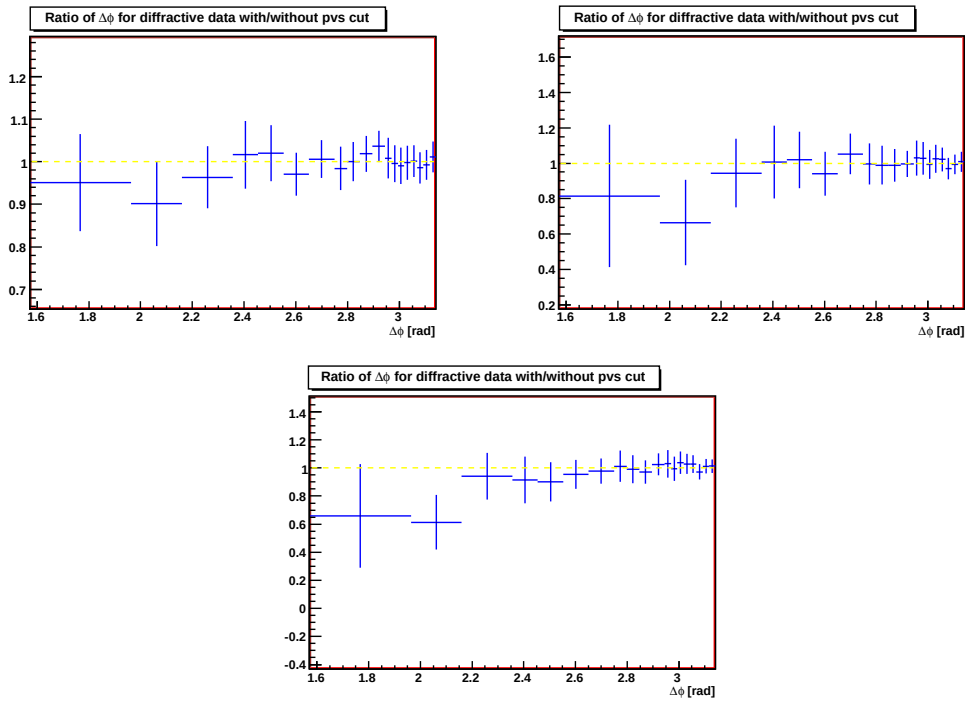

Figure 4.15: The ratio of $\Delta\phi$ distributions of diffractive jets with gap on the south side for data with and without all but primary vertex cuts.

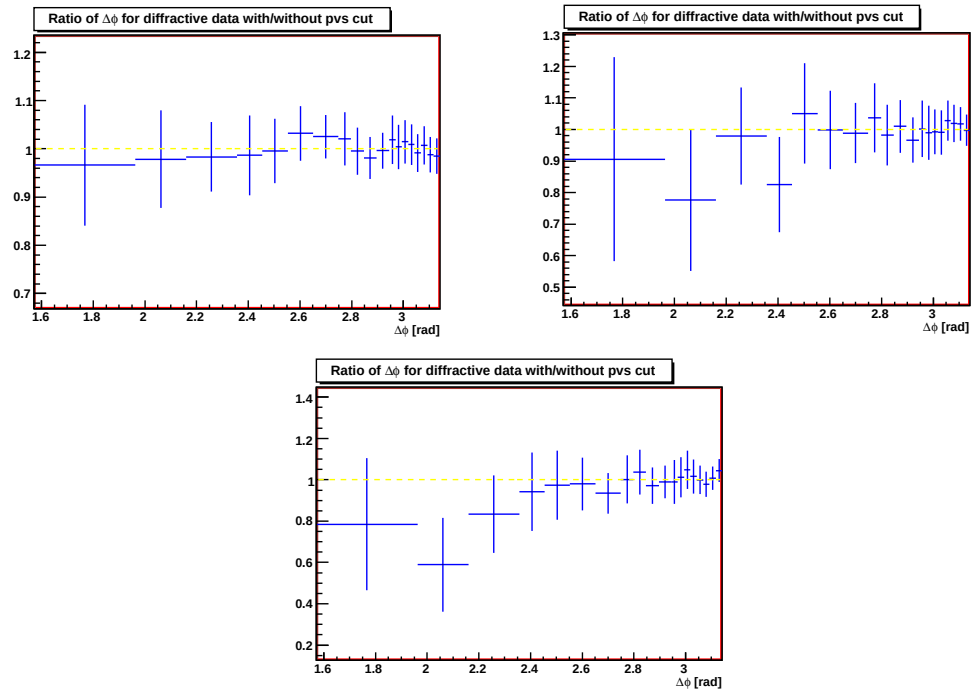

Figure 4.16: The ratio of $\Delta\phi$ distributions of diffractive jets with gap on the north side for data with and without all but primary vertex cuts.

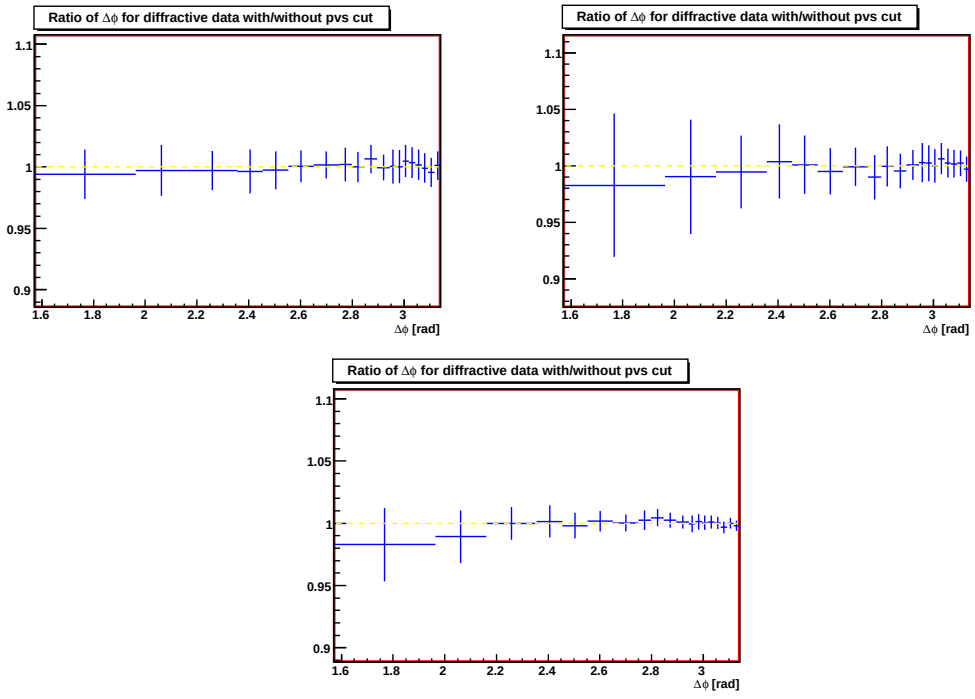

Figure 4.17: The ratio of $\Delta\phi$ distributions of inclusive jets for data with and without all but primary vertex cuts.

calorimeter. From theory and from known properties of D0 calorimeter, EMF for a typical jet is ≈ 0.5 (50%). But even very far values from this mean are not uncommon. The distribution of EMF for leading jet is shown in Fig. 4.18. The cut is set to

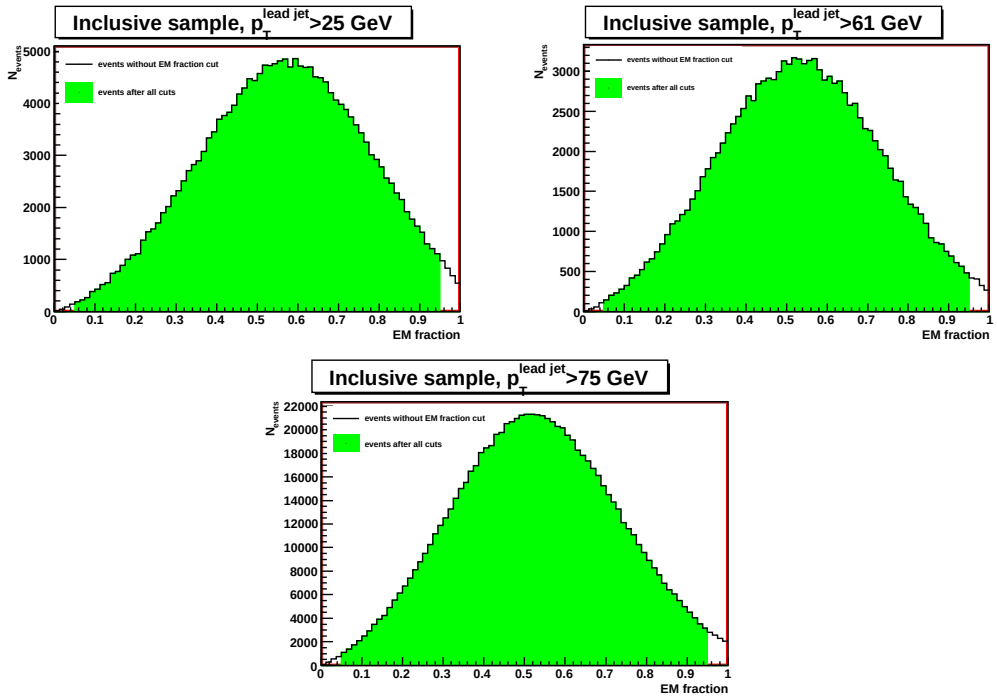

Figure 4.18: Distribution of EMF for leading jet in inclusive sample.

$0.05 < \text{EMF} < 0.95$. The lower cut removes jets with no detected electromagnetic particles (this cut removes very small number of events, as seen in figures), while the upper cut is introduced to reject jets made almost inclusively of EM particles (mainly when only one electron or photon makes the 'jet').

	$p_T > 25$ GeV	$p_T > 61$ GeV	$p_T > 75$ GeV
inclusive	0.9837	0.9873	0.9871
diffractive south	0.9728	0.9843	0.9879
diffractive north	0.9733	0.9788	0.9834

Table 4.5: Efficiencies for cut on electromagnetic fraction for different p_T regions in inclusive and diffractive samples.

CHF Similarly to EMF variable, coarse hadronic fraction means a fraction of jet transverse energy deposited in the coarse hadronic part of the calorimeter. The distribution of the variable is shown in Fig.4.21. Coarse hadronic calorimeter width

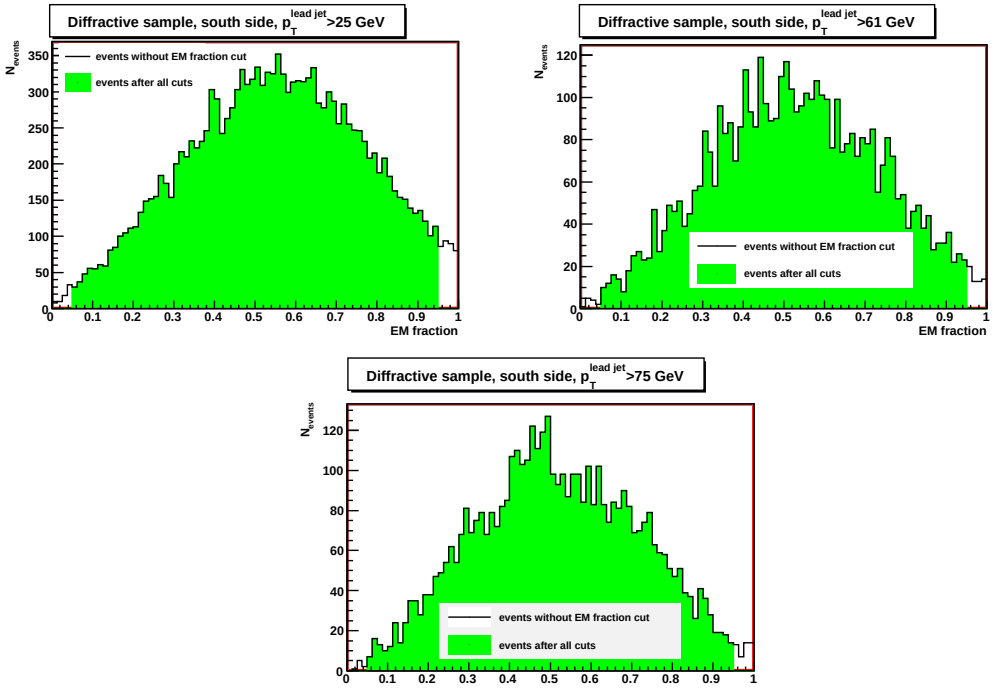

Figure 4.19: Distribution of EMF for leading jet in diffractive sample for events with gap on south side.

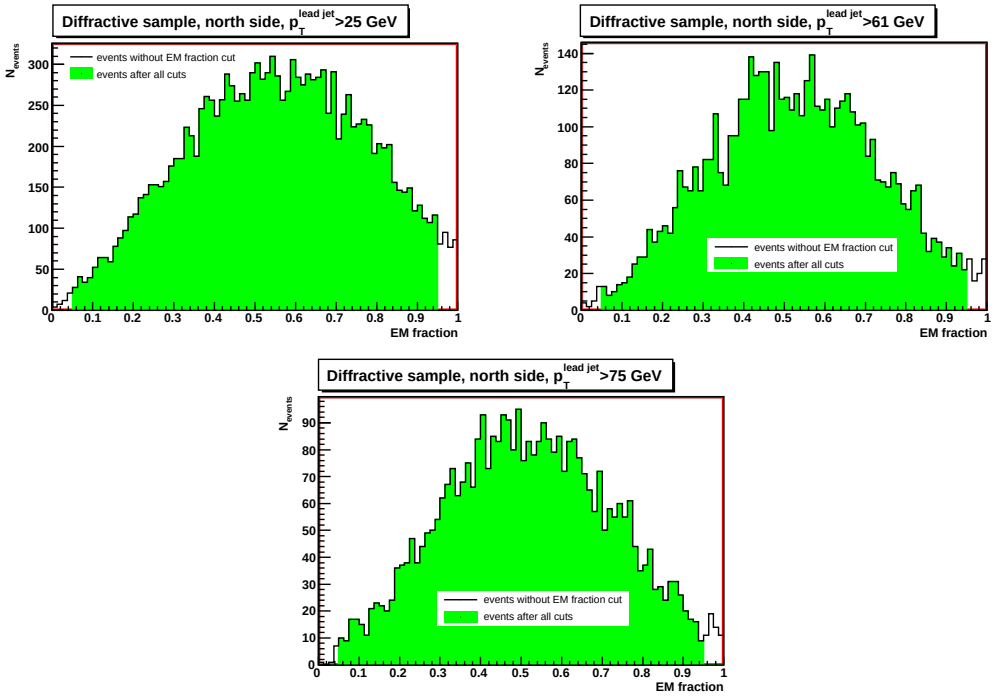

Figure 4.20: Distribution of EMF for leading jet in diffractive sample for events with gap on north side.

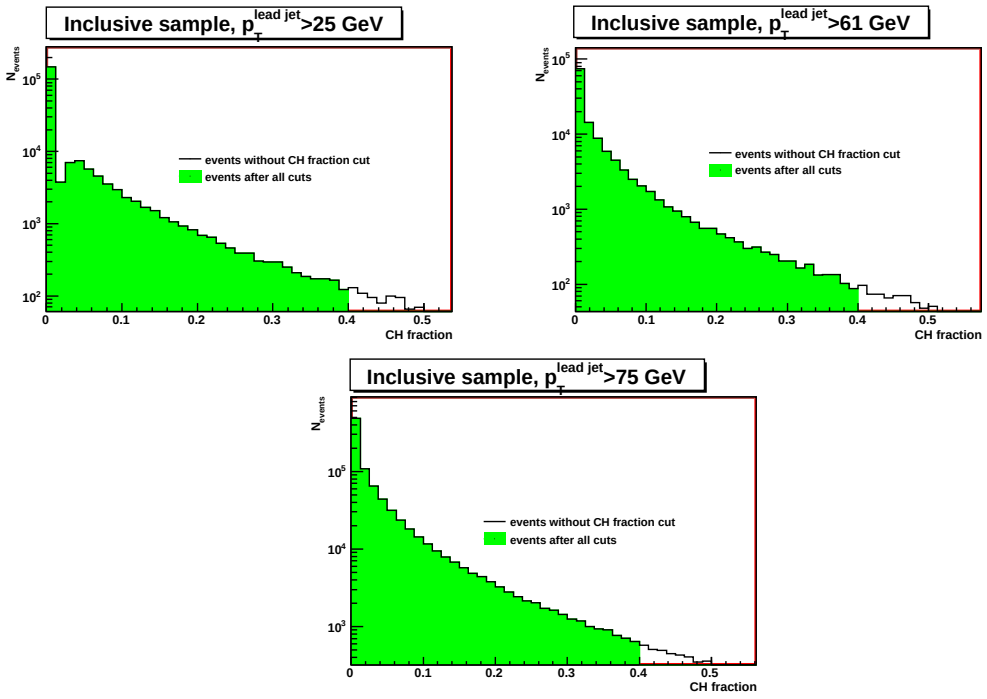

Figure 4.21: Distribution of coarse hadronic fraction for leading jet in inclusive sample.

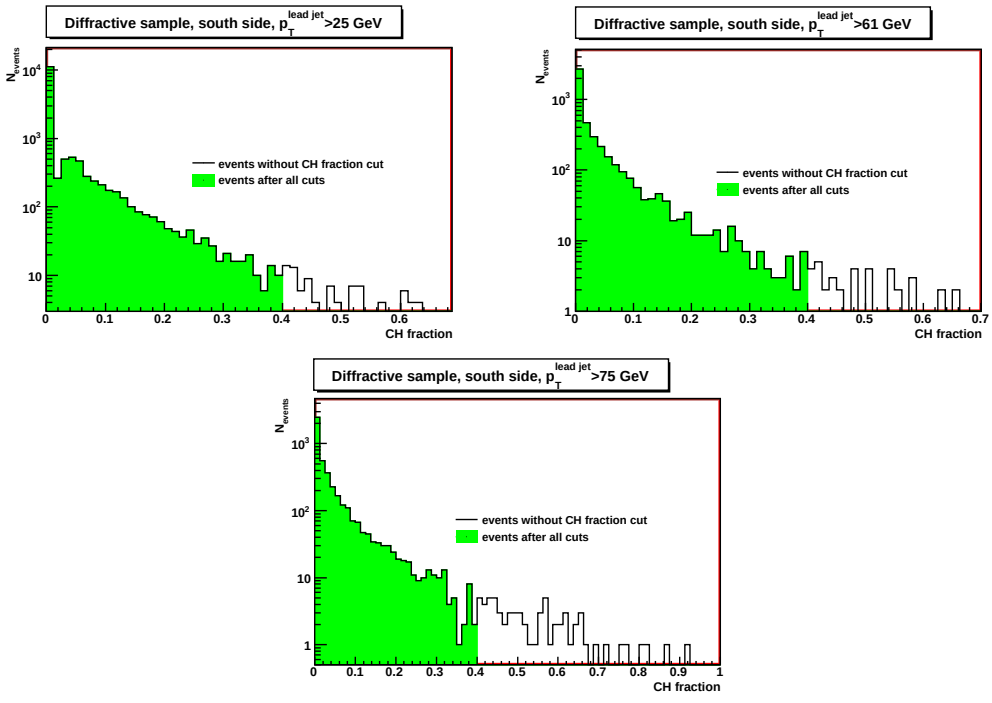

Figure 4.22: Distribution of coarse hadronic fraction for leading jet in diffractive sample for events with gap on south side.

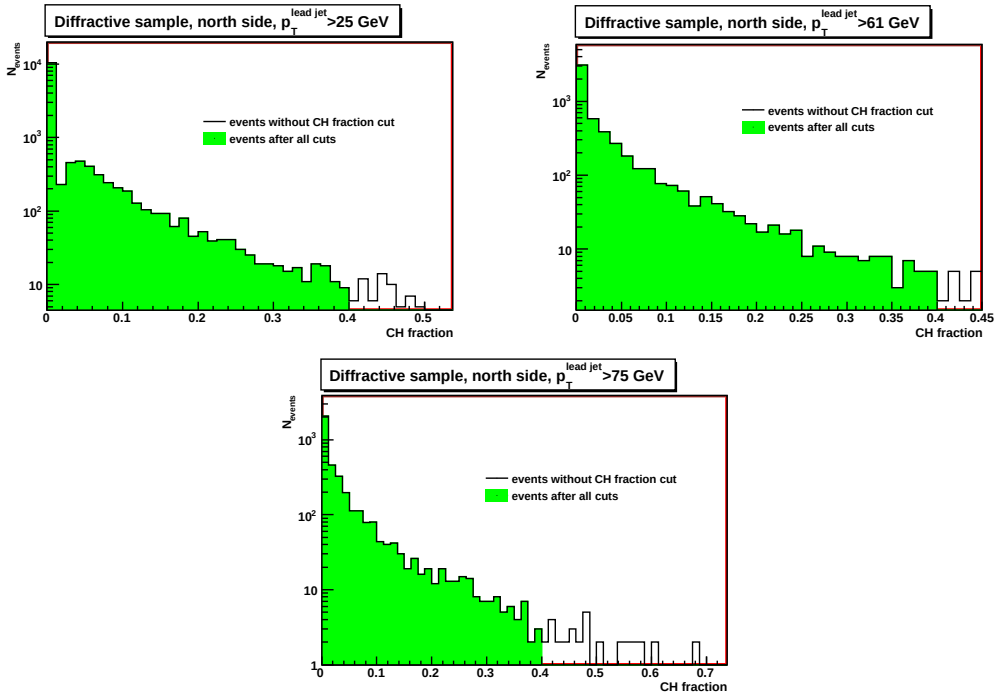

Figure 4.23: Distribution of coarse hadronic fraction for leading jet in diffractive sample for events with gap on north side.

is $4\lambda_I$, so using the theory we can assume that a typical jet should deposit about 2% of its energy in this part of calorimeter, which is in a good agreement with the plots. The reason why this behaviour is different from previous studies [22] is probably in a new read-out algorithm of the calorimeter (see Calorimeter chapter), where T42 algorithm was used.

	$p_T > 25$ GeV	$p_T > 61$ GeV	$p_T > 75$ GeV
inclusive	0.9934	0.9916	0.9921
diffractive south	0.9927	0.9903	0.9853
diffractive north	0.9927	0.9895	0.9891

Table 4.6: Efficiencies for cut on coarse hadronic fraction for different p_T regions in inclusive and diffractive samples.

HotF Hot cell fraction is defined as a ratio of the transverse energy of the most energetic calorimeter cell in the jet to the second most energetic cell transverse energy. This cut removes jets, energy of which is dominated by only one hot cell, which was not removed by a calorimeter hot cell killer. The distribution of HotF is

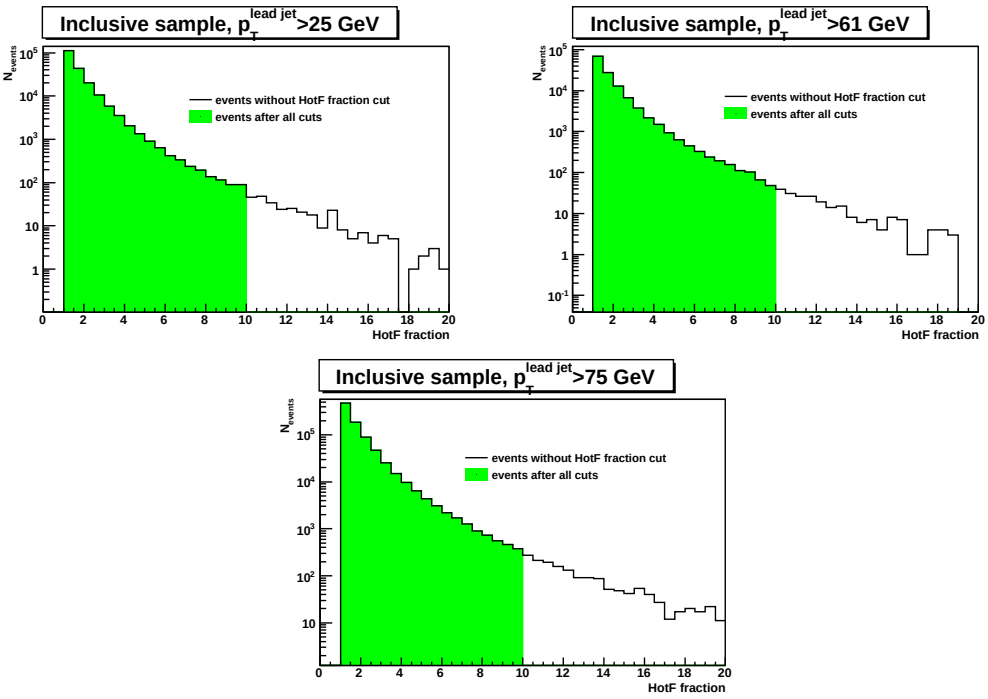

Figure 4.24: Distribution of hot cell fraction for leading jet in inclusive sample.

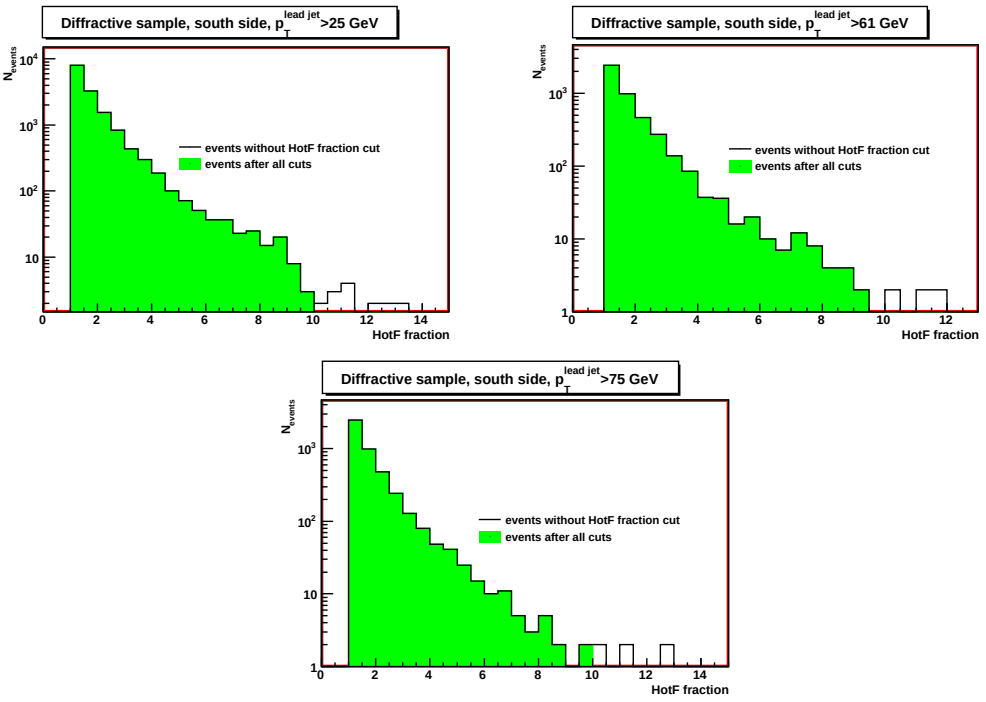

Figure 4.25: Distribution of hot cell fraction for leading jet in diffractive sample for events with gap on south side.

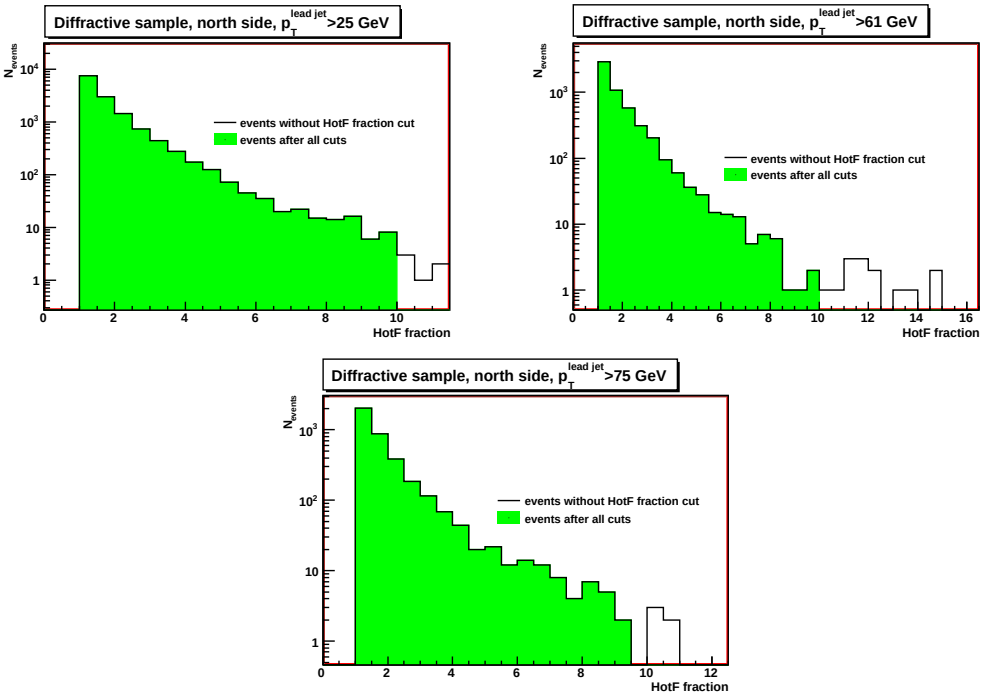

Figure 4.26: Distribution of hot cell fraction for leading jet in diffractive sample for events with gap on north side.

shown in Fig. 4.24. A cut is quite loose and assumes the hot cell fraction less than 10.

	$p_T > 25$ GeV	$p_T > 61$ GeV	$p_T > 75$ GeV
inclusive	0.9986	0.9983	0.9982
diffractive south	0.9986	0.9983	0.9980
diffractive north	0.9983	0.8874	0.9982

Table 4.7: Efficiencies for cut on hot cell fraction for different p_T regions in inclusive and diffractive samples.

n90 Variable n90 is used to describe transversal behaviour of the jet. It counts a number of calorimeter towers, which hold 90% of the jet transverse energy. To do this, towers are ordered by transverse energy and summed up until the required energy is achieved. A distribution of this variable is shown in Fig. 4.27. A cut is very loose, it requires a jet to be built-up of more than one calorimeter tower (it would be probably a hot tower) n90 > 1.

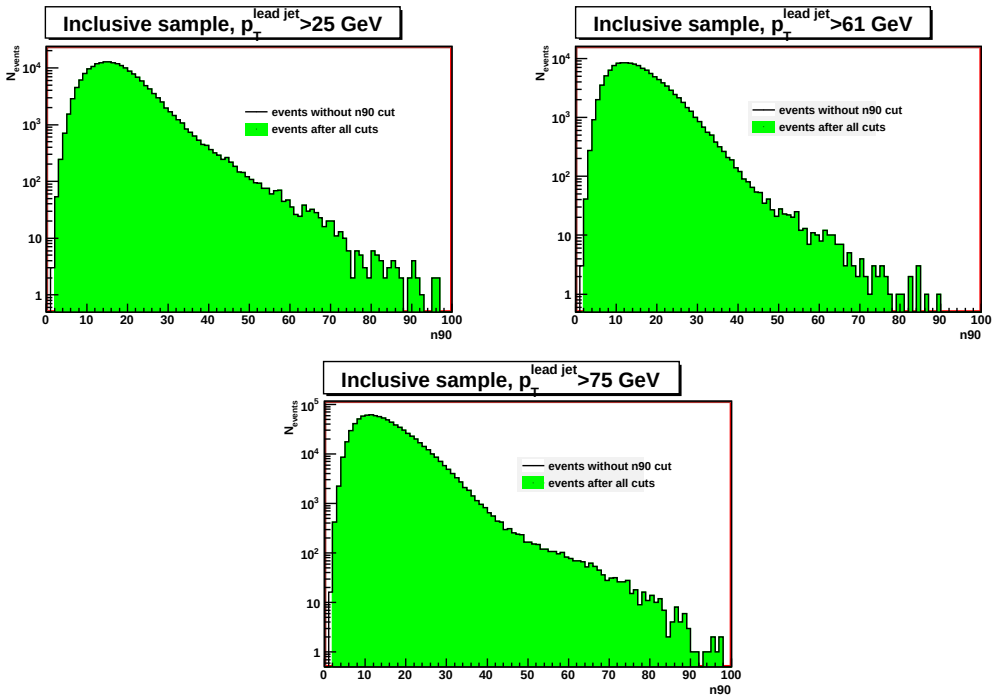

Figure 4.27: Distribution of n90 variable for leading jet in inclusive sample.

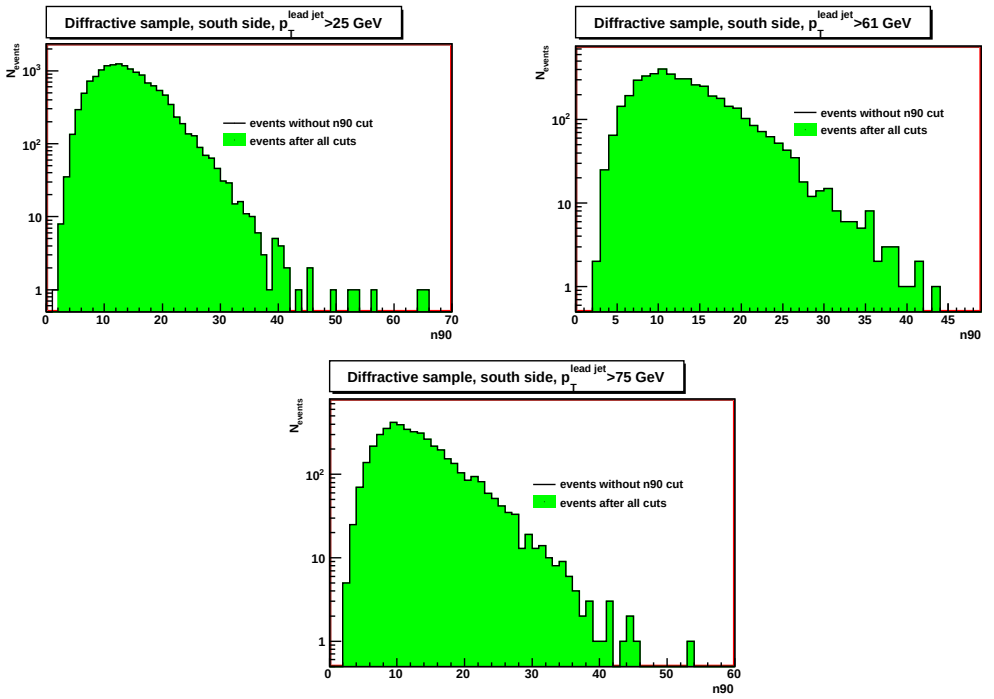

Figure 4.28: Distribution of n90 variable for leading jet in diffractive sample for events with gap on south side.

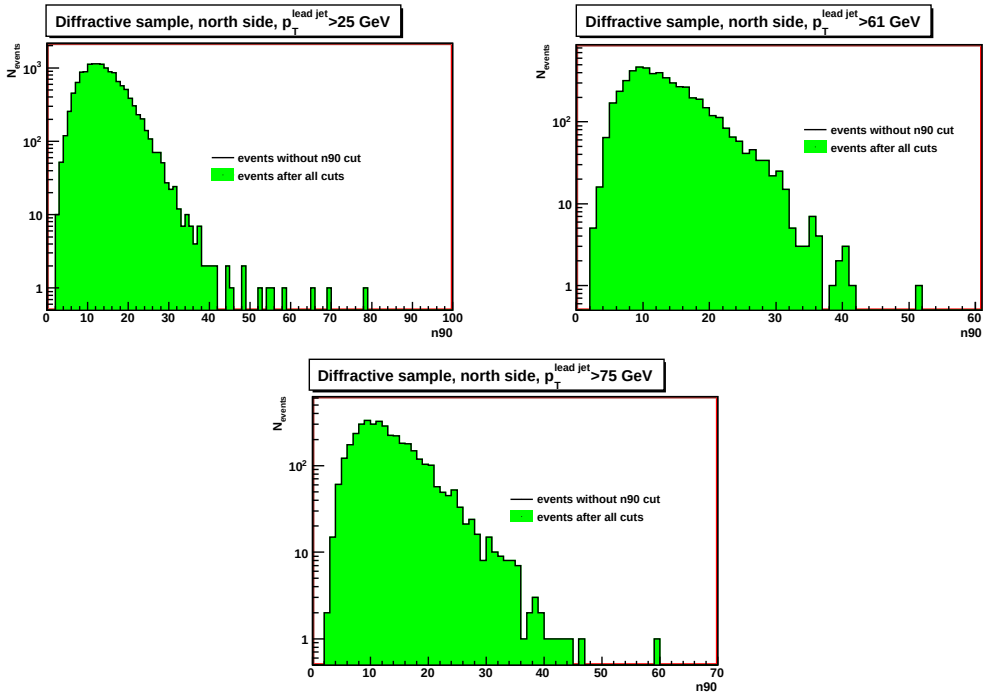

Figure 4.29: Distribution of n90 variable for leading jet in diffractive sample for events with gap on north side.

	$p_T > 25$ GeV	$p_T > 61$ GeV	$p_T > 75$ GeV
inclusive	0.9999	0.9999	0.9999
diffractive south	1	1	1
diffractive north	1	1	1

Table 4.8: Efficiencies for cut on hot cell fraction for different p_T regions in inclusive and diffractive samples.

L1 confirmation Level 1 confirmation cut was introduced for p14 release of D0 reconstruction software. The L1 jets are reconstructed from calorimeter towers energy, measured on first trigger level, using a cone algorithm in the direction of jet with R = 0.5. L1SET - Level 1 scalar transverse energy - is computed from these jets. Energy of coarse hadronic part of calorimeter is not included in the reconstruction, because CH is not read out in L1 calorimeter triggers. P_T of the L1 jets is not corrected with Jet Energy Scale for the purpose of this cut. The cut depends on p_T, coarse hadronic fraction and also on the direction of the jet (it is different for ICD and other calorimeter regions) as described earlier.

The distribution of variable L1SET/[P_T(1-CHF)] is shown in Fig. 4.30 - 4.32.

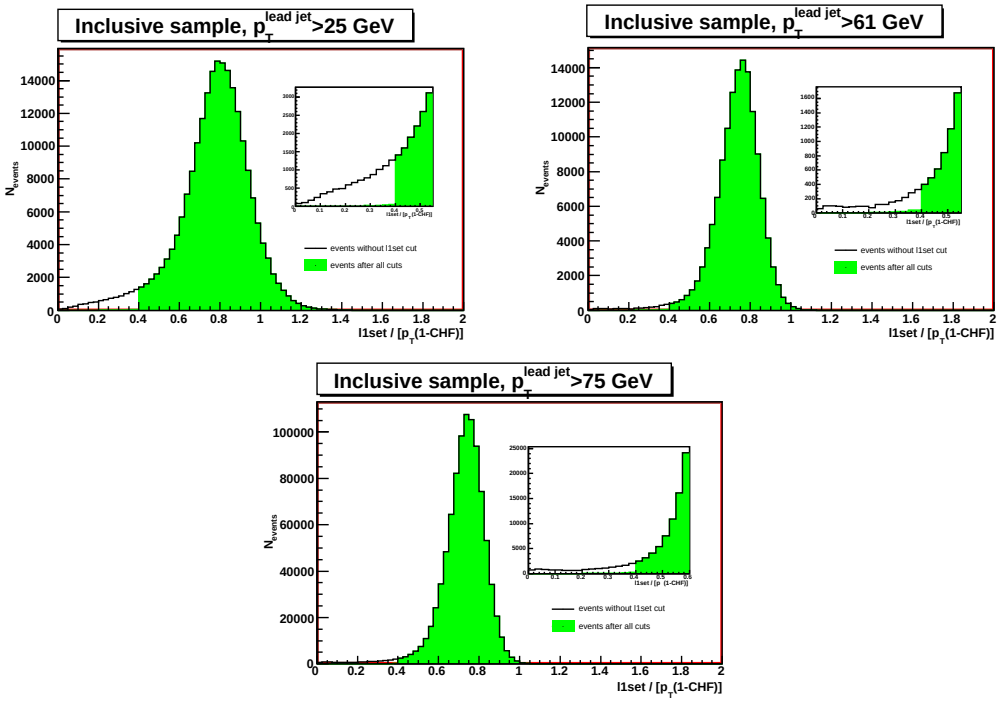

Figure 4.30: Distribution of L1 confirmation variable for leading jet in inclusive sample.

The inclusive sample does not show any strange behaviour under the cut for low p_T events, but there is a small increase in low values of the variable for higher p_T's.

In Fig. 4.33- 4.35, we can see how this cut, together with all other jet ID cuts, influences the $\Delta\phi$ distribution. While none of the other cuts changes the shape of the $\Delta\phi$ distribution, the L1 confirmation cut alters the inclusive distribution considerably. There is no such change for diffractive triggers. Both these properties correspond well with previous study in [33]. This study showed that jets rejected by L1 cut are fake jets and thus the cut does not influence the efficiency.

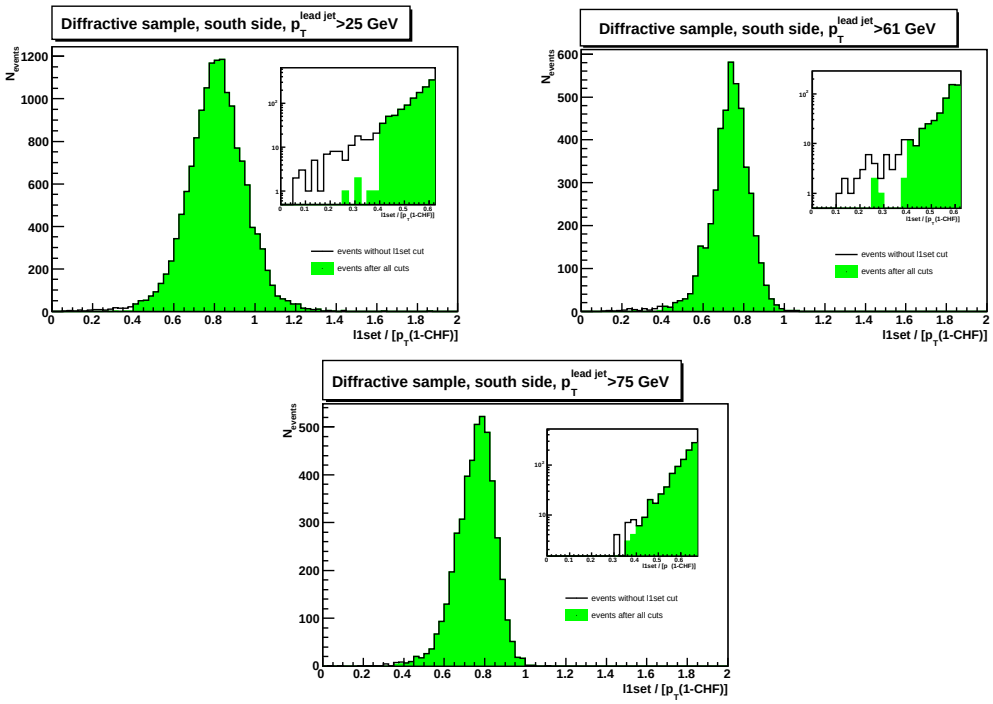

Figure 4.31: Distribution of L1 confirmation variable for leading jet in diffractive sample for events with gap on south side.

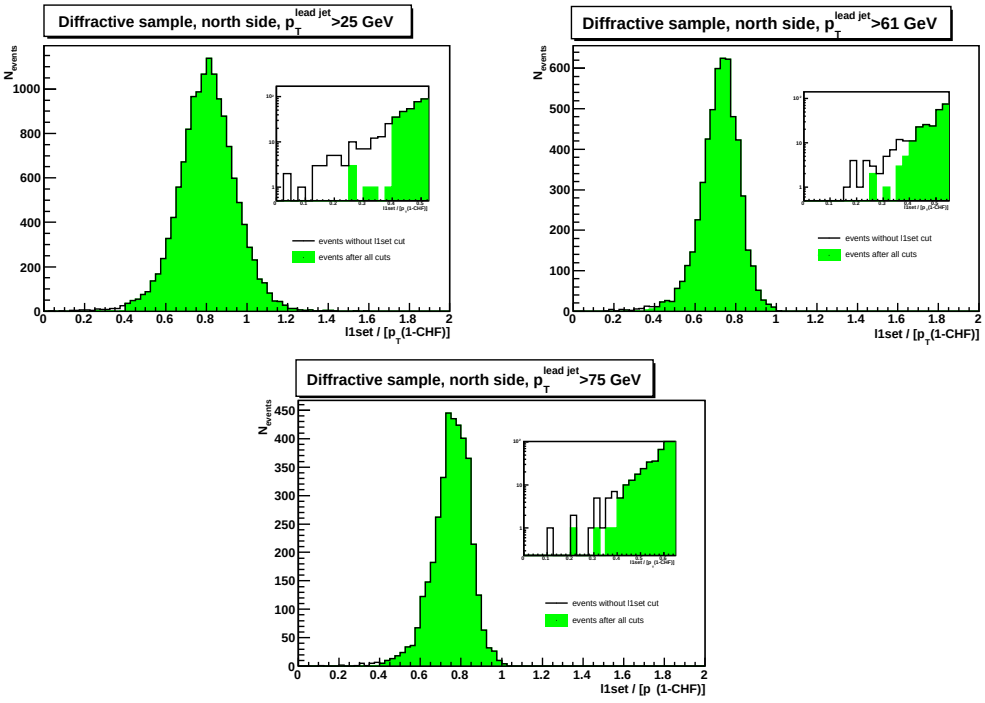

Figure 4.32: Distribution of L1 confirmation variable for leading jet in diffractive sample for events with gap on north side.

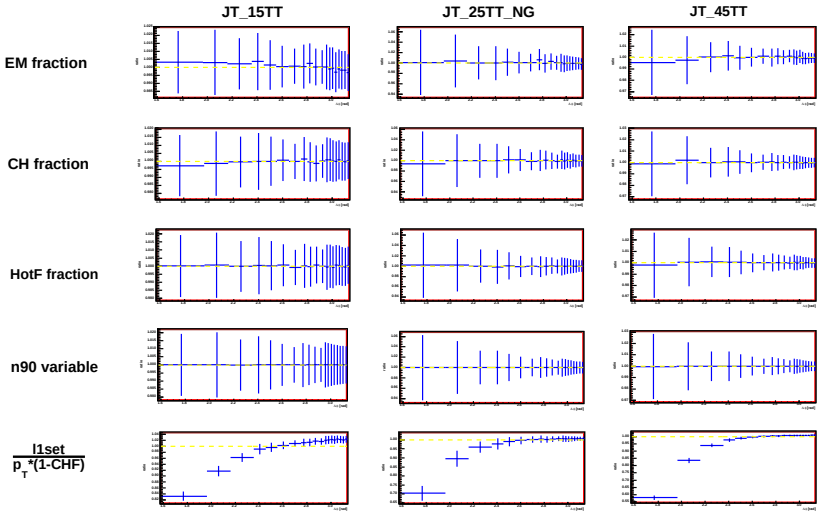

Figure 4.33: Ratios of $\Delta\phi$ distributions for various jet ID cuts for inclusive data sample. Each plot is a ratio of $\Delta\phi$ distribution with to without the given jet ID cut.

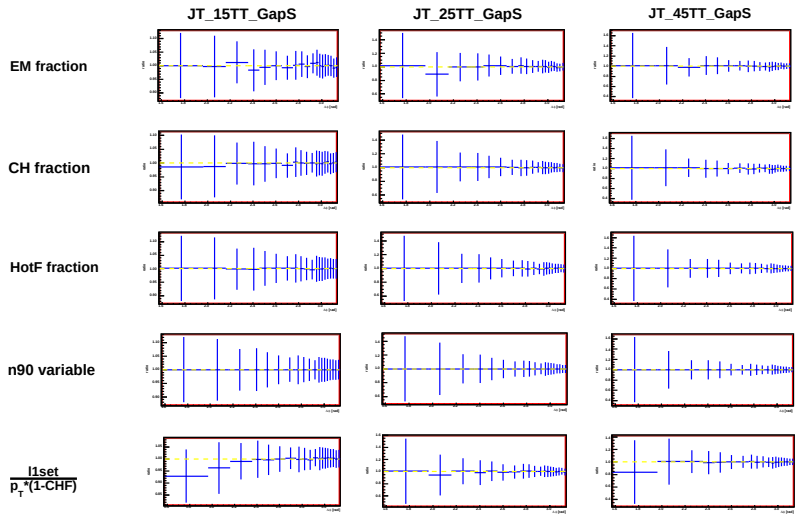

Figure 4.34: Ratios of $\Delta\phi$ distributions for various jet ID cuts for south diffractive data sample. Each plot is a ratio of $\Delta\phi$ distribution with to without the given jet ID cut.

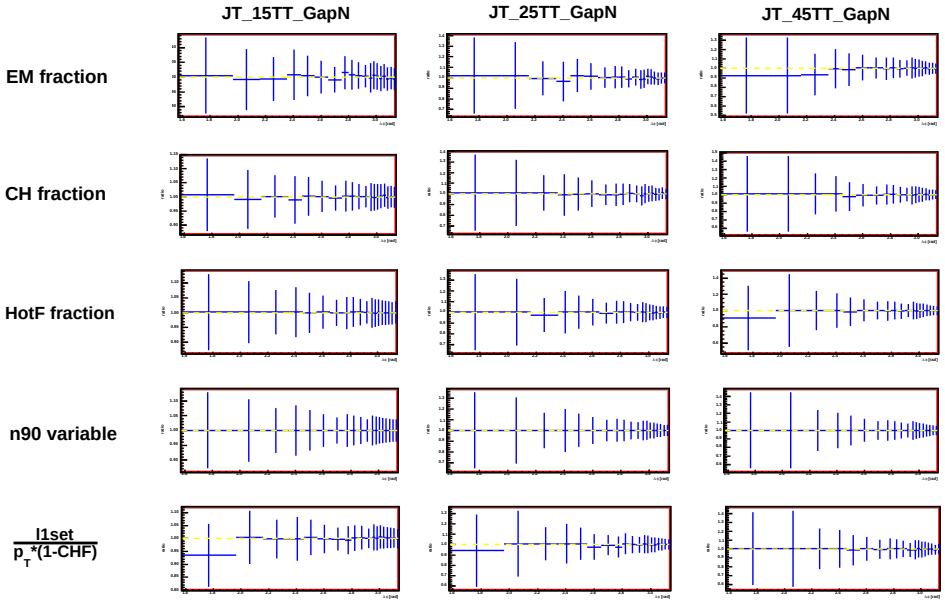

Figure 4.35: Ratios of $\Delta\phi$ distributions for various jet ID cuts for north diffractive data sample. Each plot is a ratio of $\Delta\phi$ distribution with to without the given jet ID cut.

Chapter 5

Gap Definition

A method of a *rapidity gap* was used to select the diffractive events from the full sample recorded by the D0 experiment. This approach is based on the fact, that particle production near the direction of intact proton or antiproton is highly suppressed by the dynamics of diffractive interactions (see chapter 2). This method is not as precise as a direct proton measurements performed by the Forward Proton Detector, yet it is commonly used in a high energy physics experiments[1].

A rapidity gap is not uniquely determined and there are many possibilities to define it. As described in chapter 2, the size of the gap differs event by event according to the value of pomeron ξ. The lower ξ, the bigger the gap. It means that for higher ξ events, the gap can be too small to be measured by the detector.

The idea, how to define a rapidity gap, used in this analysis, is to choose a *fixed* region in the calorimeter and search for an upper limit on the energy deposited in this region. As written above, the gap size changes with each event, so using the fixed part of the calorimeter is not directly a searching for a rapidity gap as a region devoid of all particles, but looking for a rapidity interval with *a low energy activity*. The low energy activity region in the calorimeter will be reffered to as a *gap* throughout the thesis. The energy limit then serves as a definition of the low activity.

The energy measured in the calorimeter can also originate from the electronics noise. This extra energy could disable to locate the rapidity gap, if we were looking for a rapidity interval with *zero energy*, even though there were no particles in the region. The electronics noise cannot be completely suppressed, so it introduces another reason to set up some upper limit on the energy that is deposited in the region and which is considered to originate from the noise.

[1] At the time of writing of this thesis, the FPD data were not yet analyzed.

Two parts of the D0 detector are used in order to define a gap - the luminosity monitor (LM) and the calorimeter. When LM is not fired[2], i.e. does not detect the proton remnants or any other particles going out of the interaction under a small angle, it is a first indication for the diffractive candidate. If the LM condition is satisfied, the energy deposited in the given forward region on the corresponding side of the calorimeter is measured and if it is lower than the limit, the event is considerd to come out of the diffractive interaction.

5.1 Cell Energy

Only cells that correctly measure energy can be used in the analysis. A distribution of cell energy of several million events is shown in Figures 5.1 and 5.2. It is clear that under a certain value, the distribution suddenly drops and does not correspond to a correct behaviour of cell measurement. The exact value is not sure from the plots. A further analysis showed that the dependence of physical measurements on the exact value (around the maximum) is small, so the limit was set to 0.1 GeV for cells in EM region and 0.2 GeV for FH region. Cells with lower energy are not included in the analysis.

5.2 Event Selection

Three types of data are used in the gap definition analysis:

1. *A noise sample* - the data taken by the detector in the time, when there is no interaction. It measures the noise that appears in the calorimeter.

2. *An inclusive sample* - the data with at least two well reconstructed jets and satisfying the event selection criteria described in chapter 4.

3. *A diffractive sample* - similar to *the inclusive sample*, with additional condition on LM detector, which must be off at least on one side.

The noise sample shows a typical behaviour of the energy deposited in the calorimeter, during the time when there is a proton bunch crossing but there is no

[2]If south disk of the luminosity monitor is fired, the level 1 trigger And/Or term *lms* is set on, if north side is fired, the And/Or term *lmn* is set on. If both lms and lmn are set on, the level 1 And/Or term FastZ is set on.

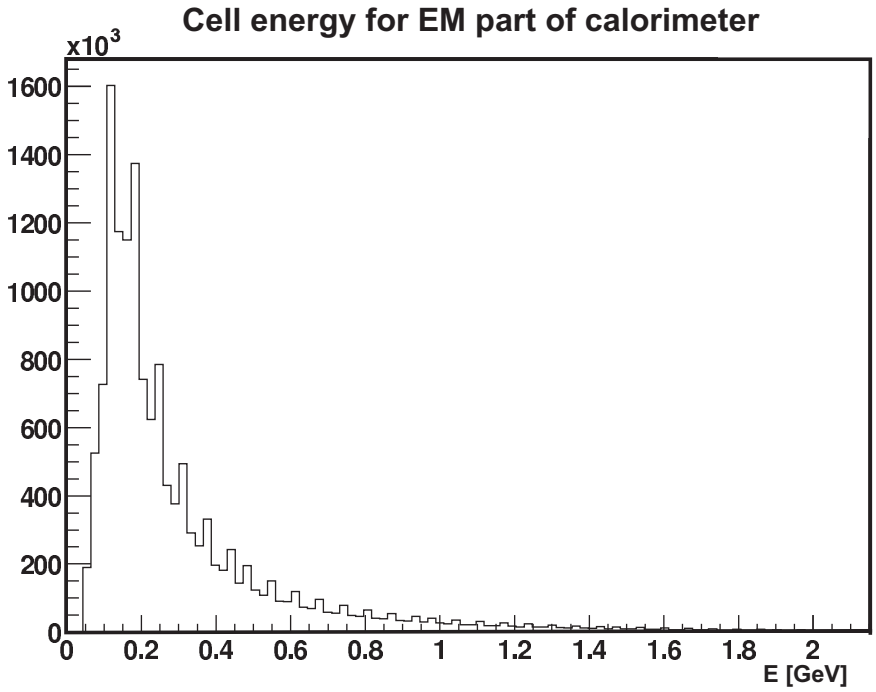

Figure 5.1: Energy distribution of cells from forward EM part of calorimeter.

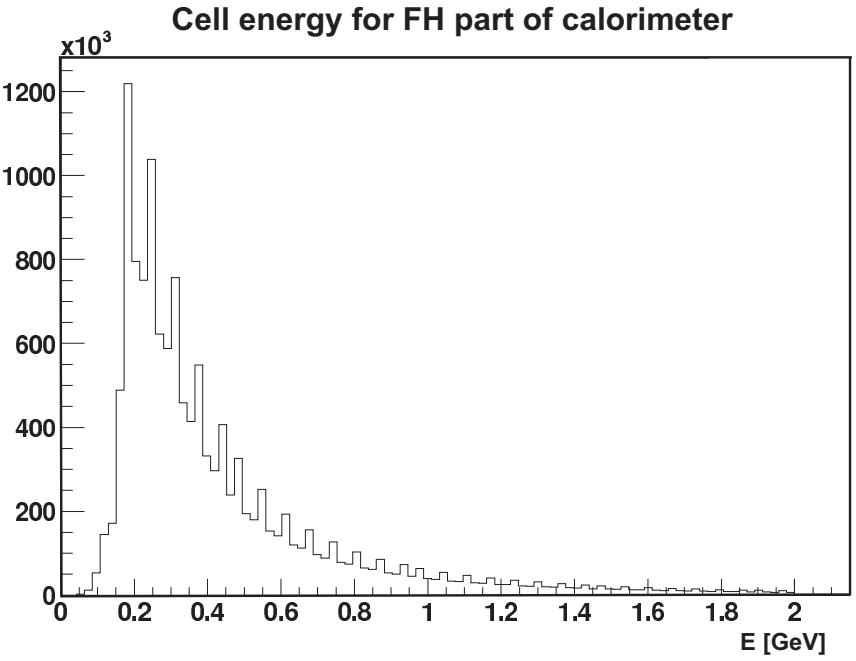

Figure 5.2: Energy distribution of cells from forward FH part of calorimeter.

deep inelastic interaction. Deep inelastic scattering (DIS) is accompanied by an origin of many particles coming from the collision, forming jets and captured mainly in the calorimeter. The interaction point can be reconstructed from particle tracks and using the tracks it is also possible to find other vertices, which come from the decays of primary particles. The noise sample should avoid all these indicators of DIS, therefore the conditions for the noise sample are: zero bias trigger on, all LM and/or terms off, no reconstructed primary vertex and no reconstructed jets.

On the contrary, the inclusive sample serves to show the behaviour of the calorimeter, when there is a *real physical collision*. The conditions for this are: one of the inclusive jet triggers (see chapter 4) is fired, at least one primary vertex with 3 or more tracks is reconstructed and the LM and/or terms lms, lmn and fastZ are on.

The conditions on the diffractive sample differ from the inclusive one in the trigger selection. The diffractive jet triggers are used for this sample, i.e. the LM and/or terms fastZ and either lms or lmn are off.

5.3 Energy Sum

In order to find the suitable rapidity interval and the upper energy limit for the gap definition, it is necessary to examine the energies deposited in various calorimeter regions by the three samples described above. As it is not clear whether the south and north sides of the calorimeter behave in the same way, all energy distributions are examined separately for both sides. Energy is summed over all cells in an area with energy above the threshold (0.1 GeV for EM, 0.2 GeV for FH). The common logarithm of the energy sum is used on x-axis in all plots for better distinctness and all plots are normalized to 1.

First two plots (Fig. 5.3-5.4) show the sum of the energy for so called *eta rings*, i.e. cells with a given ieta[3] and arbitrary azimuthal angle. Only south side of the calorimeter is shown. There are several aspects of the plots, which should be noticed and which are valid for all energy sum plots in this section:

1. Sharp edge of all distributions at -1 corresponds to the fact that there is a minimum cut on cell energy 0.1 and a common logarithm of the energy sum is used on the x-axis.

2. There are events in the inclusive sample with very low energy deposited in the forward region. This is not surprising for eta rings, as the azimuthal angle of

[3]For ieta definition see Table 3.2.3

one unit of calorimeter rapidity (ieta) is very low, but this property is generally valid for all regions (see plots below).

3. There are events in the noise sample with high energy spreaded in the forward region. Even in this small rapidity region, the energy sum can achieve tens of GeV (hot cells are removed from the sample!). This legitimizes the idea of looking for a fixed rapidity region with some fixed limit on the energy instead of looking for a region with no energy. The reason is in electronics noise, cosmic rays or pile-up events.

4. The shapes of all three distributions are roughly the same for all ieta rings, except the last two, ieta = 36 and ieta = 37.

The fourth property corresponds to the fact that proton remnants can spread to the cells closest to the beam tube and thus to change the distribution of energy deposited in the region.

The gap definition, which we are looking for, is to find a forward region with low energy activity. Because of the strange behaviour of cells close to the beam pipe, it seems to be a good idea to investigate also regions that excludes the very forward cells, i.e. regions which ends with cells ieta = 36 and regions which ends with cells ieta = 35. Thus throughout this chapter all combinations of rapidity intervals ieta $\in [x,y]$, where $x \in [26,37]$ and $y \in [35,37]$, $x < y$, are examined. As already mentioned all these combinations are further separated for north and south side of the calorimeter.

There is also possibility that there is a difference between energy deposited in electromagnetic and fine hadronic parts of calorimeter. An example of this is displayed in Fig. 5.5 - Fig. 5.6. Plots show only the south side and rapidity intervals which end at the end of calorimeter (ieta = 37). The other intervals are not shown because their distribution is similar to these. From these plots we can conclude:

1. There is no big difference between activity in electromagnetic and fine hadronic parts.

2. As mentioned above, there is still non-negligible number of events in jet sample with very low activity in any rapidity interval.

3. The separation of noise and inclusive samples is smaller than in the case of EM+FH sum in respective regions (compare to Fig. 5.7). In case of EM or FH sums, the two distributions are 'closer' to each other, which means that overlap of the two graphs is larger.

A good separation of inclusive and noise samples is the basic idea to define the gap in the manner described above. The principle is that the definition should be set so that the number of inclusive events falling below the energy limit is as small as possible and vice versa with the noise events. When the separation between the two samples is the highest possible, the contamination between the samples mutually is the lowest possible. Therefore only the whole sum of EM and FH cells is assumed in further analysis.

The energy sum plots are presented in Fig. 5.7 - Fig. 5.12. All investigated regions for south and north sides of the calorimeter are shown.

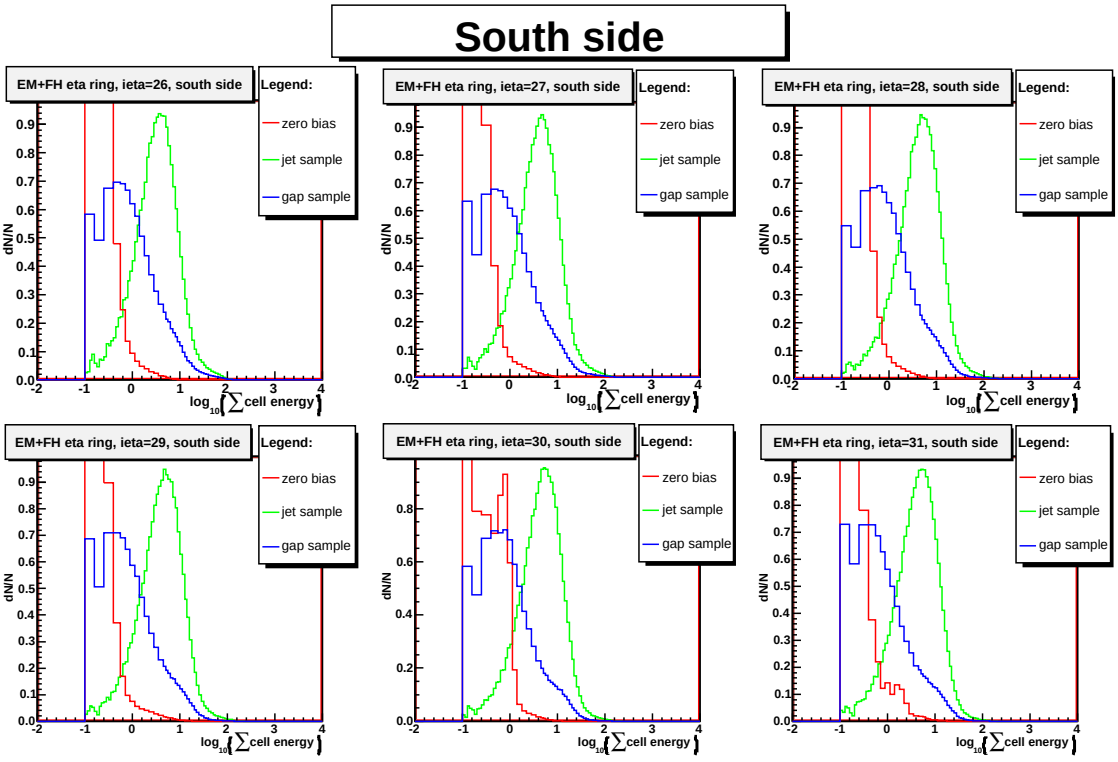

Figure 5.3: Sum of calorimeter cells with a given ieta. Events with LM south turned off.

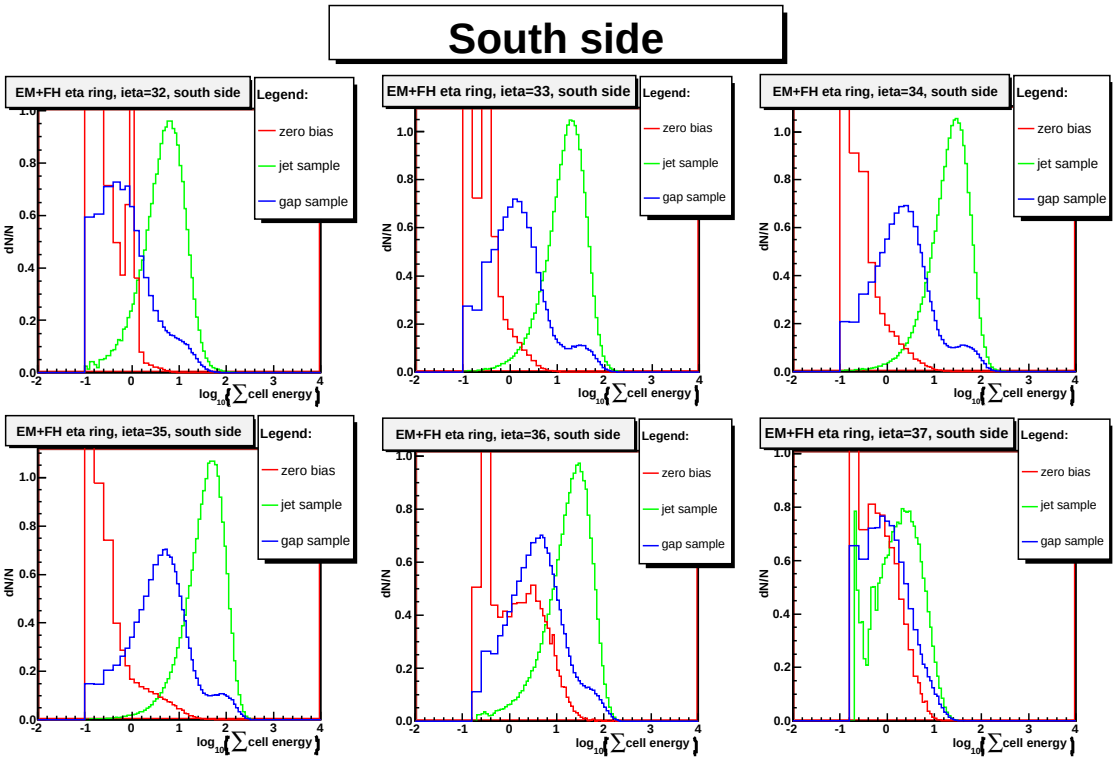

Figure 5.4: Sum of calorimeter cells with a given ieta. Events with LM south off.

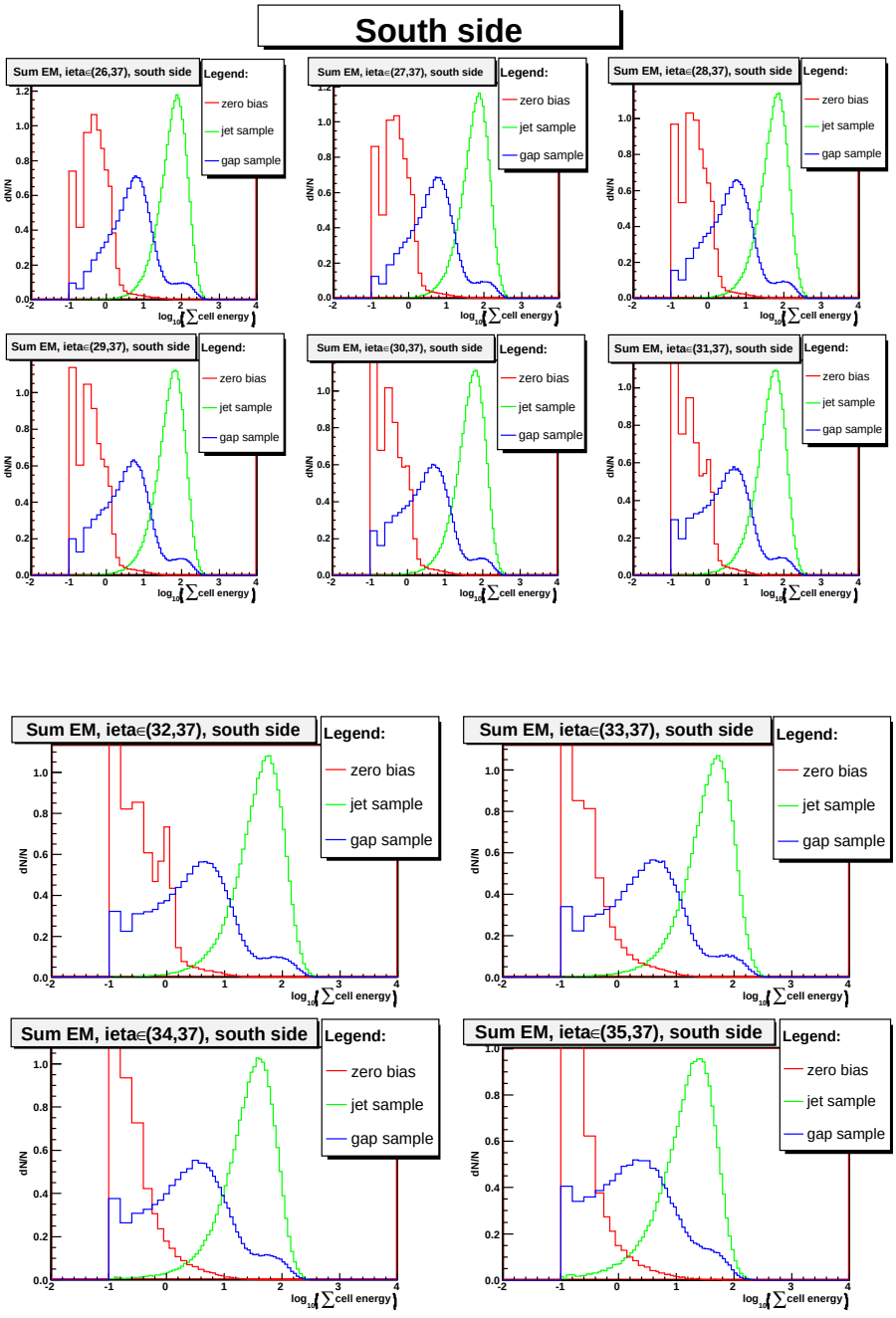

Figure 5.5: Sum of cell energies for various ieta intervals for cells in electromagnetic part of calorimeter. Events with lms off.

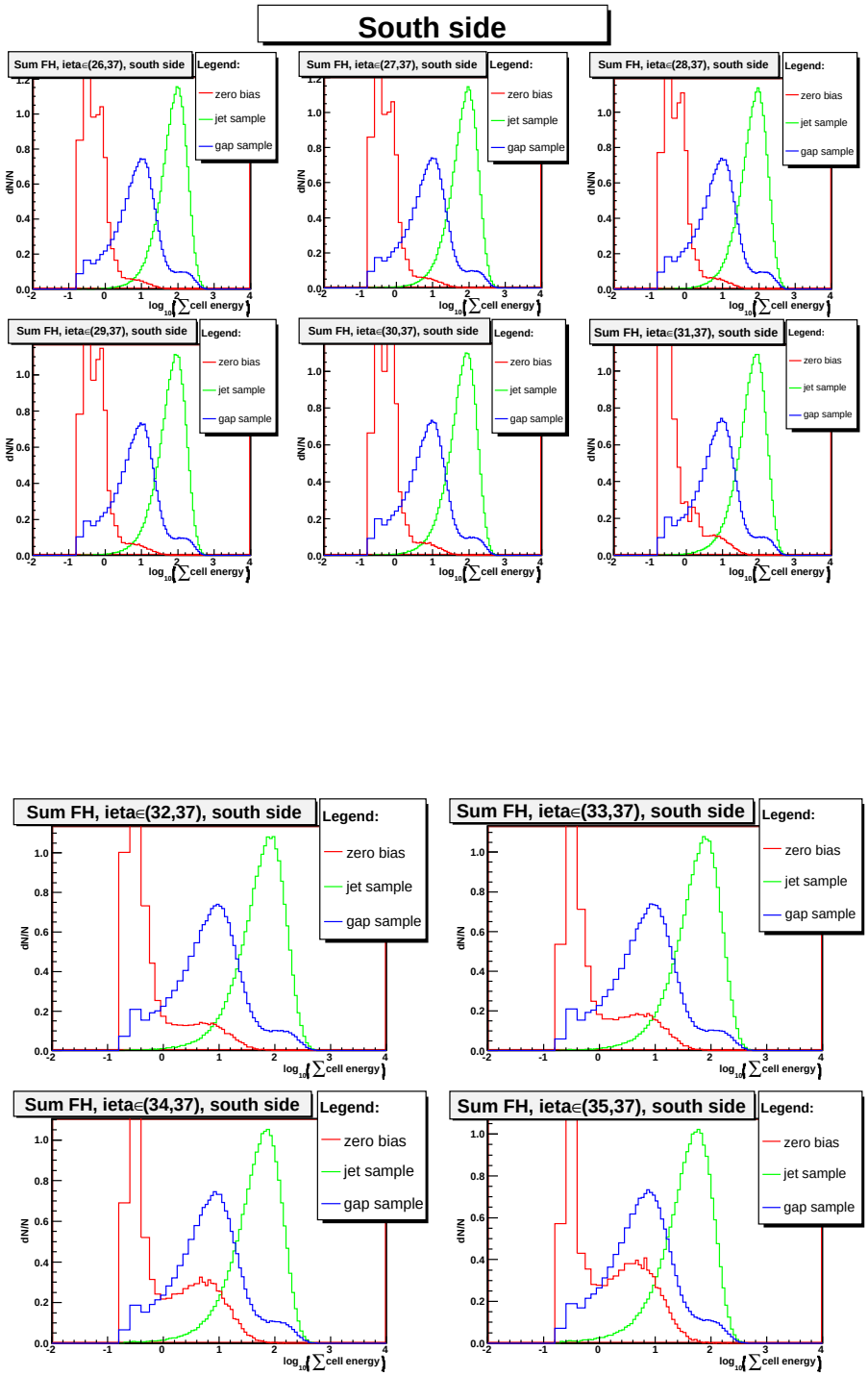

Figure 5.6: Sum of cell energies for various ieta intervals for cells in fine hadronic part of calorimeter. Events with lms off.

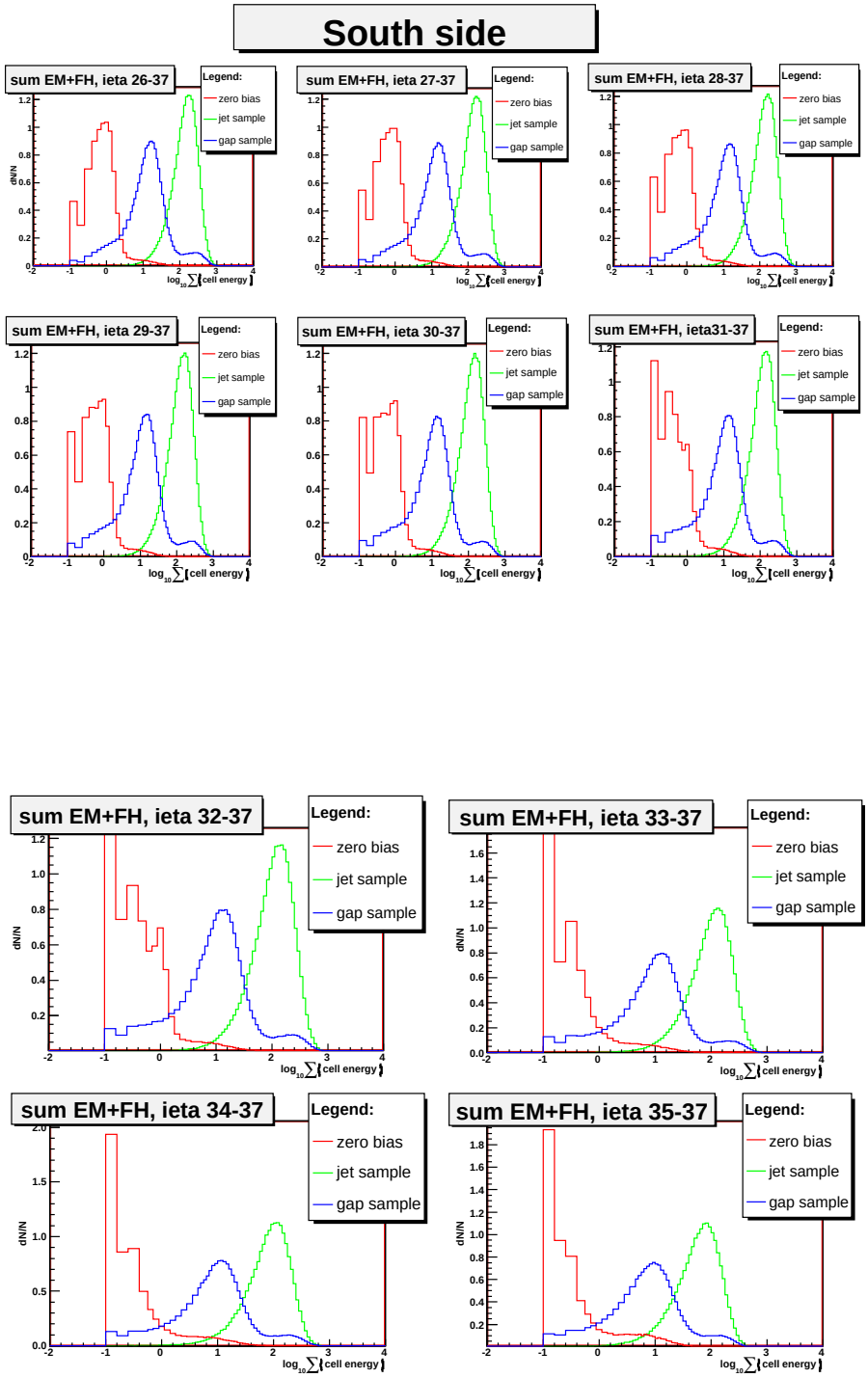

Figure 5.7: Sum of cell energies for various ieta intervals for cells within whole calorimeter except the coarse hadronic part. Events with LM south turned off.

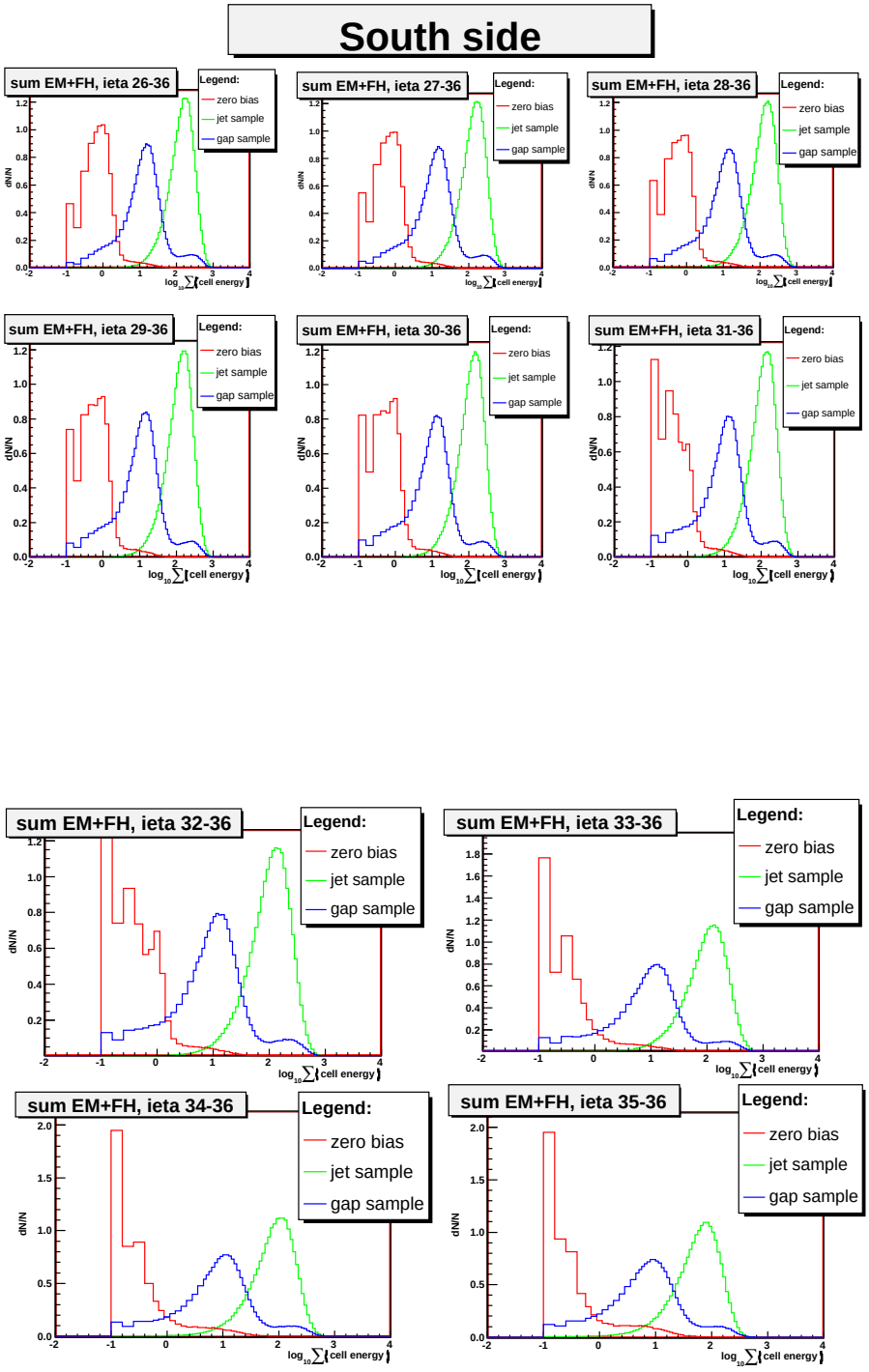

Figure 5.8: Sum of cell energies for various ieta intervals for cells within whole calorimeter except the coarse hadronic part. Events with LM south turned off.

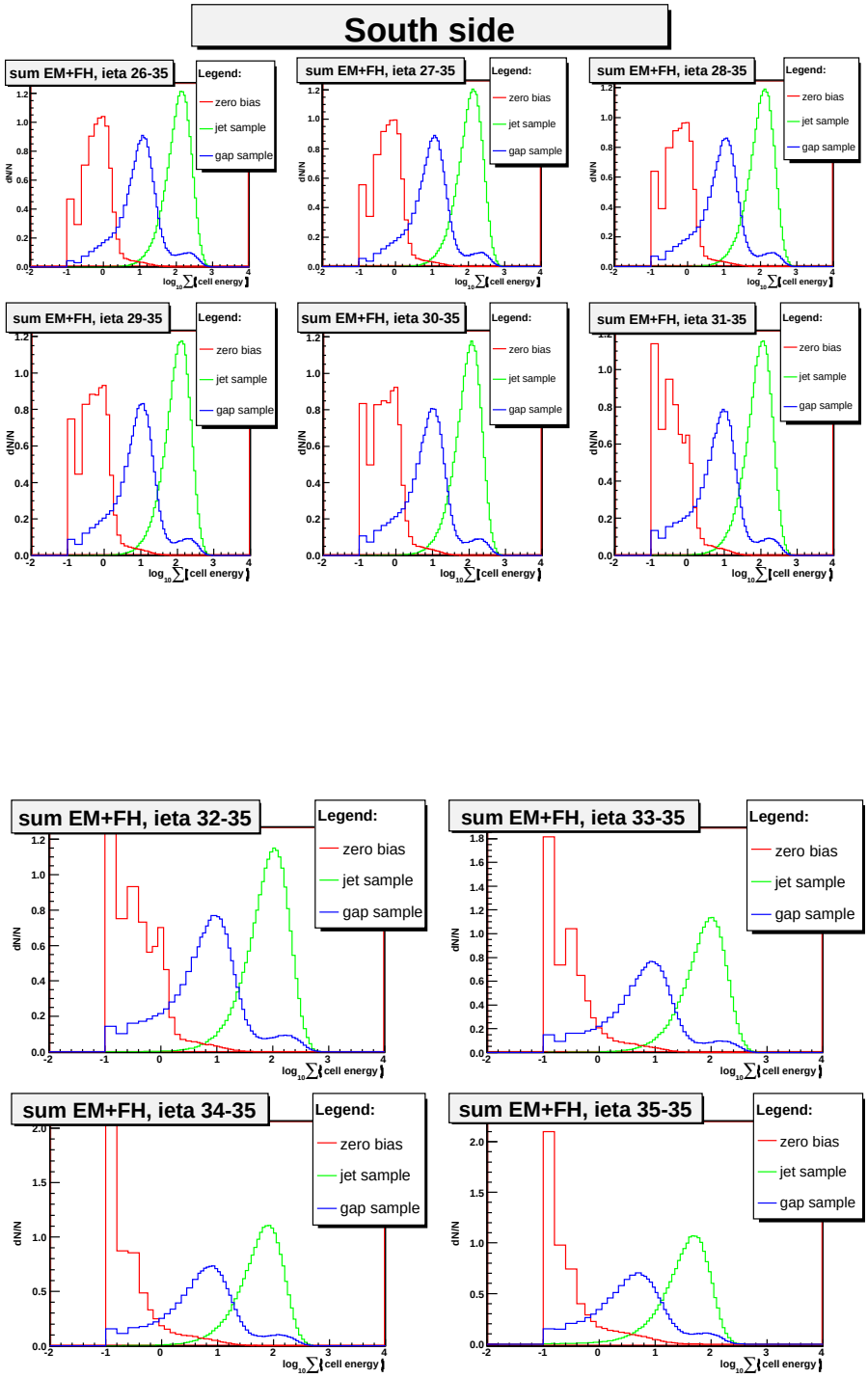

Figure 5.9: Sum of cell energies for various ieta intervals for cells within whole calorimeter except the coarse hadronic part. Events with LM south turned off.

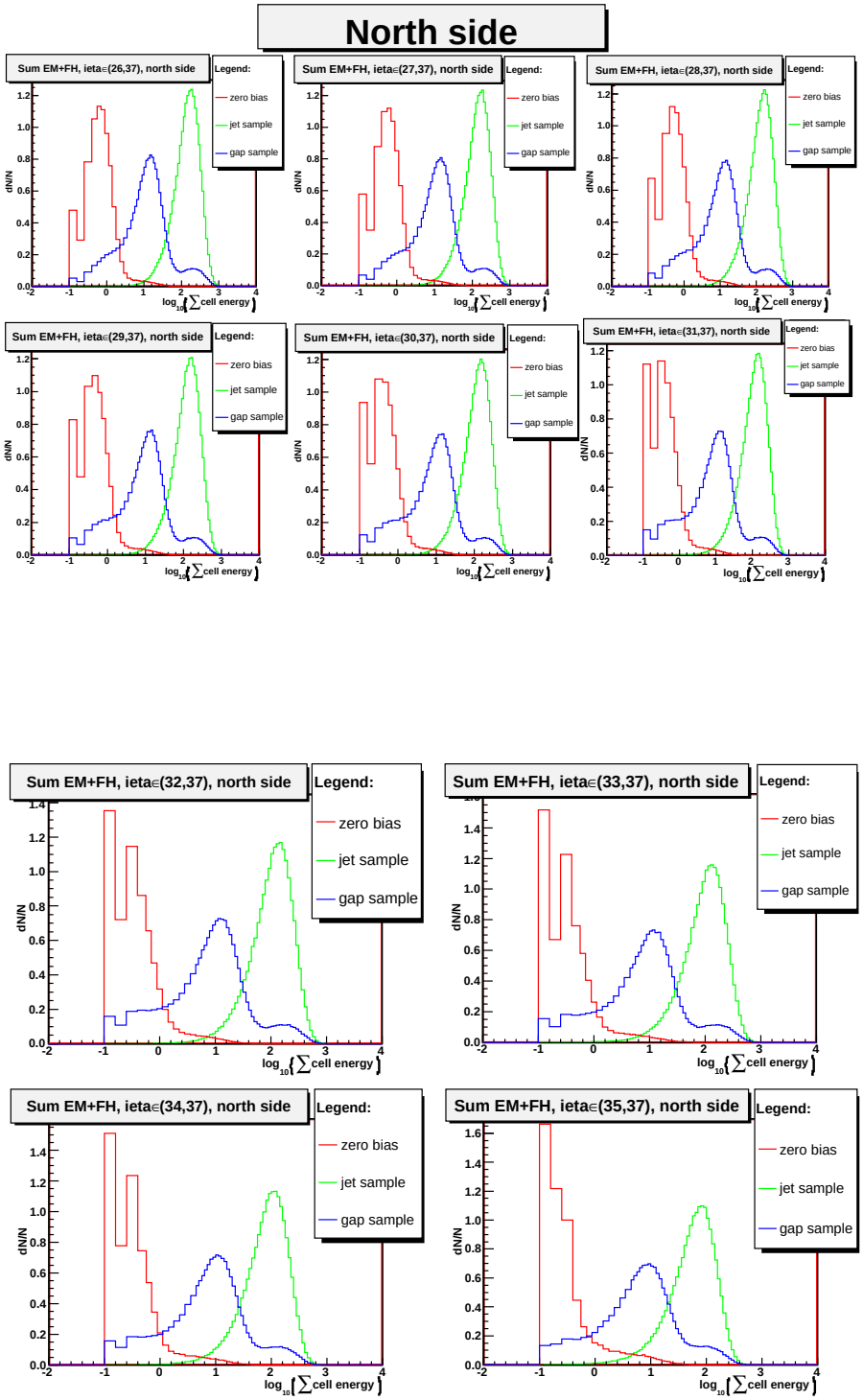

Figure 5.10: Sum of cell energies for various ieta intervals for cells within whole calorimeter except the coarse hadronic part. Events with LM north turned off.

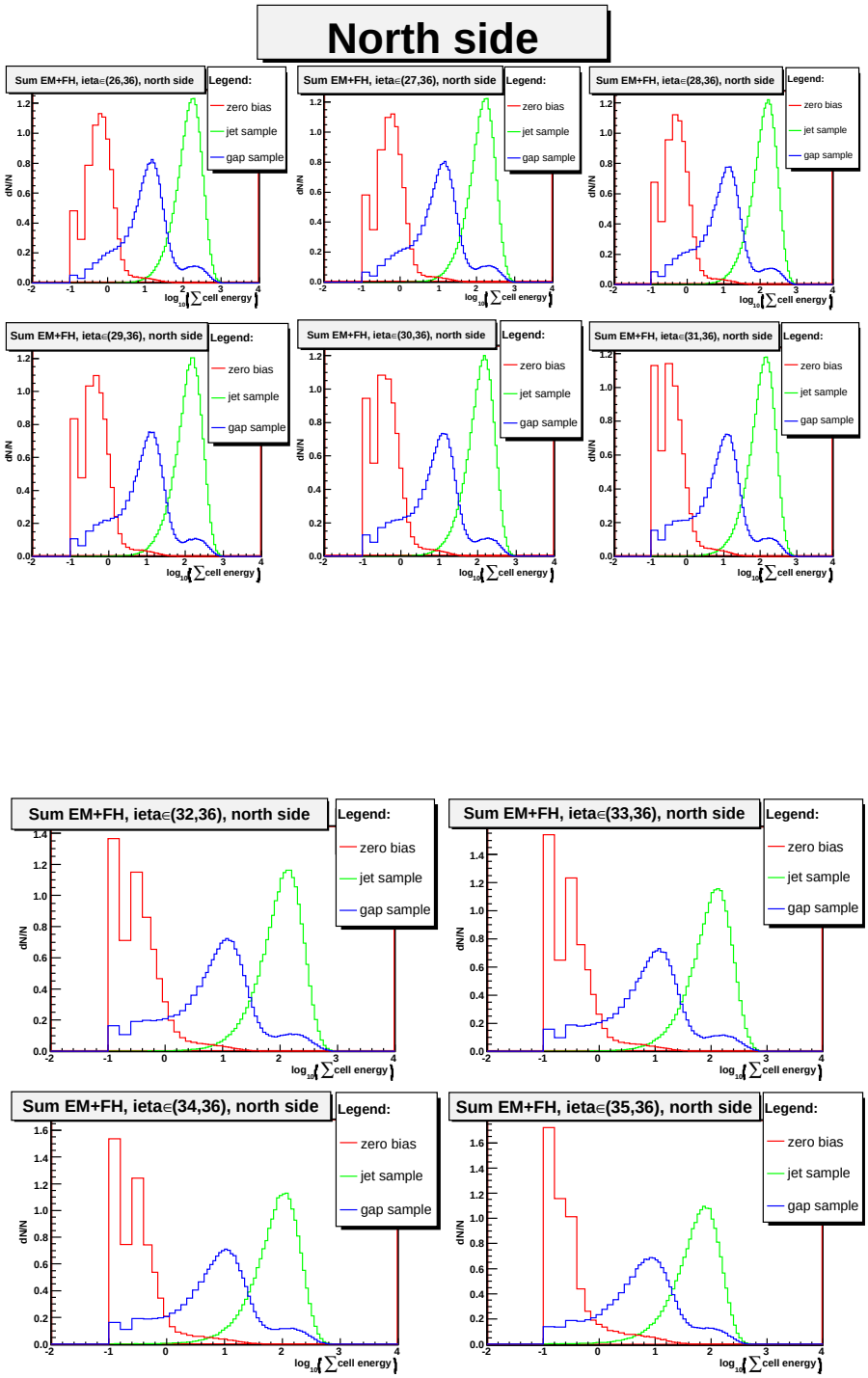

Figure 5.11: Sum of cell energies for various ieta intervals for cells within whole calorimeter except the coarse hadronic part. Events with LM north turned off.

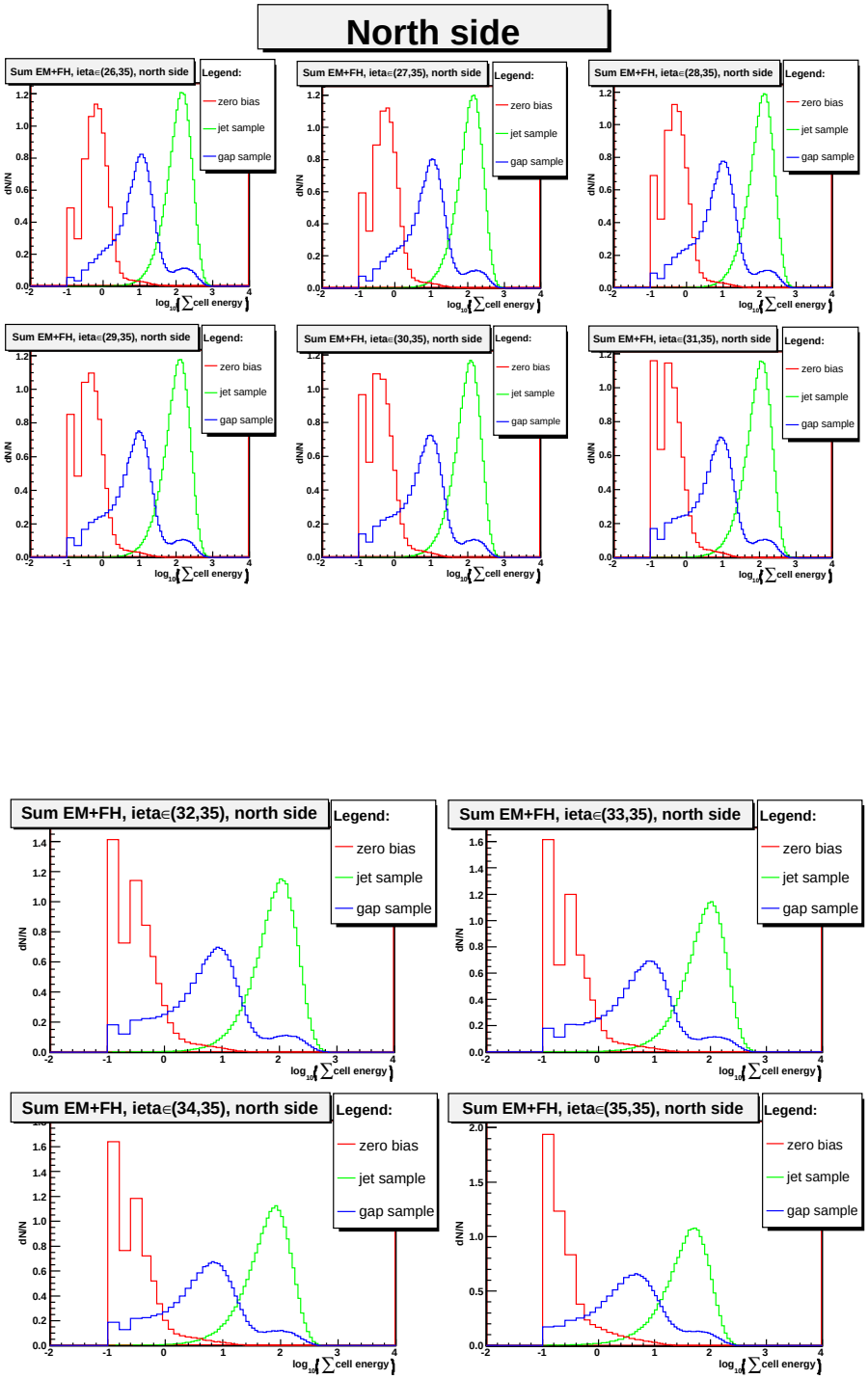

Figure 5.12: Sum of cell energies for various ieta intervals for cells within whole calorimeter except the coarse hadronic part. Events with LM north turned off.

To find the best region and the best cut, we must examine all plots and all possible cuts in each of them, and look for the lowest mutual contamination between the noise and the inclusive samples. The procedure is as follows:

1. One rapidity interval is picked and the lowest cut is chosen.
2. The ratio of noise events that are *above* the cut to the total number of noise events is measured for this plot. Similarly, the ratio of number of inclusive events which are *below* the cut to the total number of inclusive events is computed.
3. This procedure is repeated for all possible cuts (with offset 0.05) and all plots.
4. The resulted ratios are displayed in one graph. Points corresponding to one sample and one rapidity region are connected with a line.

Figures 5.13 - 5.18 show the described ratios for all involved regions and energy cuts. One color corresponds to one rapidity interval.

The differences of the distributions in the individual rapidity intervals are small and it is difficult to determine the best combination of region and the energy cut. Generally, both ratios of the noise and the inclusive samples for one rapidity region should be as small as possible. To compare the particular regions among each other, it is useful to combine together results of noise and inclusive samples. This is done using an auxiliary function of the two plots.

First, the noise sample plots are transformed as $p_1 = 100 - p$, where p is the original value of the noise ratios. After the transformation, we look for such a combination of rapidity interval and the energy limit, for which the new noise sample ratios are the highest possible while the inclusive sample ratios are the smallest. So we think of the noise ratios as a *signal (S)* sample, and of the inclusive ratios as a *background (B)* sample and we use the best significance function for a comparison (F_2). One more function is used to compare the results. Using this notation, we examine two functions:

$$F_1 = S - B \tag{5.1}$$

$$F_2 = \frac{S}{\sqrt{S+B}} \tag{5.2}$$

Plots of these functions are shown in Fig. 5.19-5.30.

First function is a simple subtraction for which a maximum value can be less or equal to 100. The second one is an expression for the best statistical significance of signal to background ratio, where the maximum value is 10.

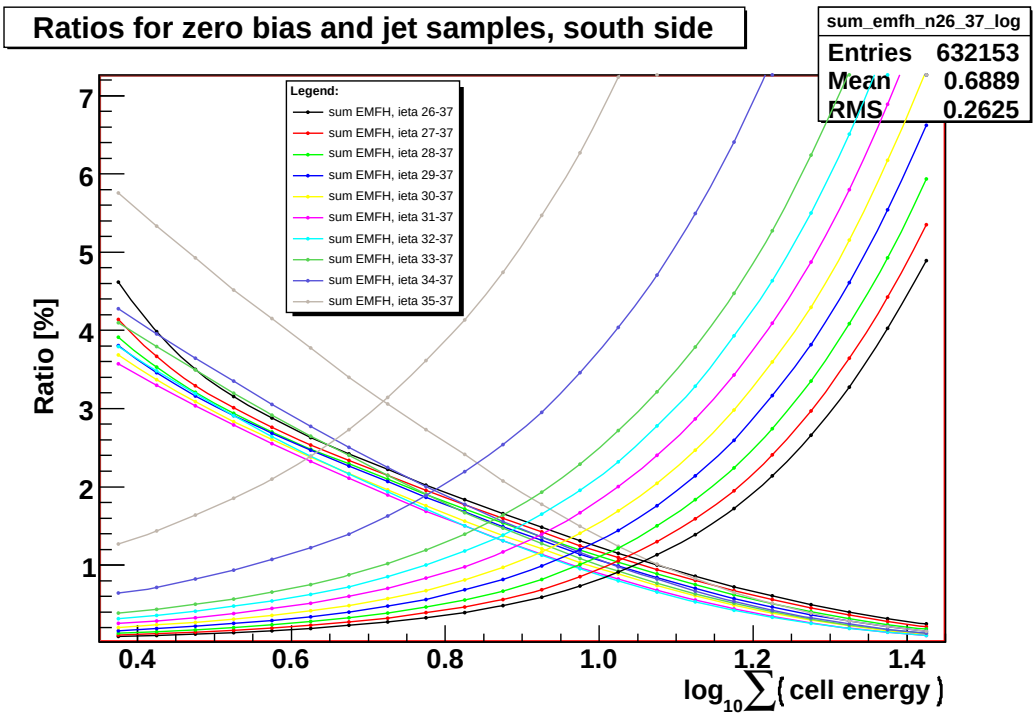

Figure 5.13: The percentage of number of events under/above a cut (which is represented by *x*-axis) to the total number of events for inclusive (on the right side) and zero bias (on the left side) sample. The ratio is shown under a cut for inclusive sample and above the cut for the noise sample. The plots show the energy sum of calorimeter cells in ieta intervals up to 37 with LM gap on the south side.

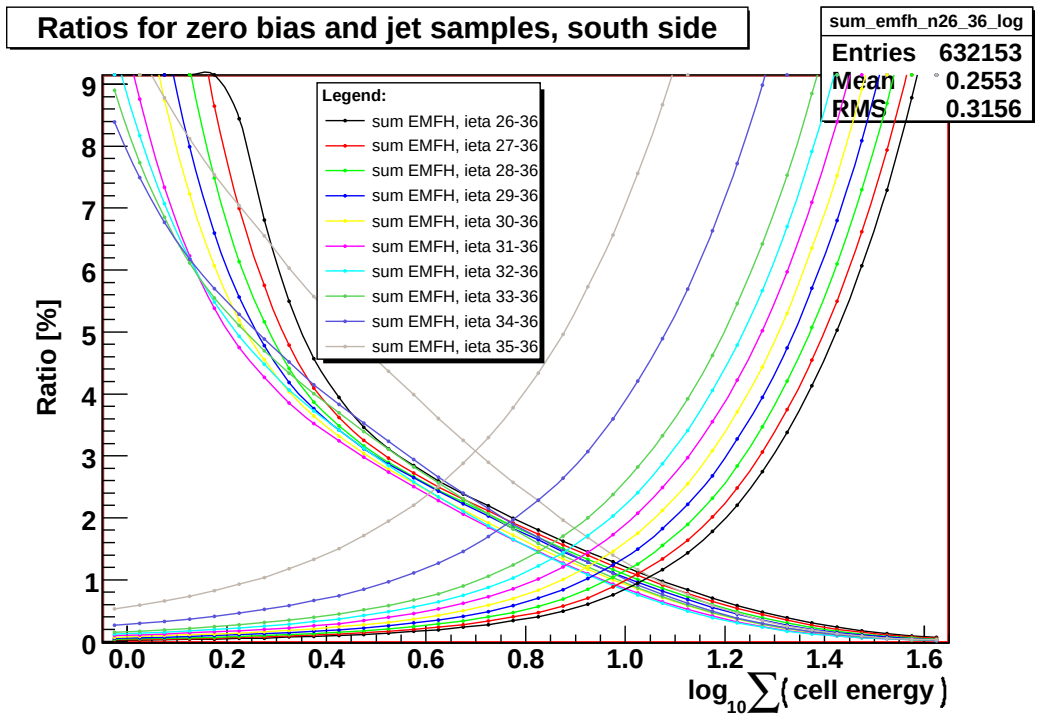

Figure 5.14: The percentage of number of events under/above a cut (which is represented by *x*-axis) to the total number of events for inclusive (on the right side) and zero bias (on the left side) sample. The ratio is shown under a cut for inclusive sample and above the cut for zero bias sample. The plots show the energy sum of calorimeter cells in ieta intervals up to 36 with LM gap on the south side.

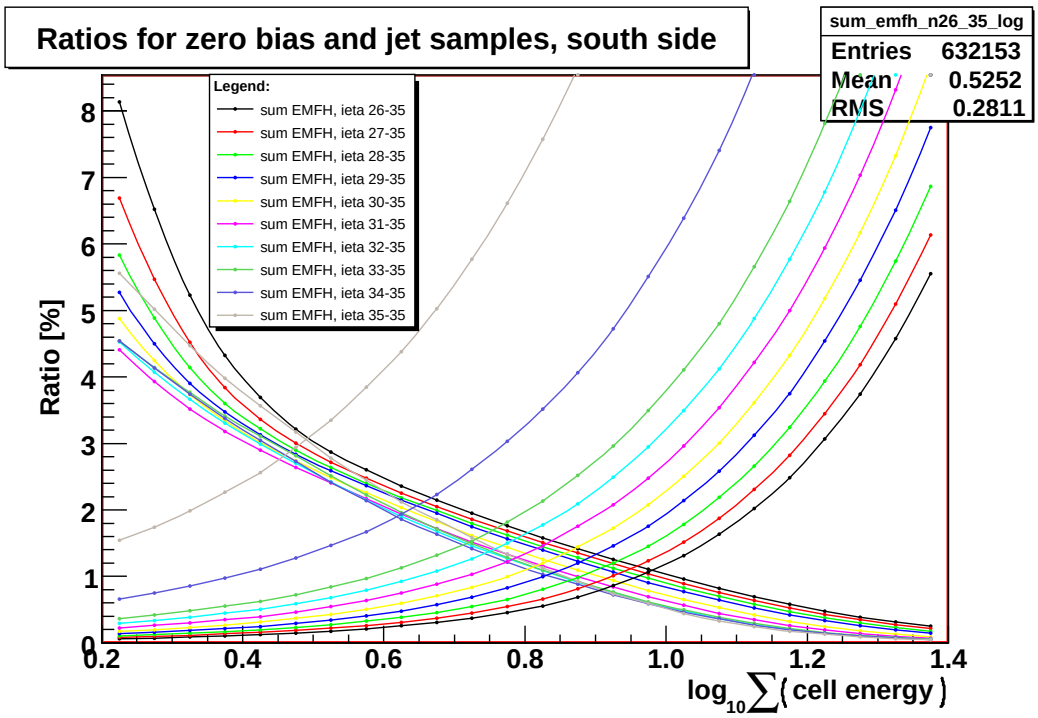

Figure 5.15: The percentage of number of events under/above a cut (which is represented by *x*-axis) to the total number of events for inclusive (on the right side) and zero bias (on the left side) sample. The ratio is shown under a cut for inclusive sample and above the cut for zero bias sample. The plots show the energy sum of calorimeter cells in ieta intervals up to 35 with LM gap on the south side.

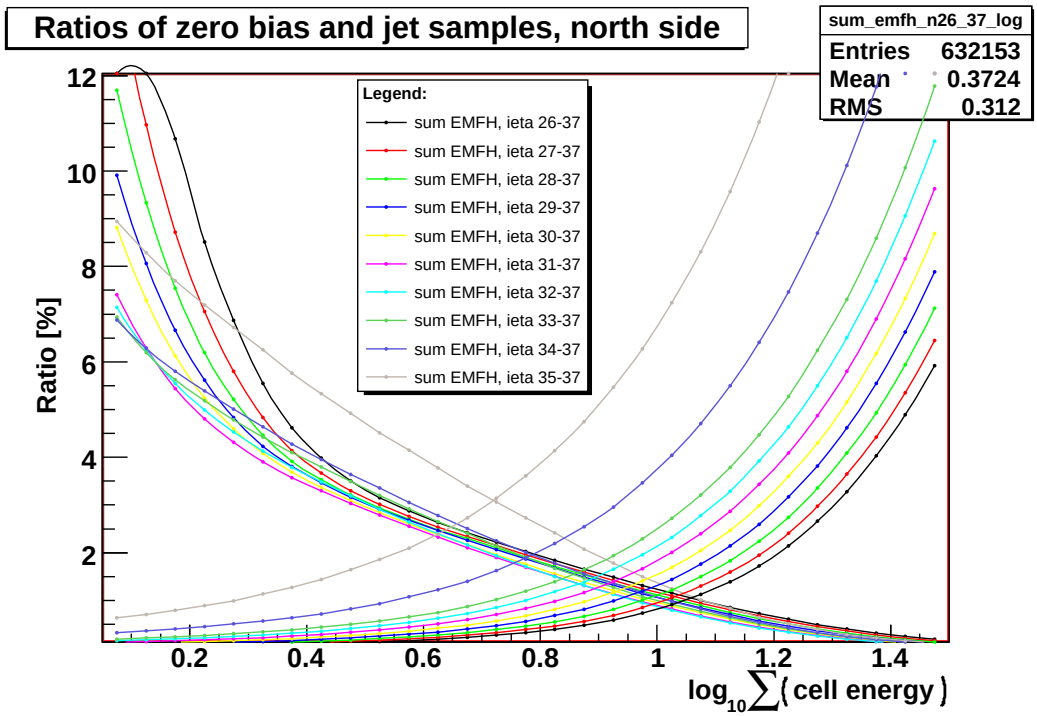

Figure 5.16: The percentage of number of events under/above a cut (which is represented by *x*-axis) to the total number of events for inclusive (on the right side) and zero bias (on the left side) sample. The ratio is shown under a cut for inclusive sample and above the cut for zero bias sample. The plots show the energy sum of calorimeter cells in ieta intervals up to 37 with LM gap on the north side.

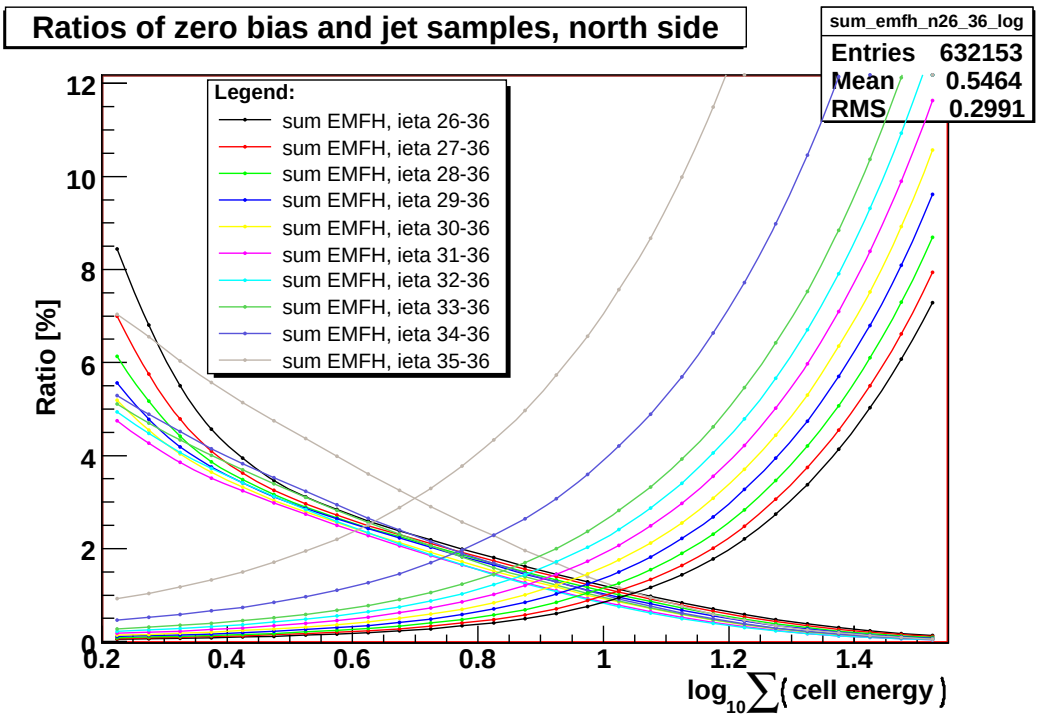

Figure 5.17: The percentage of number of events under/above a cut (which is represented by *x*-axis) to the total number of events for inclusive (on the right side) and zero bias (on the left side) sample. The ratio is shown under a cut for inclusive sample and above the cut for zero bias sample. The plots show the energy sum of calorimeter cells in ieta intervals up to 36 with LM gap on the north side.

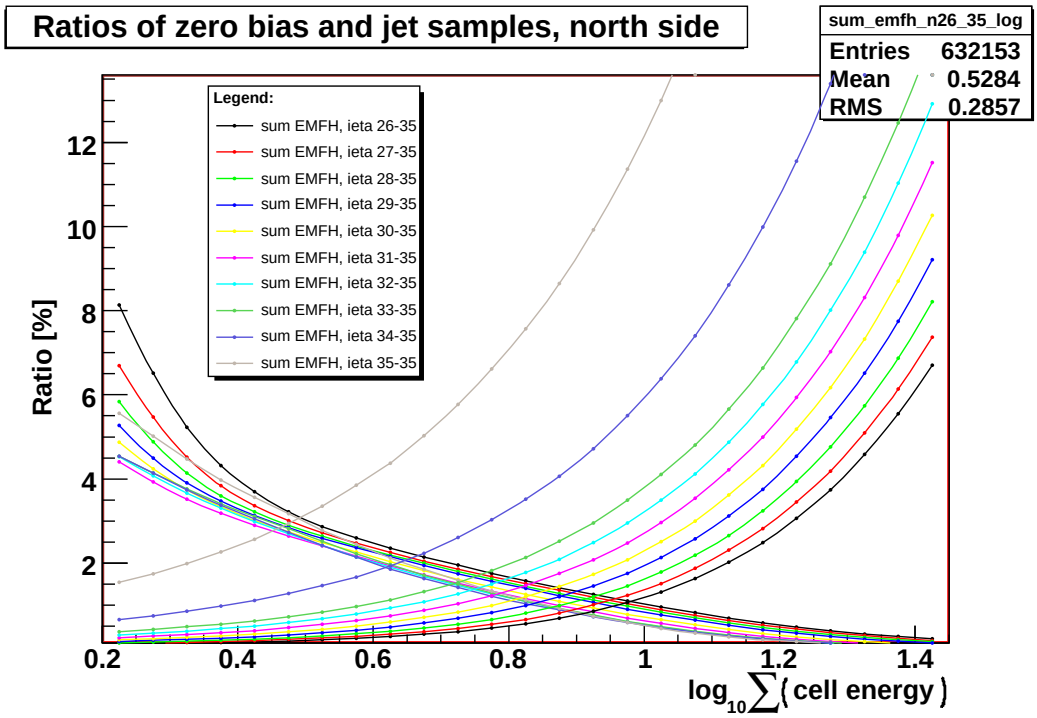

Figure 5.18: The percentage of number of events under/above a cut (which is represented by *x*-axis) to the total number of events for inclusive (on the right side) and zero bias (on the left side) sample. The ratio is shown under a cut for inclusive sample and above the cut for zero bias sample. The plots show the energy sum of calorimeter cells in ieta intervals up to 35 with LM gap on the north side.

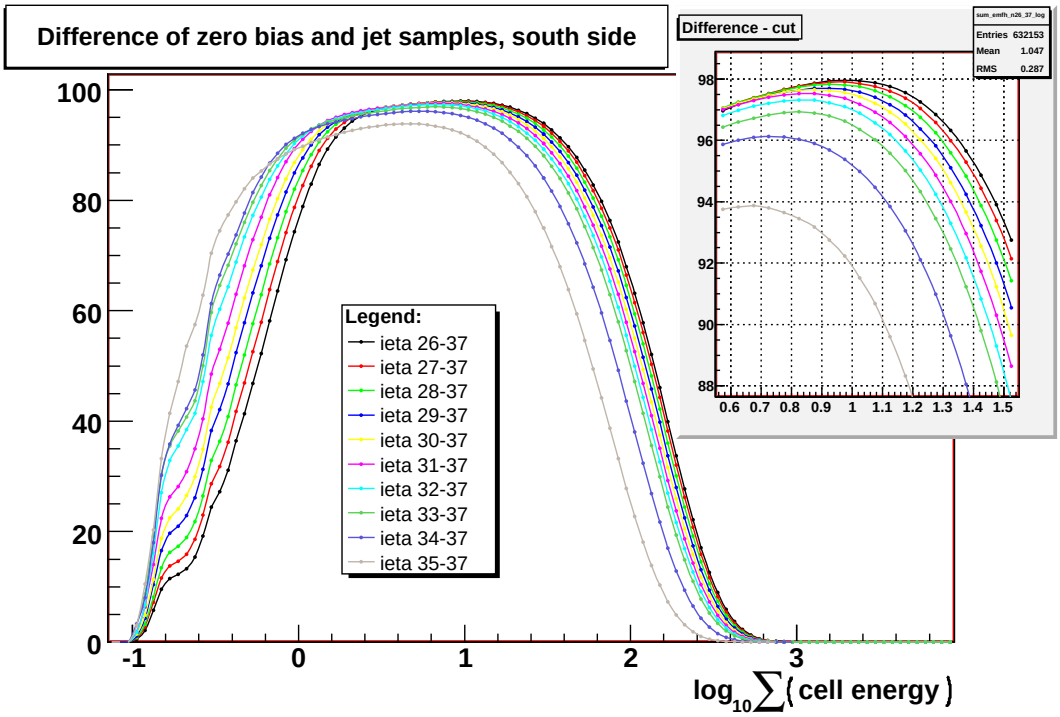

Figure 5.19: F_1 distribution for cell sums within ieta intervals up to 37, south side.

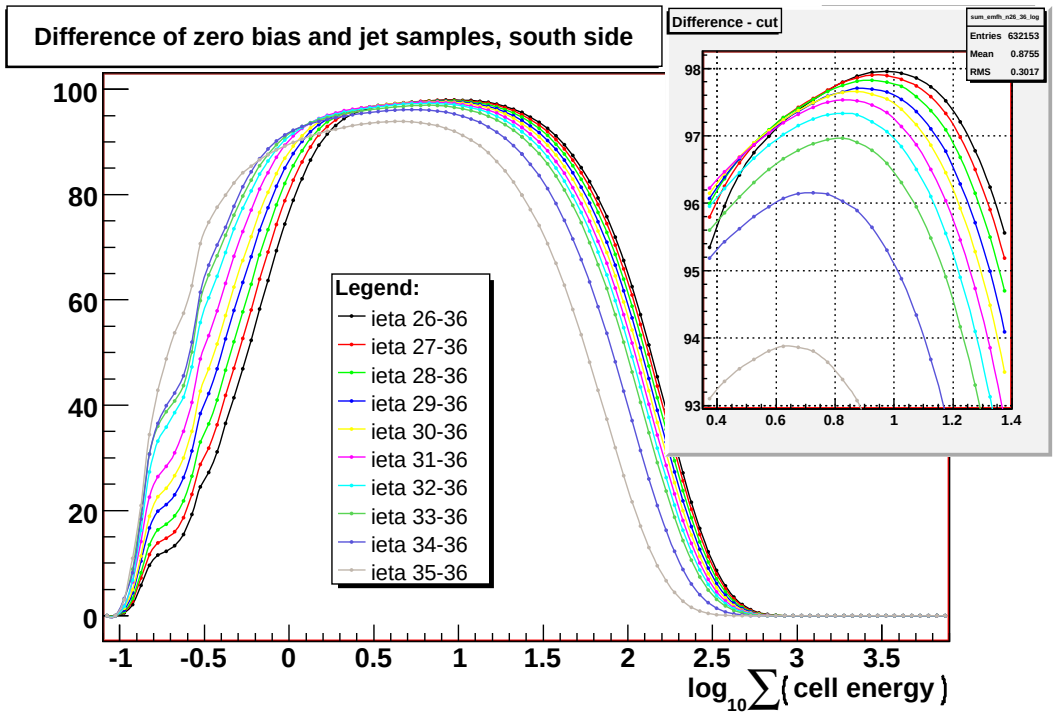

Figure 5.20: F_1 distribution for cell sums within ieta intervals up to 36, south side.

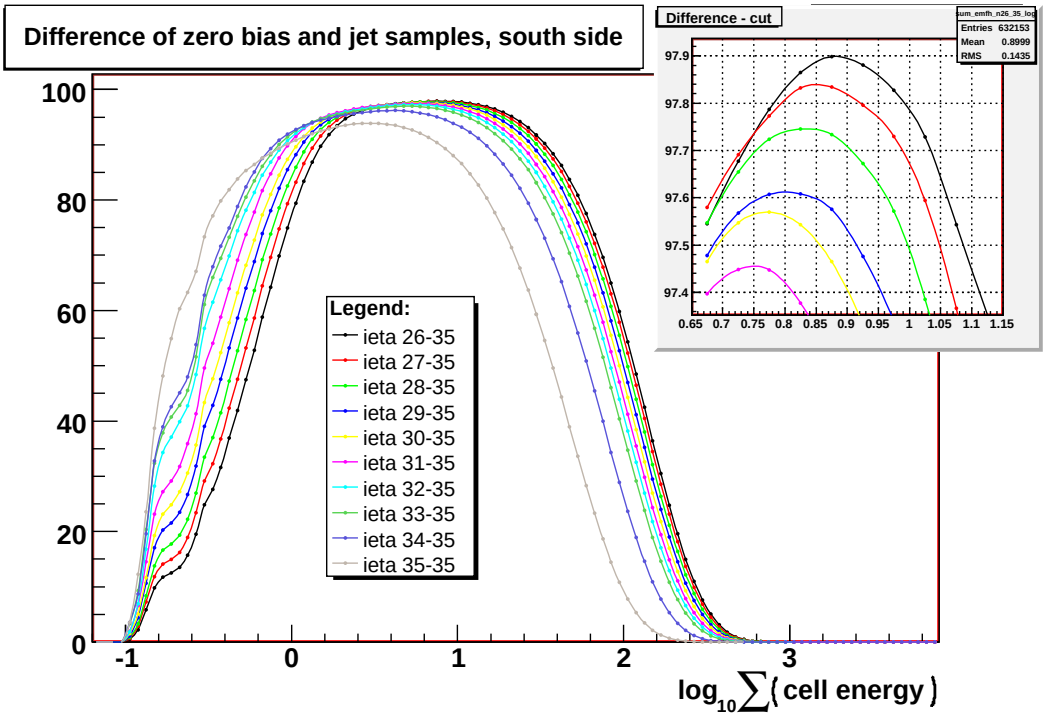

Figure 5.21: F_1 distribution for cell sums within ieta intervals up to 35 south side.

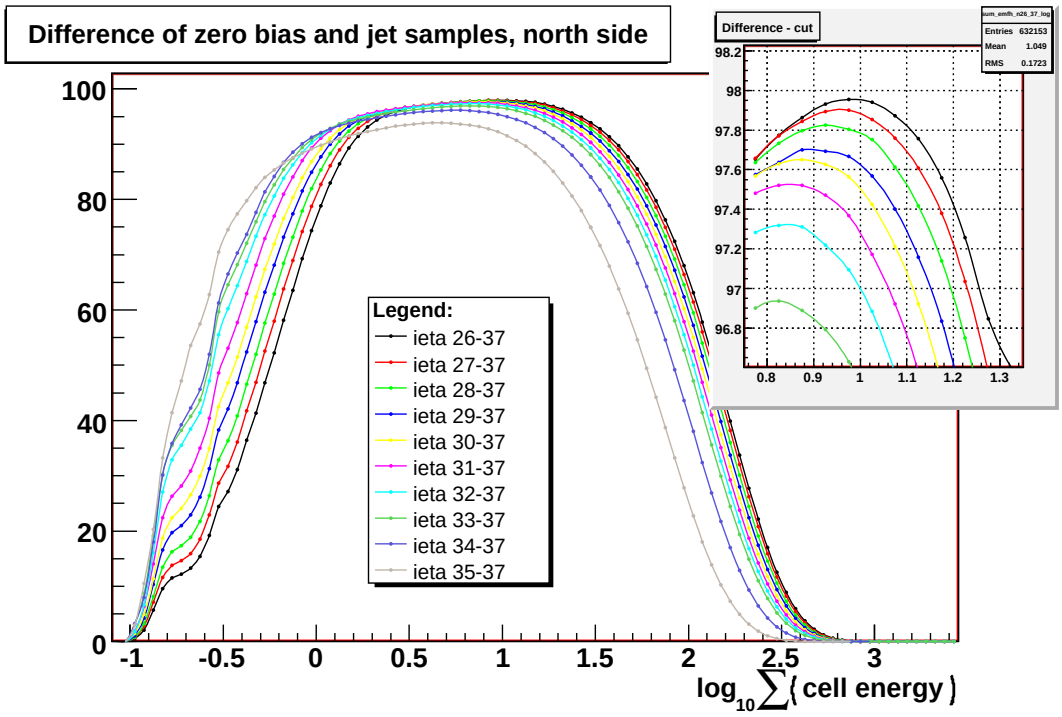

Figure 5.22: F_1 distribution for cell sums within ieta intervals up to 37, north side.

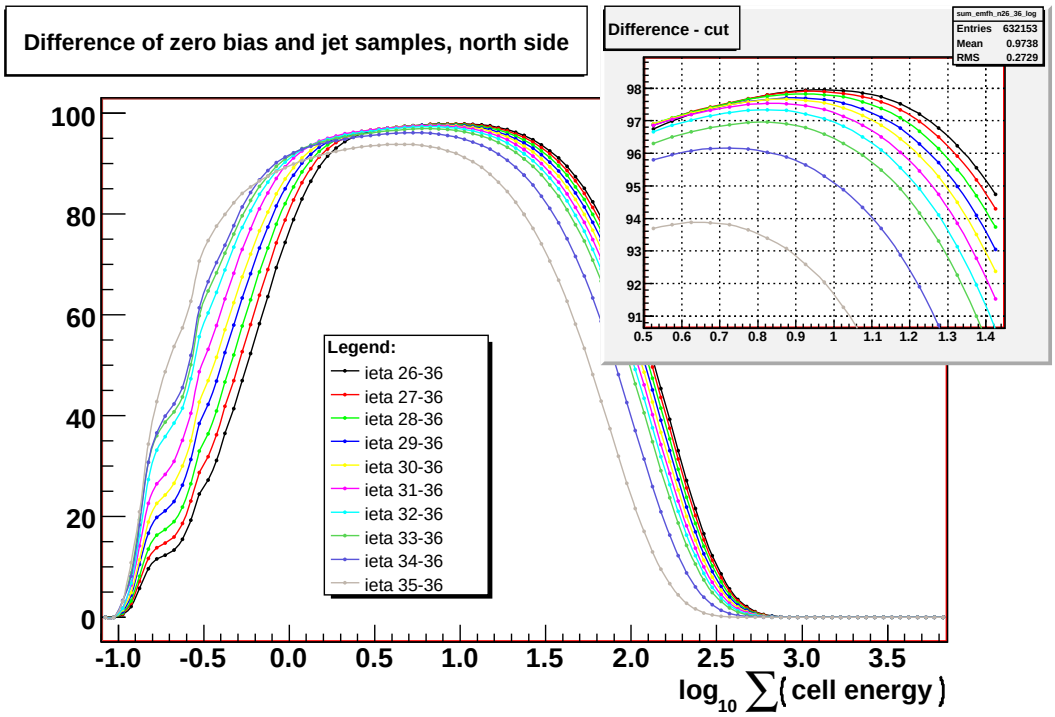

Figure 5.23: F_1 distribution for cell sums within ieta intervals up to 36, north side.

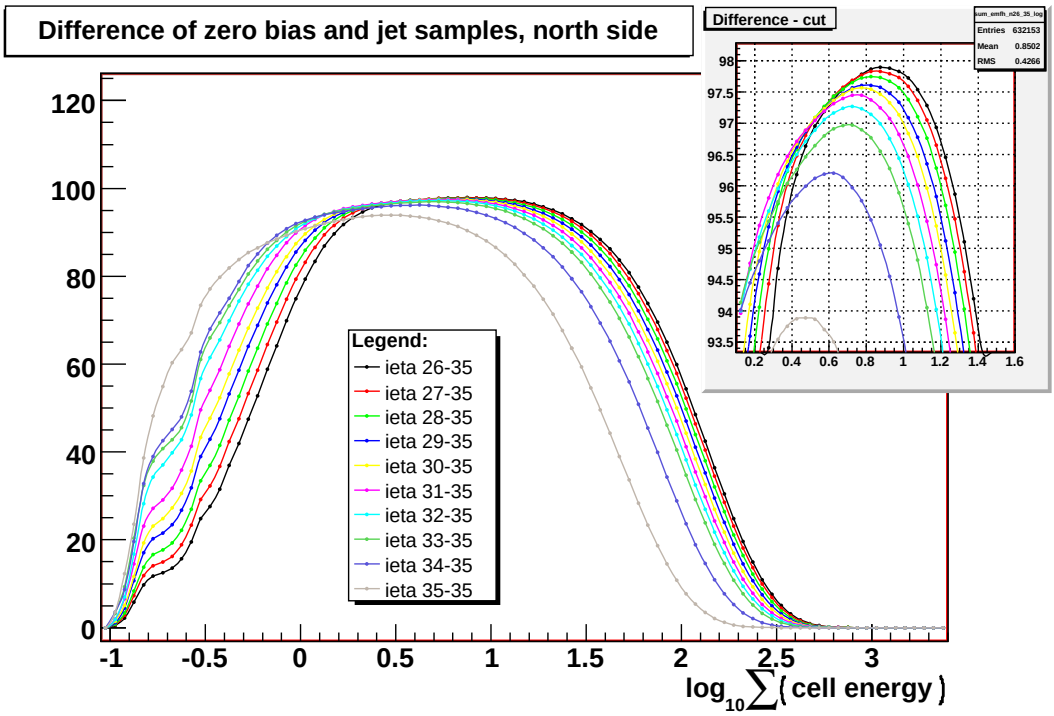

Figure 5.24: F_1 distribution for cell sums within ieta intervals up to 35, north side.

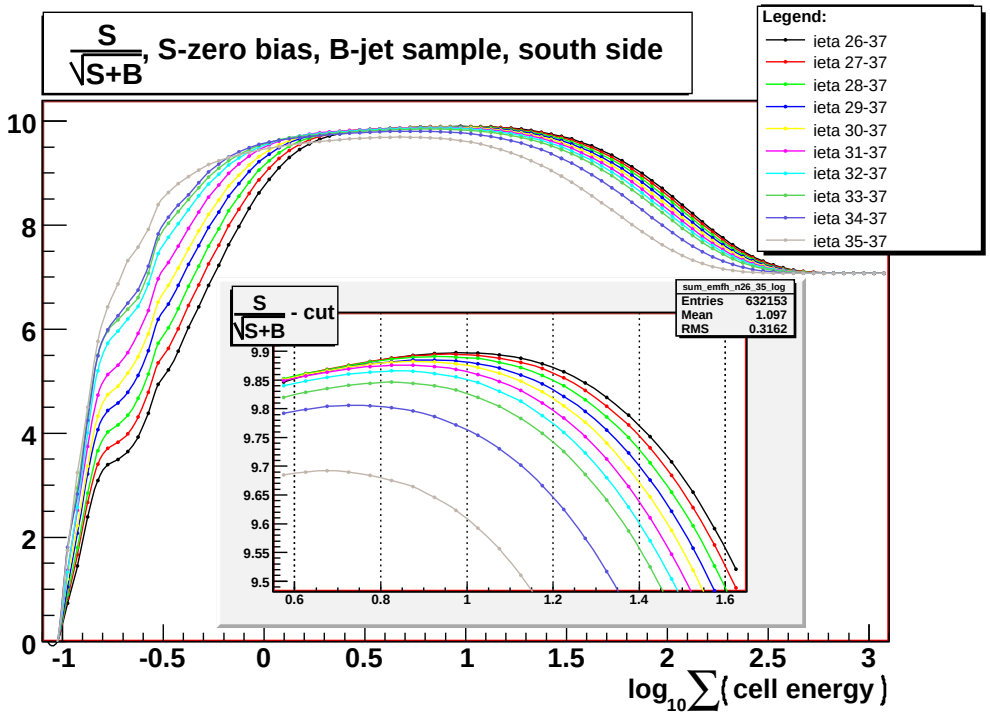

Figure 5.25: F_2 distribution for cell sums within ieta intervals up to 37, south side.

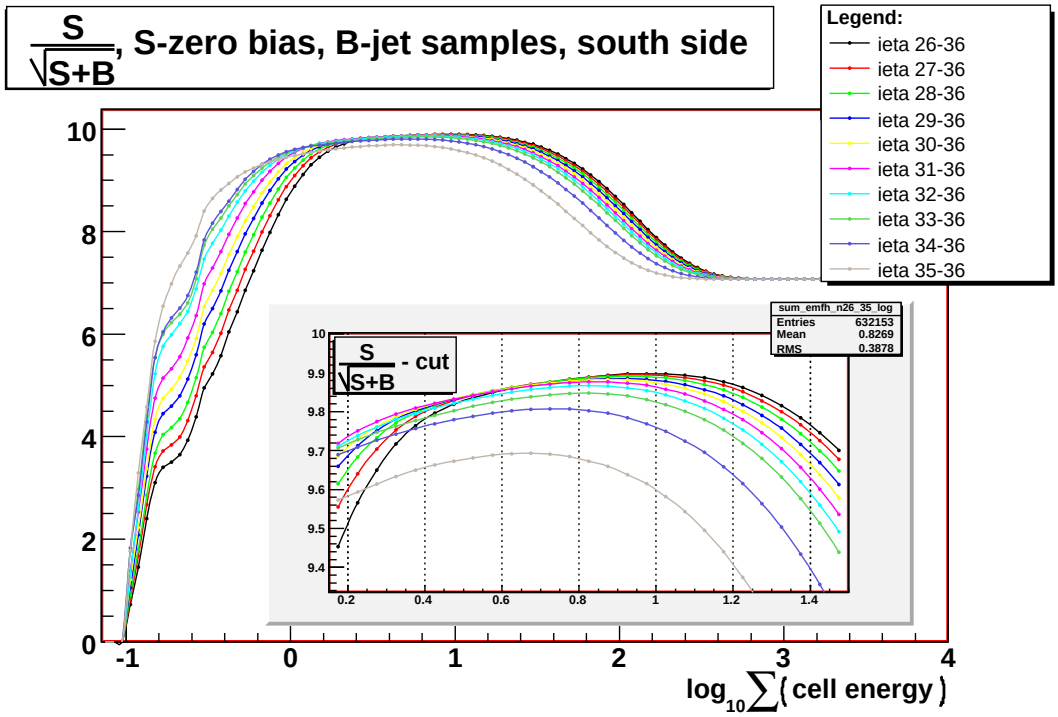

Figure 5.26: F_2 distribution for cell sums within ieta intervals up to 36, south side.

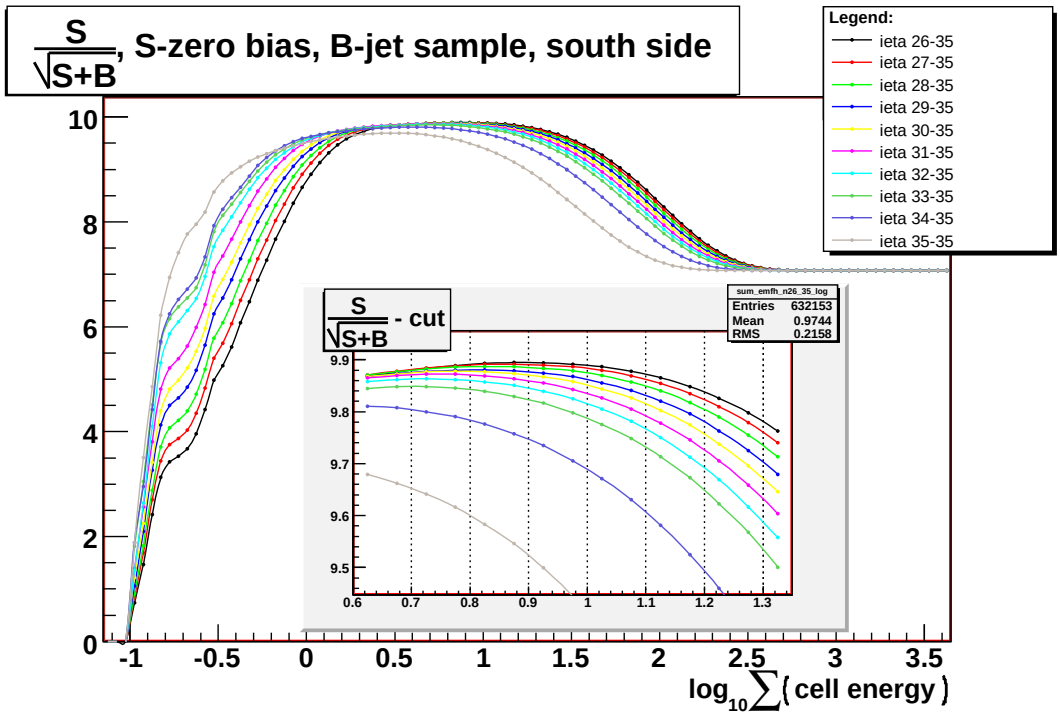

Figure 5.27: F_2 distribution for cell sums within ieta intervals up to 35, south side.

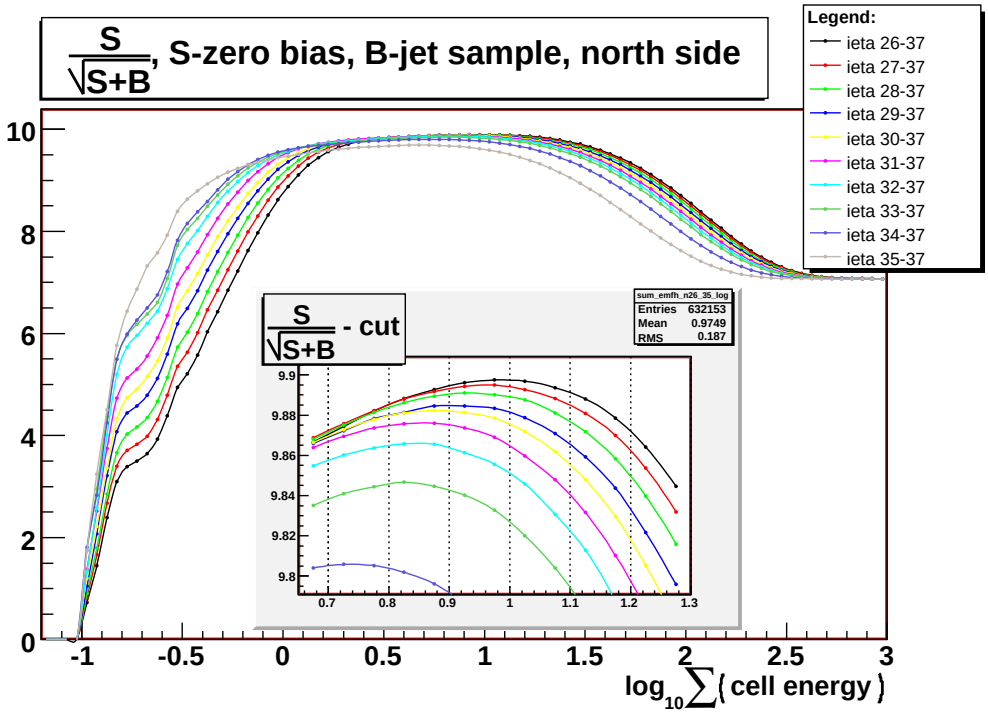

Figure 5.28: F_2 distribution for cell sums within ieta intervals up to 37, north side.

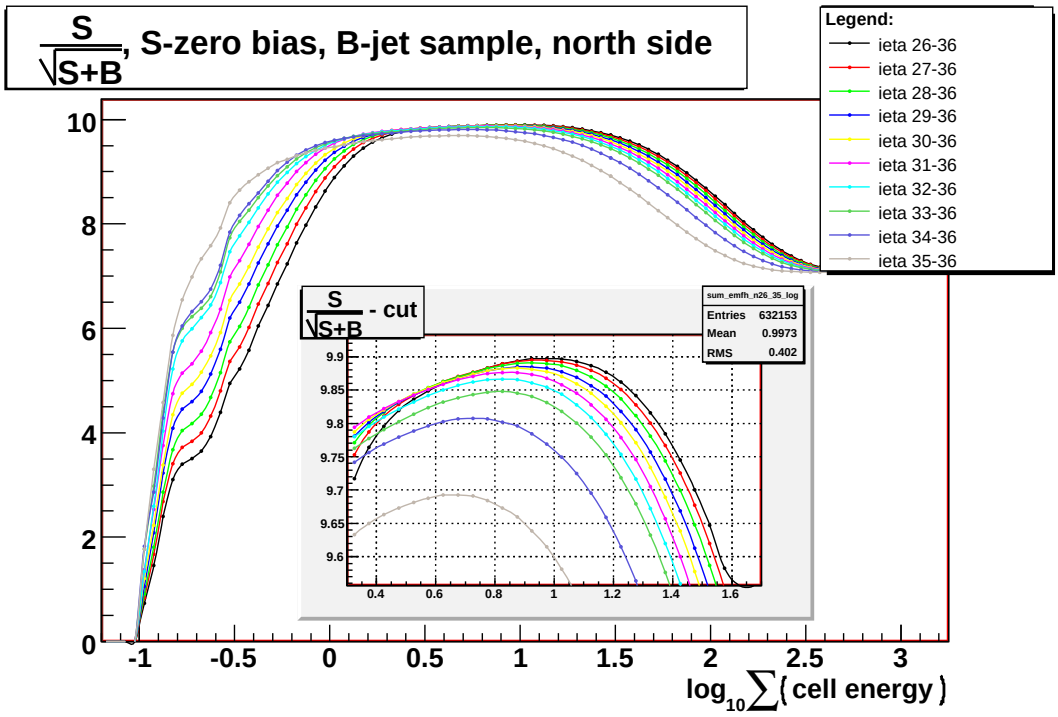

Figure 5.29: F_2 distribution for cell sums within ieta intervals up to 36, north side.

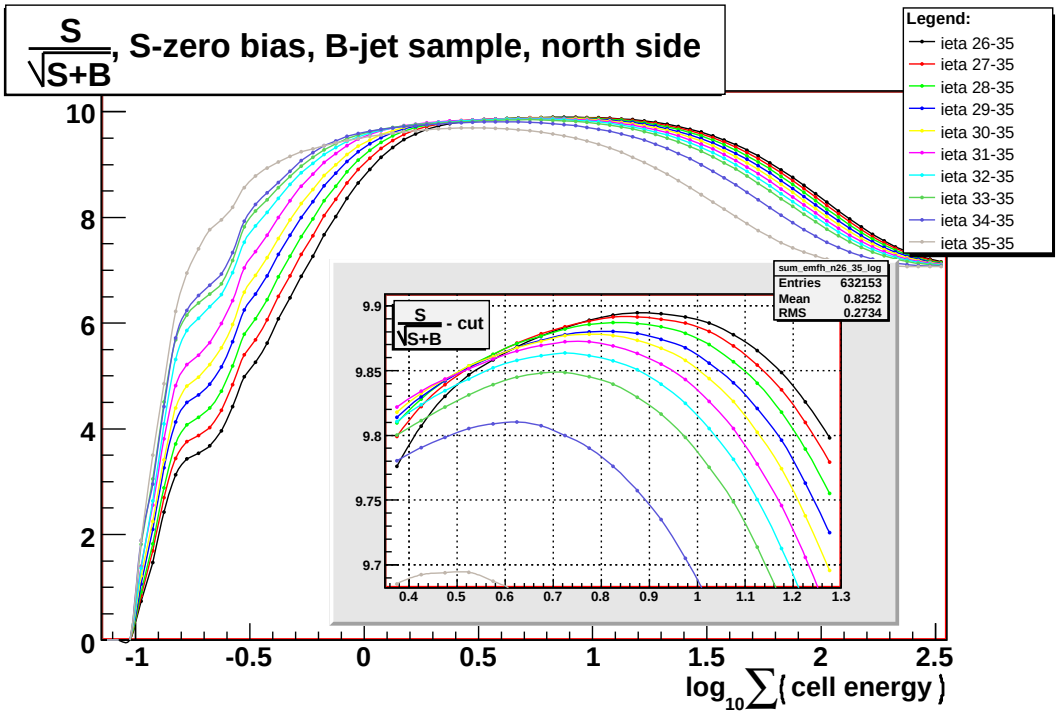

Figure 5.30: F_2 distribution for cell sums within ieta intervals up to 35, north side.

Both functions show the same results, which can be summarized as:

- The plots roughly show that the wider region is considered, the better are the results.
- At a rapidity of approximately 2.9 (ieta=29), graphs condense and differences between the regions are very small. Therefore wider rapidity intervals are no more examined.
- The problem with strange behaviour of cells with ieta = 36 and ieta = 37 disappeared in the energy sum over larger region; in fact the best results shows the region $|ieta| \in [26, 37]$.
- There is no difference between the distributions on north and south sides of the calorimeter.
- The maxima of both functions are at $log_{10}E_{sum} = 1$.

According to the observed properties of energy sums, the best rapidity gap definition can be summarized as:

1. LM and/or term fastZ is off
2. either lms or lmn is off
3. a sum of calorimeter cells in the respective direction satisfy:

$$\begin{aligned} \textstyle\sum_{cells} E_{cell} &< 10 \text{ GeV} && \text{, for cells with} \\ |ieta_{cell}| &> 25 && \\ E_{cell} &> 0.1 \text{ GeV} && \text{for EM cells} \\ &> 0.2 \text{ GeV} && \text{for FH cells} \end{aligned}$$

5.4 Alternative Definition

The definition given in the previous section has the lowest contamination between the samples, i.e. the lowest systematical errors, even though there still remain events coming from the non-diffractive interactions with energy sum below the cut and vice-versa. Increasing the energy limit decreases the number of diffractive events that are rejected, and increases the number of non-diffractive events that are accepted. Decreasing the limit works opposite.

In case of $\Delta\phi$ analysis, only the shape of the distribution is measured[4], so it is not necessary to deal with the systematical errors coming from the rejection of diffractive events. Instead, the purest possible diffractive sample is used to be compared to inclusive data. This pure sample is selected using an alternative gap definition, which rejects most of the inclusive contamination and accepts reasonable number of diffractive events.

In order to define a gap in the sense described above, the diffractive and inclusive samples are used. A new cut should be lower than the original one to get a cleaner sample, but this new definition can be done more or less arbitrarily. It is assumed that most of the diffractive events is included in the diffractive sample, while there are almost none in the inclusive one. The fraction of events that passed all selection criteria of the opposite sample (diffractive events assigned to inclusive sample and vice-versa) is assumed to be small and these events are neglected. With these assumptions, a rough estimation of the percentage of the events, which pass a limit, can thus be done using the same energy sum plots as before (Fig. 5.3 - 5.12). Similar ratios as in the previous case, but for diffractive and inclusive samples, are shown in Fig. 5.31-5.32.

Partial fractions of diffractive sample fall more slowly with decreasing energy sum than the inclusive sample. This is shown in Fig. 5.33 and Fig. 5.34, where the ratio of the two distributions is displayed. The ratio increases with lowering energy cut, which means that diffractive candidates are rejected less than the inclusive events[5]. It is also clear that the most increasing ratio is that of a rapidity interval $ieta \in [26,37]$.

Thus as the new gap definition, the same rapidity region $ieta \in [26,37]$ is used. The energy limit can be set arbitrarily, because the lower it is, the better ratio signal/background we get.

We set the cut so that the inclusive sample contamination is one per thousand, i.e. $E_{sum} \sim 3GeV$ ($log_{10}E_{sum} \sim 0.5$). This cut keeps about 18% of the diffractive candidates.

[4] As written earlier, the luminosity is not recorded for diffractive triggers, thus the cross-section measurement is not possible.

[5] The behaviour of the plots at lower values is omitted, because the fraction of the diffractive data is too low in this region.

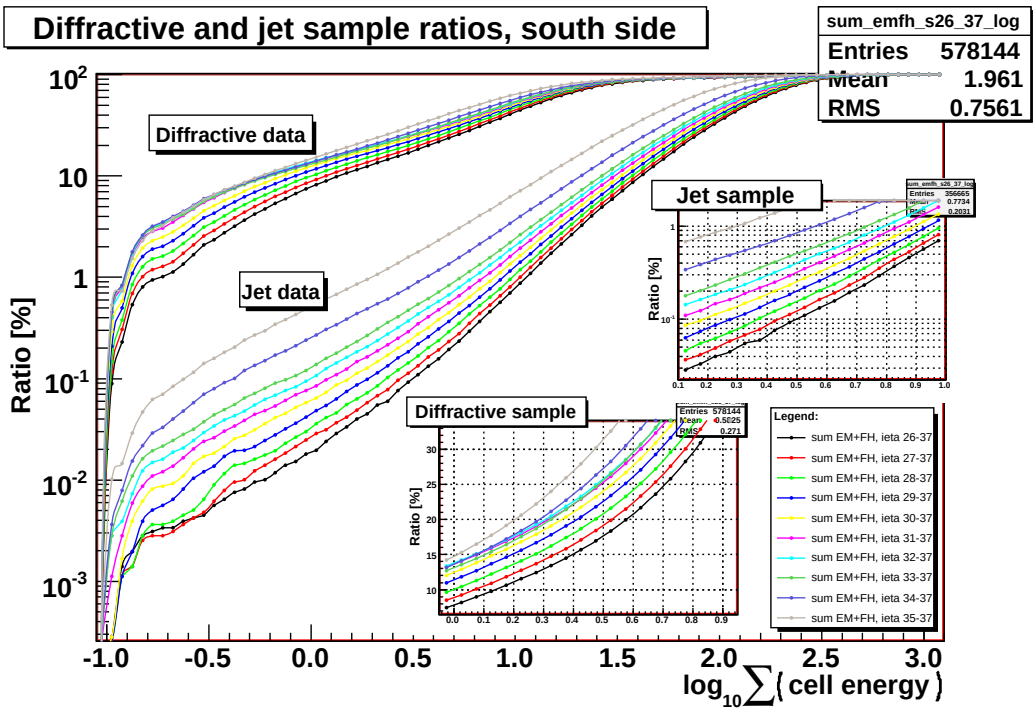

Figure 5.31: The percentage of number of events under a cut (represented by *x*-axis) to the total number of events for inclusive (in the lower part) and south diffractive (in the upper part) sample. The plots show the energy sums of calorimeter cells in ieta intervals up to 37.

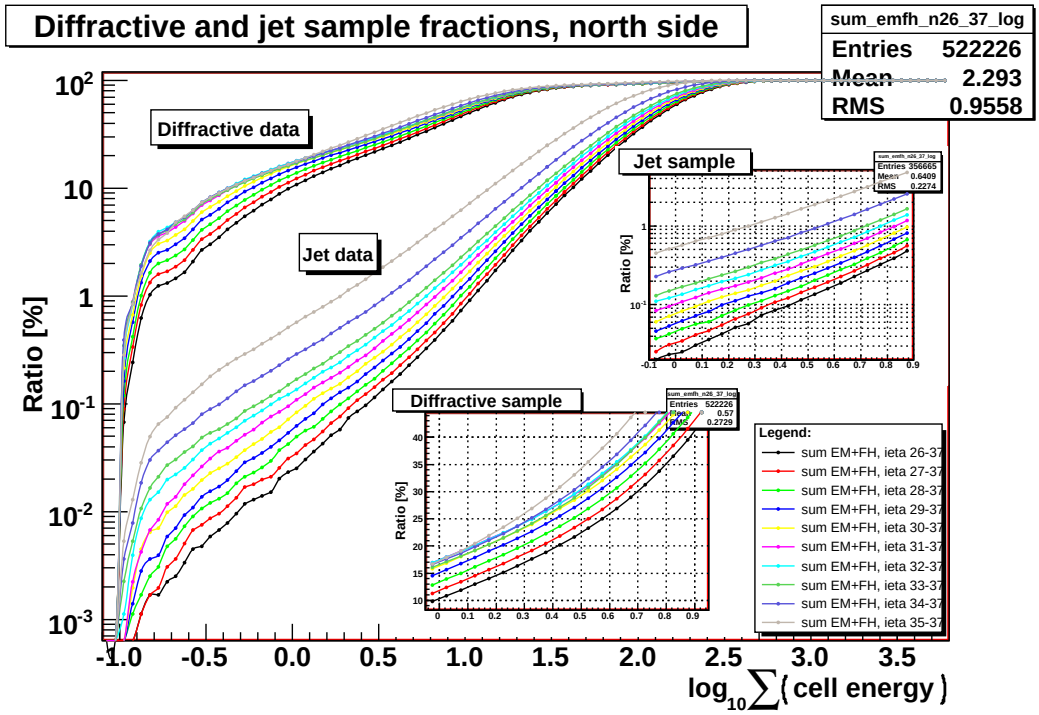

Figure 5.32: The percentage of number of events under a cut (represented by x-axis) to the total number of events for inclusive (in the lower part) and north diffractive (in the upper part) sample. The plots show the energy sums of calorimeter cells in ieta intervals up to 37.

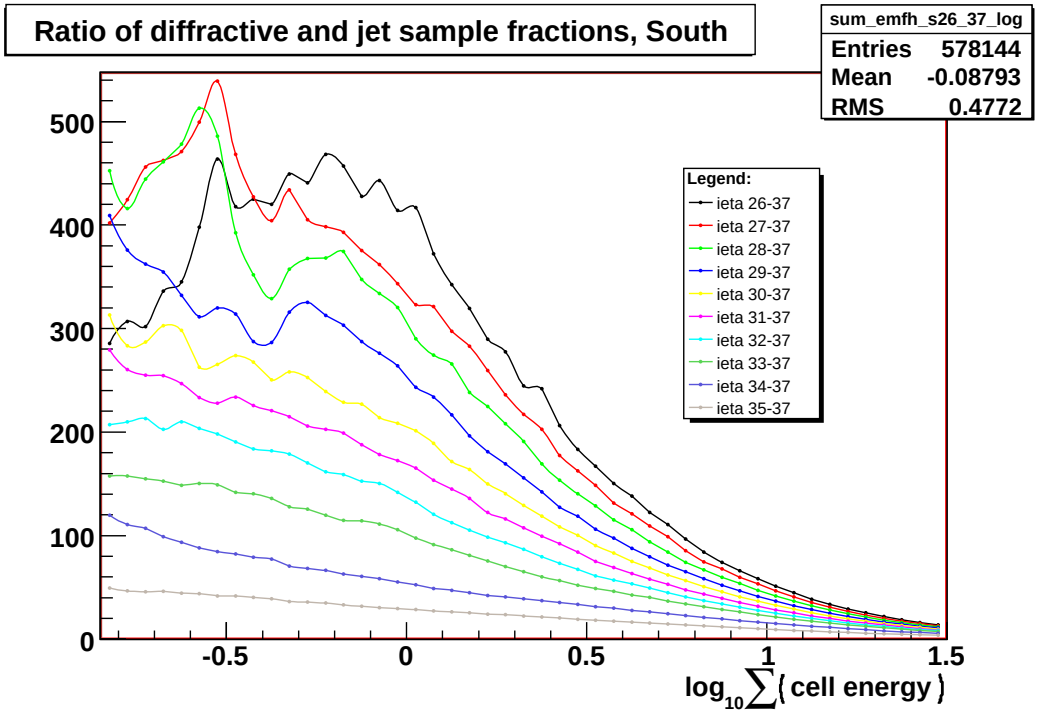

Figure 5.33: A quotient of the south diffractive sample and inclusive sample fraction plots from Fig. 5.31.

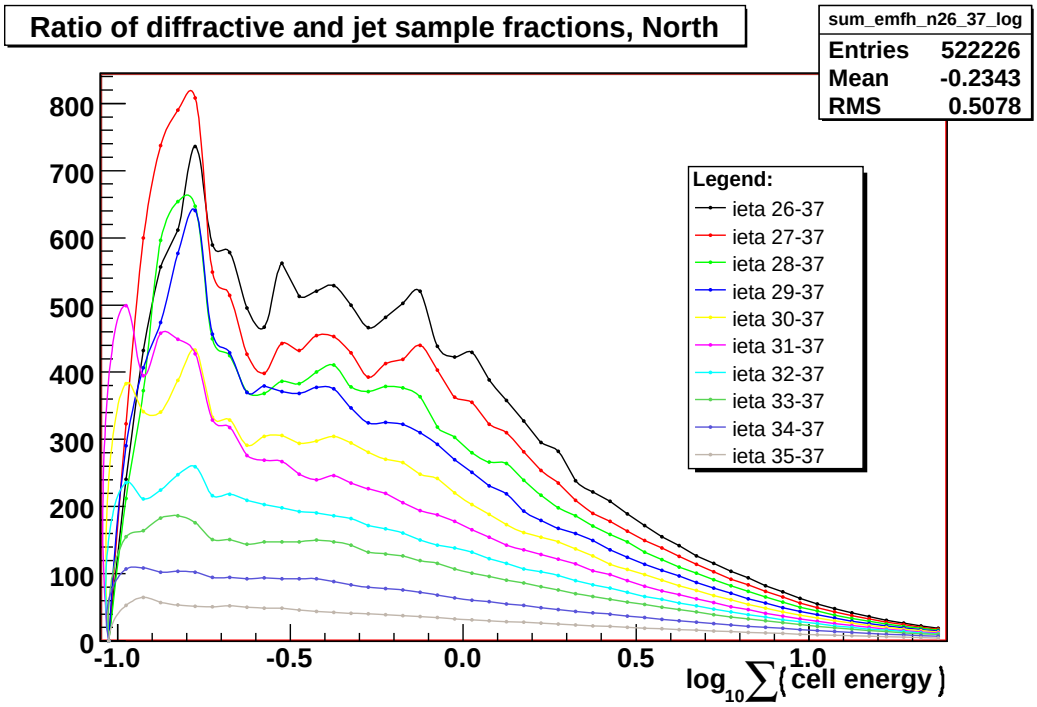

Figure 5.34: A quotient of the north diffractive sample and inclusive sample fraction plots from Fig. 5.32.

Chapter 6

$\Delta\phi$

6.1 $\Delta\phi$ Distribution

$\Delta\phi$ is a difference in azimuthal angle between two leading jets (ordered according to p_T)

$$\Delta\phi = |\phi_1 - \phi_2|$$

This quantity is an invariant under a boost along the beam axis and is directly sensitive to the higher order pQCD radiation, even when the third or higher jets are not reconstructed. Thus it is a suitable variable to probe the inner dynamics of a given process.

A basic formula for plotting $\Delta\phi$ between two jets is

$$\left| \frac{1}{N} \frac{dN}{d\Delta\phi} \right|_{bin} = \frac{1}{N} \frac{S_{bin} N_{bin}}{B_{width}} \tag{6.1}$$

where N is a total number of events in all bins, S_{bin} is an unsmearing correction in the bin (see below), B_{width} is a bin width and N_{bin} is a weighted sum of events in the bin.

The technical studies in the previous chapters were separated for north and south sides of the calorimeter. In general, no big differences were found. In fact no physical analysis should depend on the direction of the measured quantities. The $\Delta\phi$ distributions are compared for north and south diffractive samples in Fig. 6.1. The difference is negligible, therefore in further analysis these two samples are combined together.

$\Delta\phi$ distributions for the three basic diffractive triggers (see chapter 4) are plotted in Fig. 6.2-6.4. The events used in the plots are after all selection criteria and all jets are after the jet energy scale (JES) corrections. Bin sizes vary from $\pi/128$ rad

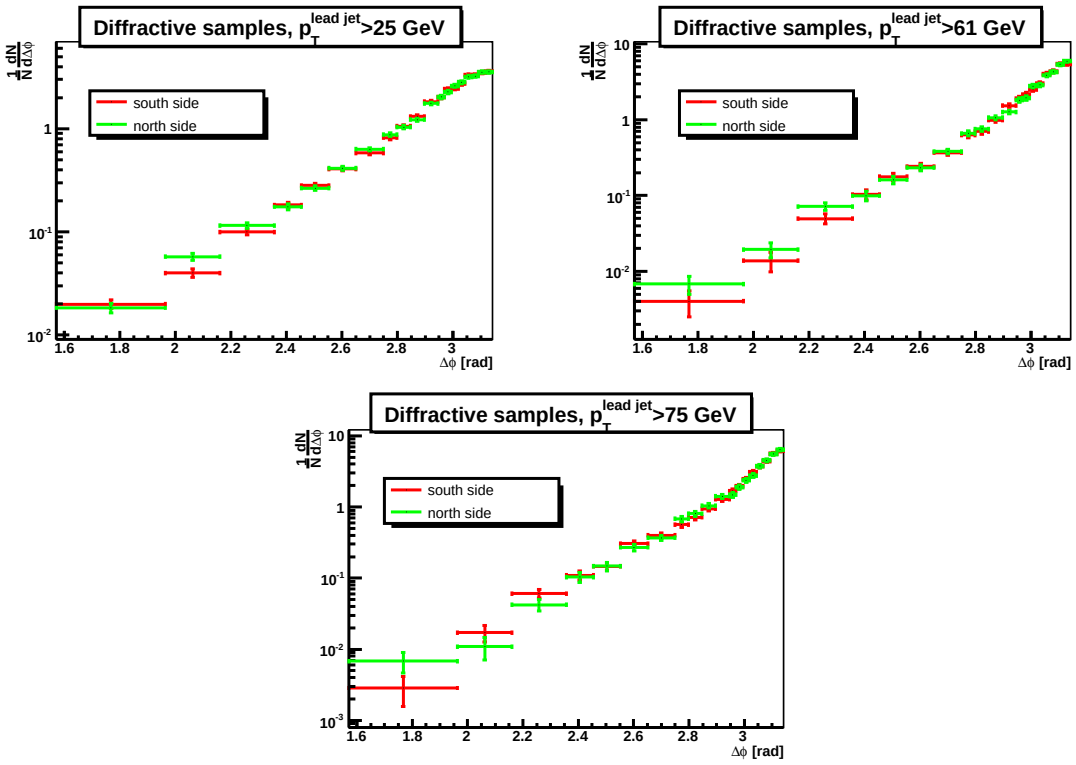

Figure 6.1: Comparison of the $\Delta\phi$ distribution for diffractive events with gap on south (red) and north (green) side of the calorimeter.

in the higher bins to $\pi/8$ rad in the lower values to reflect the number of events in the given intervals. The plots are shown only in the interval $(\pi/2, \pi)$ to avoid the region where the two jets can overlap (jet radius is 0.7, $2R < 1.4$).

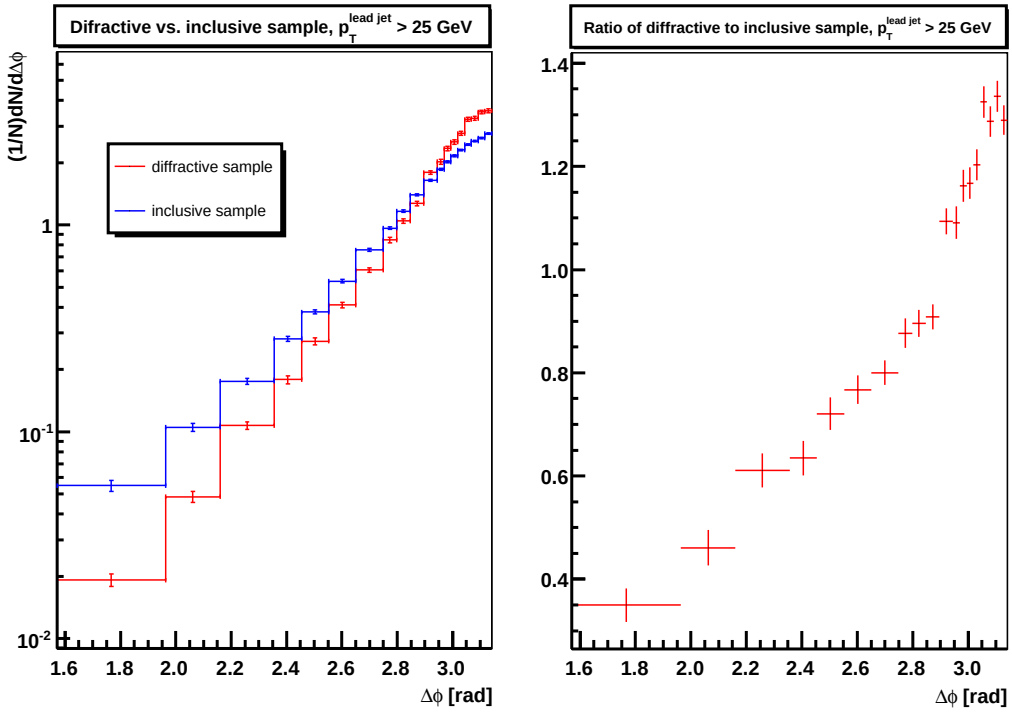

Figure 6.2: Uncorrected $\Delta\phi$ distributions of inclusive and diffractive samples for events with leading jet $p_T > 25$ GeV. On the right, the ratio of the two distributions is given.

As discussed in the chapter on gap definition, the rapidity gap can be defined in various ways. The influence of different gap definitions is shown in Fig. 6.5.

The differences are quite small, so the $\Delta\phi$ distribution does not depend much on the energy sum used in the definition. On the other hand, the condition on luminosity monitor seems to be important, because all three distributions have similar behaviour, which is clearly far from the inclusive sample.

6.2 Unsmearing Corrections

Any physical measurement is influenced by the finite detector resolution. Measured values of some quantity then differ from the *particle level* values as they arose

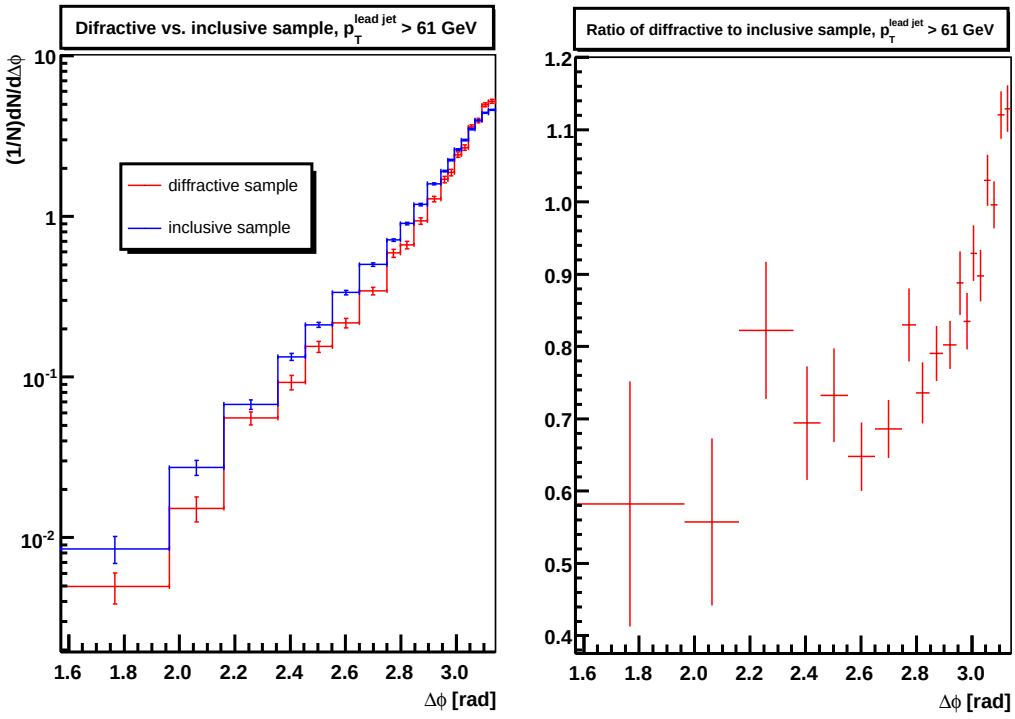

Figure 6.3: Uncorrected $\Delta\phi$ distributions of inclusive and diffractive samples for events with leading jet $p_T > 61$ GeV. On the right, the ratio of the two distributions is given.

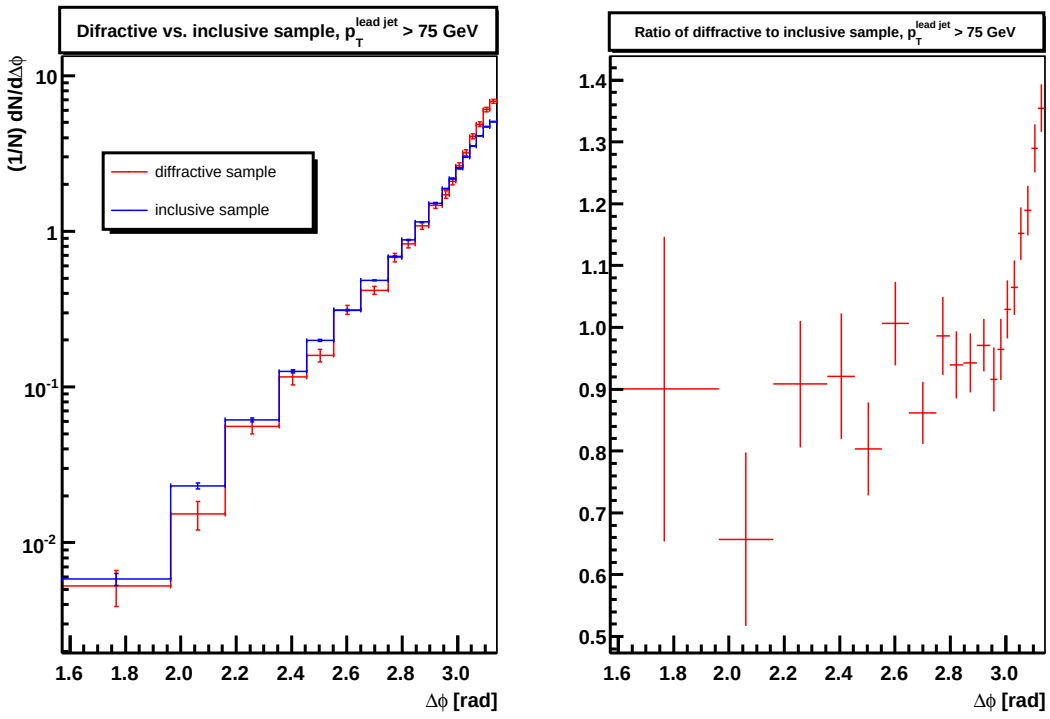

Figure 6.4: Uncorrected $\Delta\phi$ distributions of inclusive and diffractive samples for events with leading jet $p_T > 75$ GeV. On the right, the ratio of the two distributions is given.

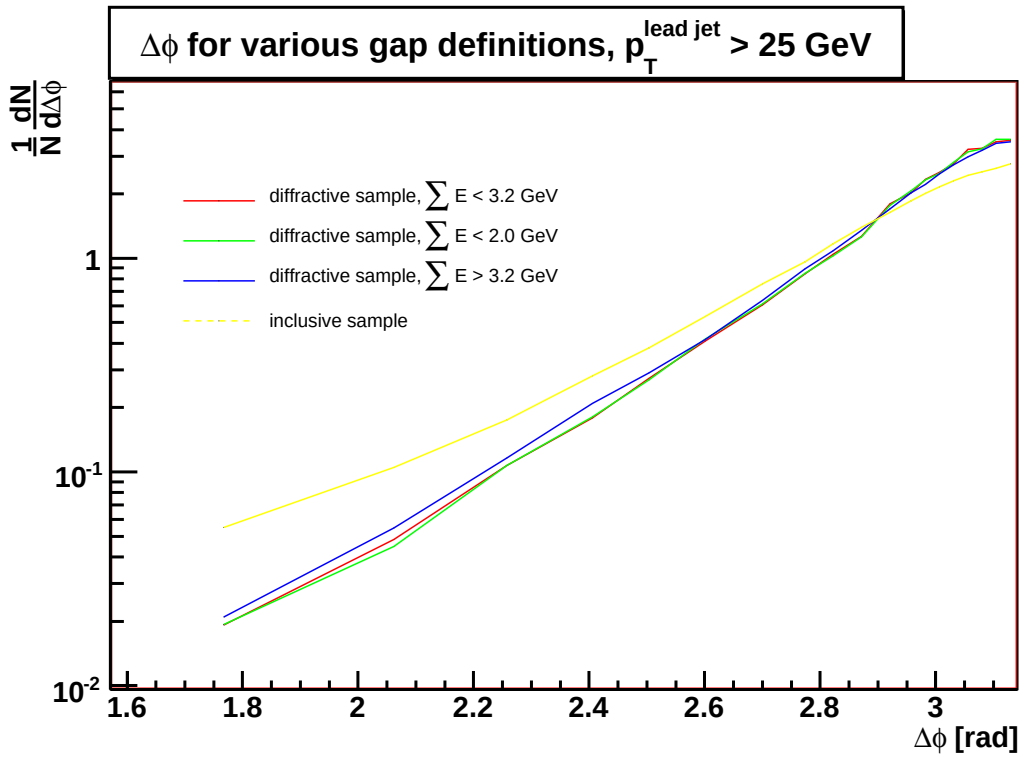

Figure 6.5: Uncorrected $\Delta\phi$ distributions of diffractive samples defined with various gap definitions. The rapidity interval is [26,37], and three various energy sum limits are used. Distribution of inclusive sample is shown for comparison.

during the interaction. To measure the real physical properties of the interactions, *an unsmearing (or unfolding) procedure* is used to eliminate the detector influence. The best possibility to find the unsmearing corrections is to use the full Monte Carlo simulations and to read the detector influence from that. Unfortunately, the full diffractive MC simulations were not performed at the time of writing this thesis, so only the partial detector resolutions, as measured by the QCD group, were used.

Generally, the detector changes a distribution of a quantity on particle level as a convolution of the distribution function with the gaussian error (smearing) function:

$$F_{smeared}(x) = (F_{part} \otimes G(\bar{x},\sigma))(x) = \int dy\, F_{part}(y) G(0,\sigma(y))(x-y) \quad (6.2)$$

$$G(\bar{x},\sigma)(x) = \frac{1}{\sqrt{2\pi}\,\sigma} \exp\left(-\frac{(x-\bar{x})^2}{2\sigma^2}\right) \quad (6.3)$$

It implies that the steeper the distribution is, the bigger is the error coming from smearing. It also implies that the unsmearing corrections depend on the shape of the distribution, so they must be determined for every distribution separately.

The smearing function is a property of the detector and remains unchanged in any analysis. In principle, if the analytical distribution function was known, it could be possible to find the unsmearing corrections analytically. But this function is not generally known, moreover for most functions the computation would be too complicated or would not be possible at all. Therefore a method of parton level Monte Carlo simulation is used.

At first, the data are produced using the Monte Carlo generator Pomwig (see chapter 7) and smeared with the measured detector resolution function. The searched quantity is then plotted using the smeared Monte Carlo data and compared to the detector data distribution. If the resulting MC function agrees with the measured distribution, it can be assumed that the original Monte Carlo distribution (before smearing) corresponds to the particle level distribution of the measurement[1]. If the smeared Monte Carlo does not describe the data distribution, then the original Monte Carlo is re-parametrized and the procedure is repeated. The parametrization is performed event by event with the fitted ratio of the smeared MC to the data distribution.

In the end, the unsmearing corrections are determined as a bin by bin ratio of original MC distribution to the smeared MC distribution.

[1]This approach is similar to the simpler case, when there is only one variable that influence the measurement. In this case a parametric ansatz distribution function can be used instead of Monte Carlo to describe the distribution. This function depends on one variable only, so it can be easily smeared and then the function parameters can be fitted to describe the searched distribution.

The detector resolutions, which are assumed in this analysis to affect the $\Delta\phi$ measurements are of two types: jet ϕ and jet p_T resolution. The influence of jet *phi* resolution on $\Delta\phi$ is clear, uncorrectly measured p_T can change the ordering of the jets (it can switch the 2^{nd} and 3^{rd} leading jet) or it can cause the migration of events because of the p_T cuts.

Detector ϕ resolution is determined from Monte Carlo simulation and the searched function is [35]

$$\sigma_\phi(E_{jet}) = \sqrt{A^2 + \frac{B^2}{E_{jet}} + \frac{C^2}{E_{jet}^2}} \tag{6.4}$$

with parameters stated as A=0.007, B=0, C=1.441.

Jet p_T resolution was measured directly from data, using clear dijet events. From the imbalance in jet p_T, the *relative* σ function was measured [36]:

$$\frac{\sigma_{p_T}}{p_T} = \sqrt{A^2 + \frac{B^2}{p_T} + \frac{C^2}{p_T^2}} \tag{6.5}$$

Parameters depend on ieta region, where the jets are found and are shown in Table 6.1.

η-region	A	B	C
$\lvert\eta\rvert < 0.5$	0.057	0.942	3.03
$0.5 < \lvert\eta\rvert < 1.0$	0.059	1.099	2.58
$1.0 < \lvert\eta\rvert < 1.5$	0.085	1.200	0.001
$1.5 < \lvert\eta\rvert < 2.0$	0.091	0.001	4.91
$2.0 < \lvert\eta\rvert$	0.045	0.013	4.49

Table 6.1: Parameters used for jet p_T resolution.

The $\Delta\phi$ distributions compared to Monte Carlo predictions are shown in Figures 6.6 - 6.11. The plots show the original Monte Carlo and MC smeared using the parameters described above. The ratio of the data and the smeared MC is shown with the fit on the right side of the plots. The fit is then used to reweight the Monte Carlo. The new MC $\Delta\phi$ and the quotient of data to reweighted MC are shown in the same plots. The reweighted MC determines the unsmearing corrections, which are shown in Fig. 6.12 and 6.13.

The final results of the $\Delta\phi$ distribution after all corrections, including unsmearing, are shown in Figures 6.14 - 6.16.

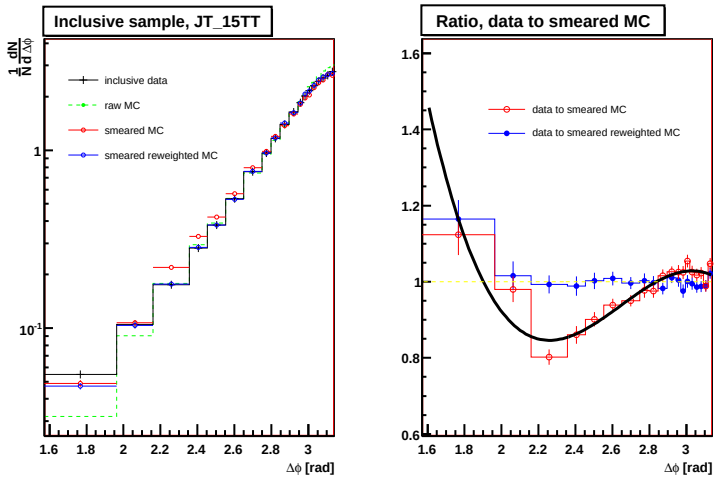

Figure 6.6: Herwig distribution of $\Delta\phi$ compared to inclusive data sample. Distributions before and after the smearing with the detector resolution parameters are shown, as well as a distribution after reweighting and smearing the Monte Carlo. Right side shows the ratios of data to Monte Carlo (before and after reweighting). A solid line shows the fit using the polynomial function.

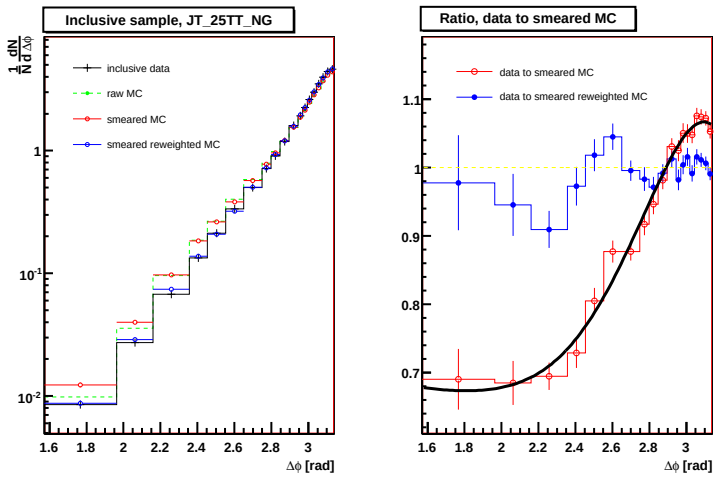

Figure 6.7: Herwig distribution of $\Delta\phi$ compared to inclusive data sample. Distributions before and after the smearing with the detector resolution parameters are shown, as well as a distribution after reweighting and smearing the Monte Carlo. Right side shows the ratios of data to Monte Carlo (before and after reweighting). A solid line shows the fit using the polynomial function.

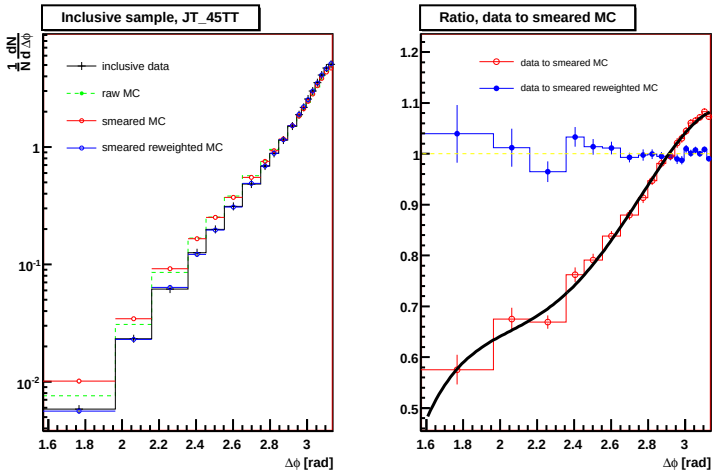

Figure 6.8: Herwig distribution of $\Delta\phi$ compared to inclusive data sample. Distributions before and after the smearing with the detector resolution parameters are shown, as well as a distribution after reweighting and smearing the Monte Carlo. Right side shows the ratios of data to Monte Carlo (before and after reweighting). A solid line shows the fit using the polynomial function.

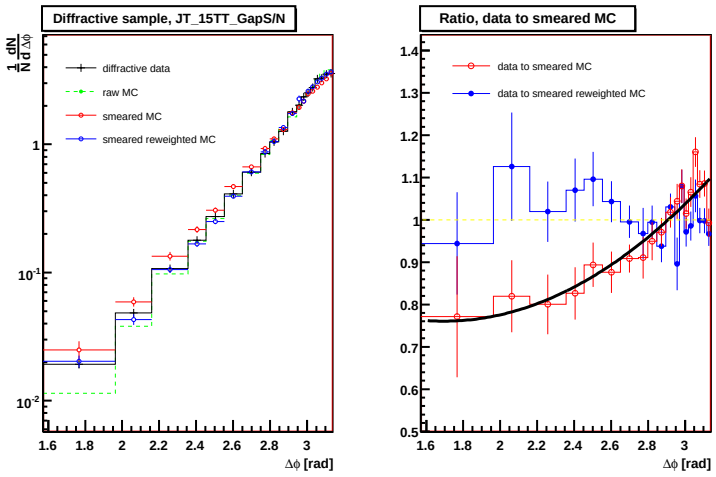

Figure 6.9: Pomwig distribution of $\Delta\phi$ compared to diffractive data sample. Distributions before and after the smearing with the detector resolution parameters are shown, as well as a distribution after reweighting and smearing the Monte Carlo. Right side shows the ratios of data to Monte Carlo (before and after reweighting). A solid line shows the fit using the polynomial function.

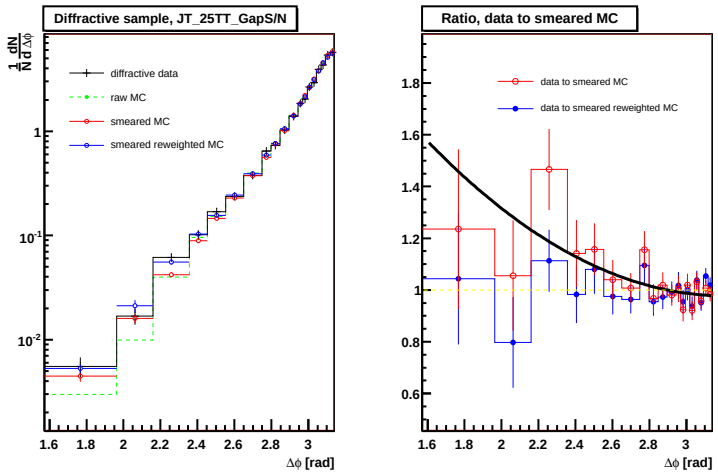

Figure 6.10: Pomwig distribution of $\Delta\phi$ compared to diffractive data sample. Distributions before and after the smearing with the detector resolution parameters are shown, as well as a distribution after reweighting and smearing the Monte Carlo. Right side shows the ratios of data to Monte Carlo (before and after reweighting). A solid line shows the fit using the polynomial function.

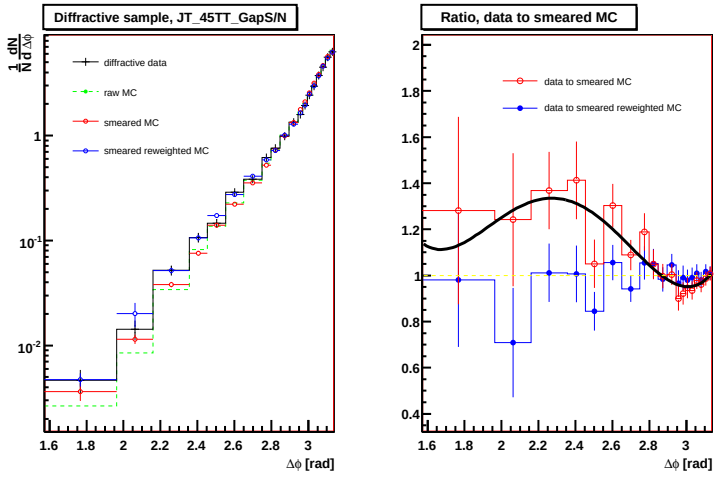

Figure 6.11: Pomwig distribution of $\Delta\phi$ compared to diffractive data sample. Distributions before and after the smearing with the detector resolution parameters are shown, as well as a distribution after reweighting and smearing the Monte Carlo. Right side shows the ratios of data to Monte Carlo (before and after reweighting). A solid line shows the fit using the polynomial function.

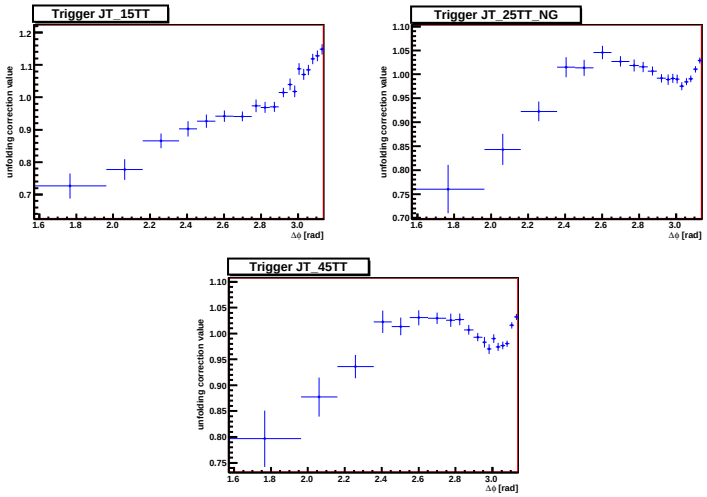

Figure 6.12: Unsmearing corrections of inclusive sample.

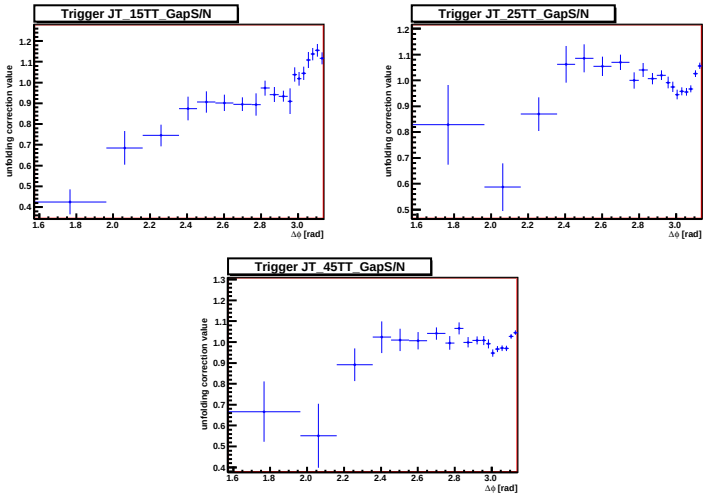

Figure 6.13: Unsmearing corrections of diffractive sample.

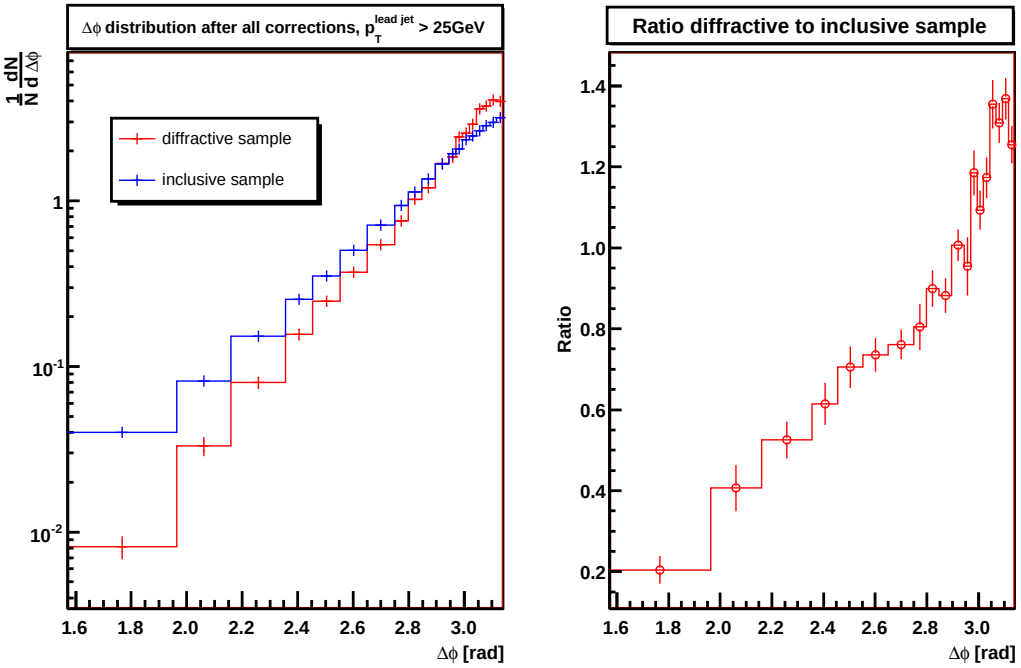

Figure 6.14: Final $\Delta\phi$ distribution after all corrections for jets with $p_T > 25$GeV.

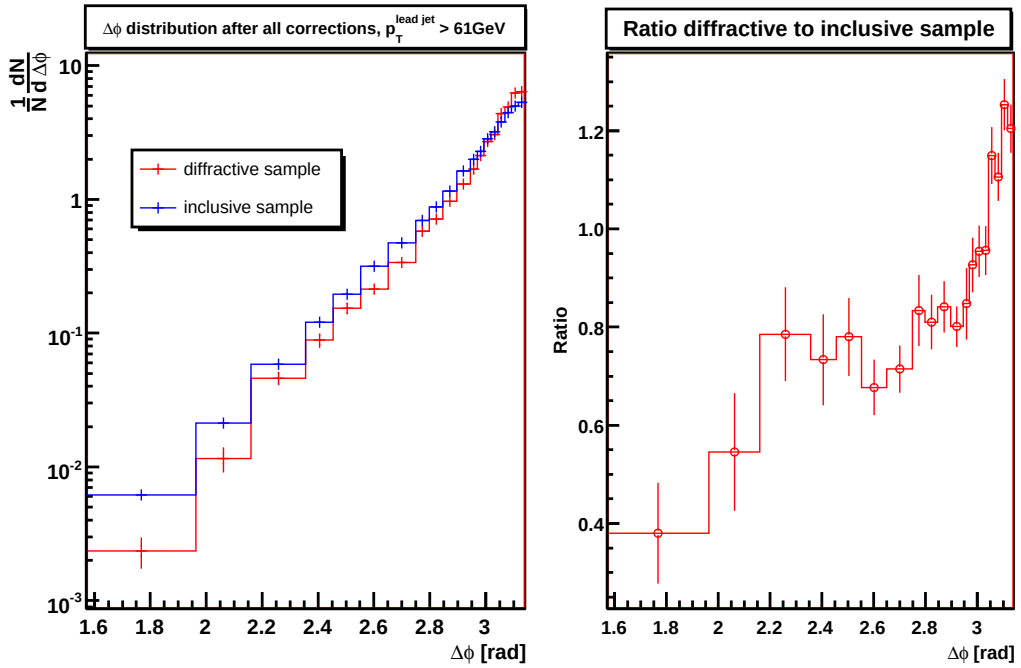

Figure 6.15: Final $\Delta\phi$ distribution after all corrections for jets with $p_T > 61$GeV.

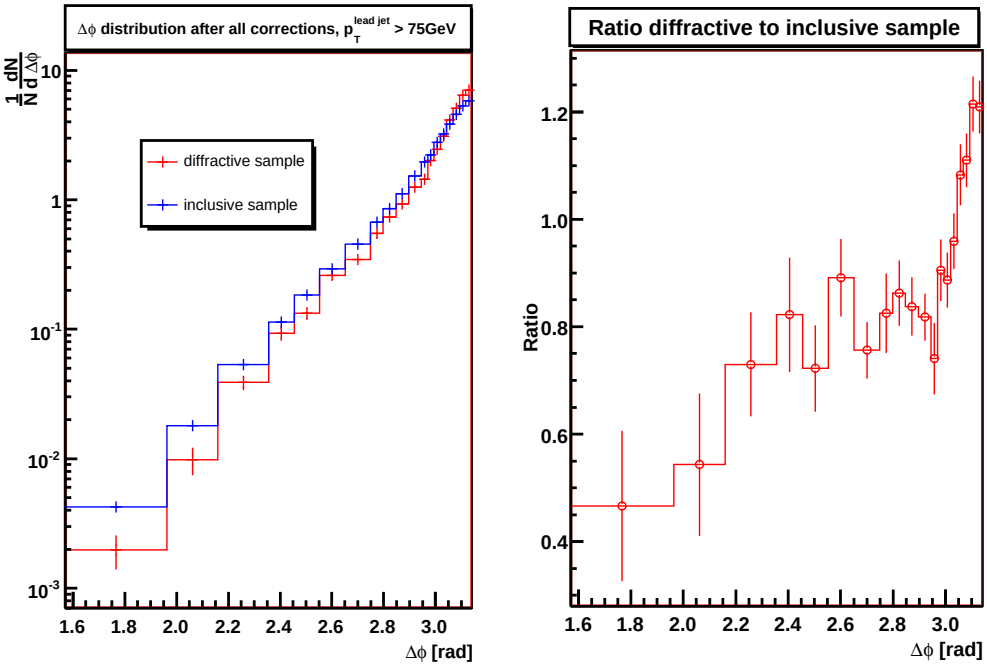

Figure 6.16: Final $\Delta\phi$ distribution after all corrections for jets with $p_T > 75$GeV.

Chapter 7

Monte Carlo

Pomwig was used as a Monte Carlo generator to compare the experimental diffractive results with theoretical predictions. It is a generator based on Herwig, which is capable to describe most, but not diffractive, physical processes. The limitation was solved in Pomwig in a way as simple as possible ([34]). The basic idea was to realize the similarity between pomeron exchange in hadron - hadron collisions and the photoproduction in electron - proton collisions. While an electron emits a photon according to a flux formula in an *eP* interaction, which interacts with the proton, single diffractive process can be treated as a pomeron emission from one of the beam protons according to some flux formula. This pomeron then collides with the second proton. Thus the only necessary change in Herwig to include diffractive processes was to replace a photon flux in an *eP* mode with some pomeron flux and to change the photon structure function to the pomeron structure function. The diffractive processes included in Pomwig are shown in Table 7.1. The beam definitions are shown as they appear in Pomwig output. The relevant flux(es) and structure function(s) of the E^+ beam(s) are automatically substituted with pomeron analogs. First row corresponds to a single diffractive process, second row to a double pomeron exchange and the third row to a diffraction process in electron-proton collision. Compared to Herwig, there are several new parameters in Pomwig de-

Process	Beam 1	Beam 2
PP $\rightarrow$ PX	P^+	E^+
PP $\rightarrow$ PPX	E^+	E^+
eP $\rightarrow$ ePX	E^-	E^+

Table 7.1: Possible processes in Pomwig generator

scribing properties of the pomeron. These are minimum and maximum virtuality

of the pomeron and minimum and maximum pomeron energy fraction (ξ variable). Default values are shown in Table 7.2.

Variable	Variable name	Default value
minimum virtuality	Q2WWMN	10^{-6}
maximum virtuality	Q2WWMX	4.0
minimum energy fraction	YWWMIN	0.0001
maximum energy fraction	YWWMAX	0.1

Table 7.2: Default values of the Pomeron parameters in Pomwig

The single diffractive processes were simulated, and generated events were passed through the standard D0 jet cone algorithm with the difference that outgoing particles were used instead of calorimeter towers. The resulting jets were smeared with measured p_T and ϕ detector resolutions to simulate the detector influence[1] (see previous chapter for resolution definitions) and the same kinematical selection criteria, as applied to the physical data, were used. The distributions of $\Delta\phi$ and p_T for Pomwig and for the data are shown in Fig. 7.1 - 7.6.

It is clear from the presented plots that the default Pomwig parameters (max $\xi = 0.1$) are ruled out by the diffractive data selected using the gap definition and restricted to high p_T central dijet events. On the other hand, when the max ξ parameter is increased to 0.4, the agreement with the data is very good. Further increasing of max ξ to 0.6 does not change the results any more. This corresponds to the definition of the ξ variable, which can be rewritten as:

$$\xi = \frac{1}{\sqrt{s}} \sum_i E_T^i e^{-\eta_i} \,, \tag{7.1}$$

where the sum goes over all particles. This statement can be easily derived from Eq. 2.15. According to this equation, the observed very high p_T central dijets must correspond to ξ higher than 0.1. On the other hand, according to [32, 37], the theoretical maximum ξ is believed to be smaller than 0.15. This introduces interesting questions for further studies, which are not solved in this dissertation.

[1] Full Monte Carlo, which simulates all aspects of the D0 detector and propagates the generated outgoing particles through it, was not available in the time of writing this thesis.

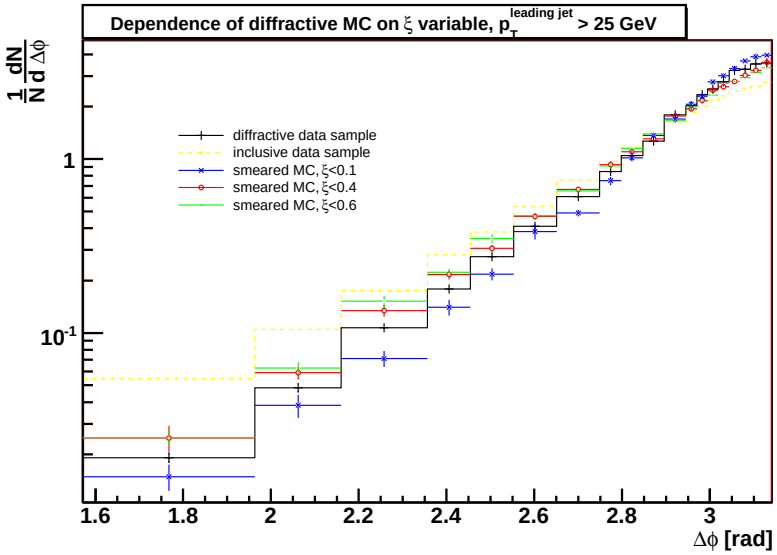

Figure 7.1: The dependence of $\Delta\phi$ distribution on smeared Pomwig generated data with various maximum ξ parameter. Comparison is made with diffractive JT_15TT_GapS/N sample. For illustration, the inclusive sample (dashed yellow line) after JT_15TT trigger is shown as well.

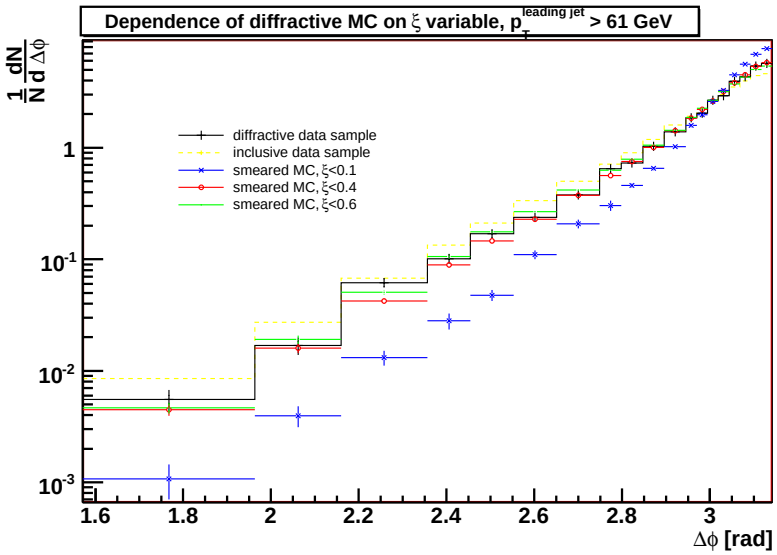

Figure 7.2: The dependence of $\Delta\phi$ distribution on smeared Pomwig generated data with various maximum ξ parameter. Comparison is made with diffractive JT_25TT_GapS/N sample. For illustration, the inclusive sample (dashed yellow line) after JT_25TT_NG trigger is shown as well.

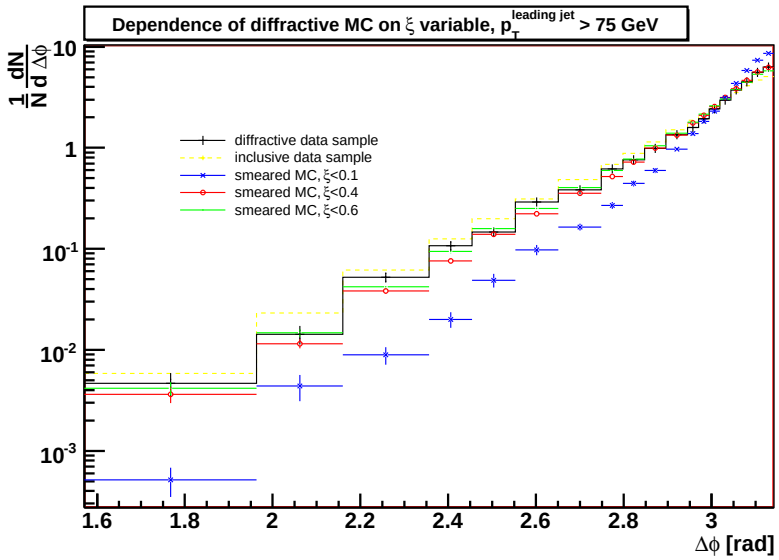

Figure 7.3: The dependence of $\Delta\phi$ distribution on smeared Pomwig generated data with various maximum ξ parameter. Comparison is made with diffractive JT_45TT_GapS/N sample. For illustration, the inclusive sample (dashed yellow line) after JT_45TT trigger is shown as well.

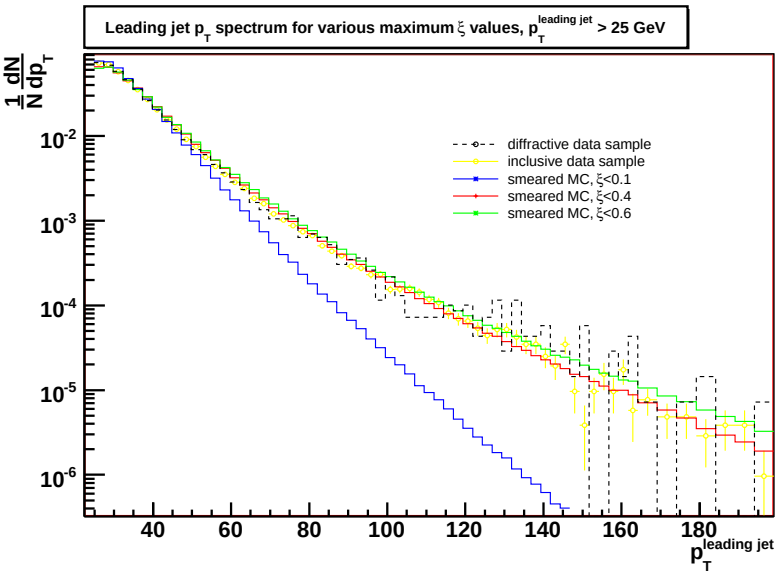

Figure 7.4: The p_T distribution for smeared Pomwig data in comparison to diffractive sample. Pomwig data are generated with various maximum ξ parameter. Trigger JT_15TT_GapS/N is used for diffractive data. For illustration, the inclusive sample (dashed yellow line) after JT_15TT trigger is shown as well.

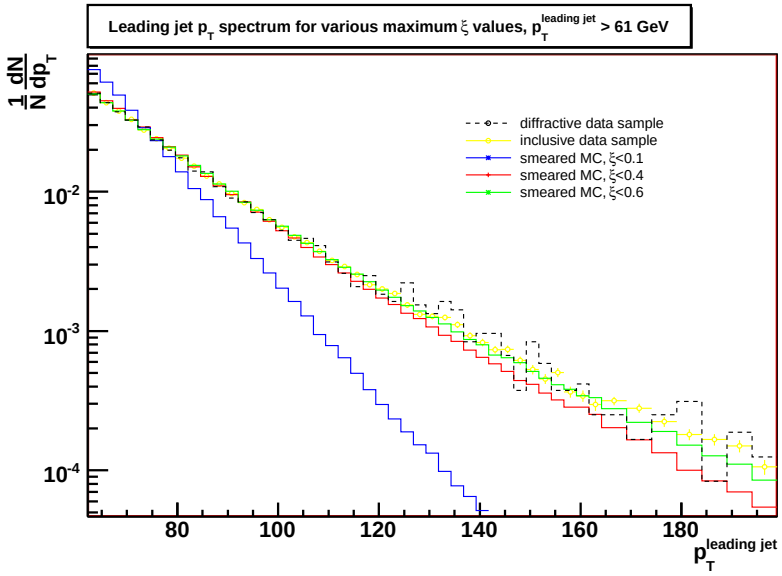

Figure 7.5: The p_T distribution for smeared Pomwig data in comparison to diffractive sample. Pomwig data are generated with various maximum ξ parameter. Trigger JT_25TT_GapS/N is used for diffractive data. For illustration, the inclusive sample (dashed yellow line) after JT_25TT_NG trigger is shown as well.

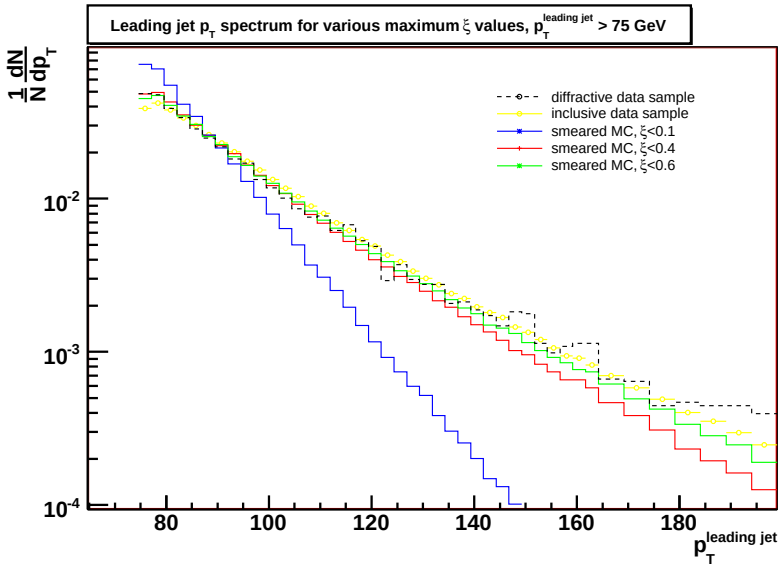

Figure 7.6: The p_T distribution for smeared Pomwig data in comparison to diffractive sample. Pomwig data are generated with various maximum ξ parameter. Trigger JT_45TT_GapS/N is used for diffractive data. For illustration, the inclusive sample (dashed yellow line) after JT_45TT trigger is shown as well.

Chapter 8

Other Distributions

Some other distributions are shown in this chapter to compare the properties of diffractive and inclusive dijet data. All events are after *all* selection criteria, all jets are after the JES corrections. Unsmearing corrections are not used in the following plots.

Dijet mass distribution is shown in Fig. 8.1.

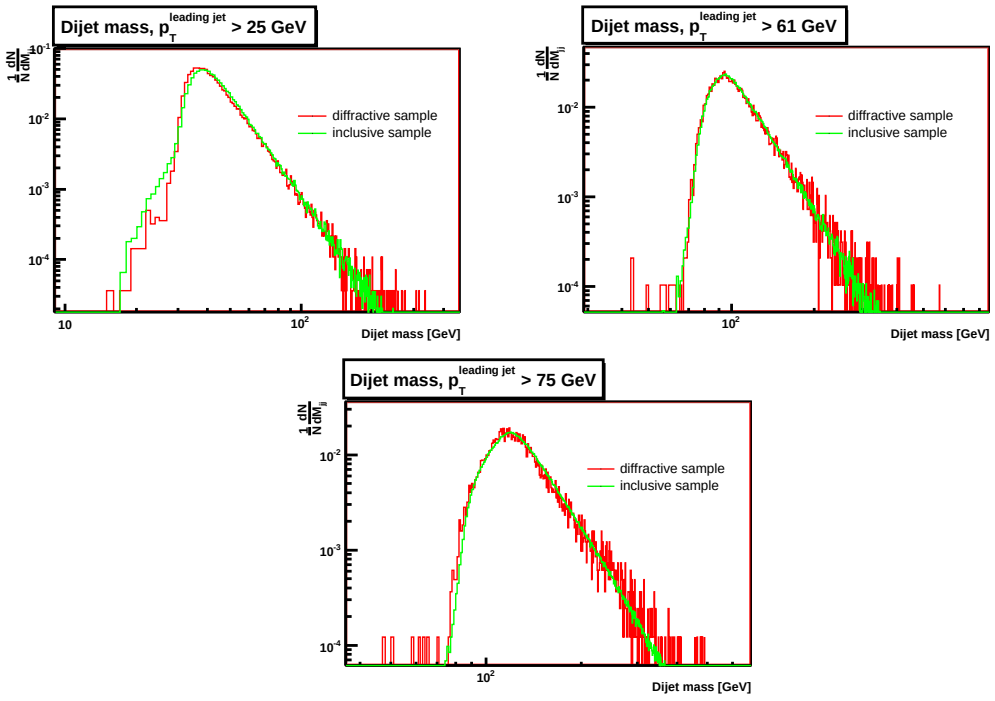

Figure 8.1: Comparison of the uncorrected dijet mass distributions for inclusive and diffractive samples.

The sum of p_T's of the two leading jets is computed as a transversal part of a 3-vector $\vec{p}_{jet1} + \vec{p}_{jet2}$. The distribution is shown in Fig. 8.2.

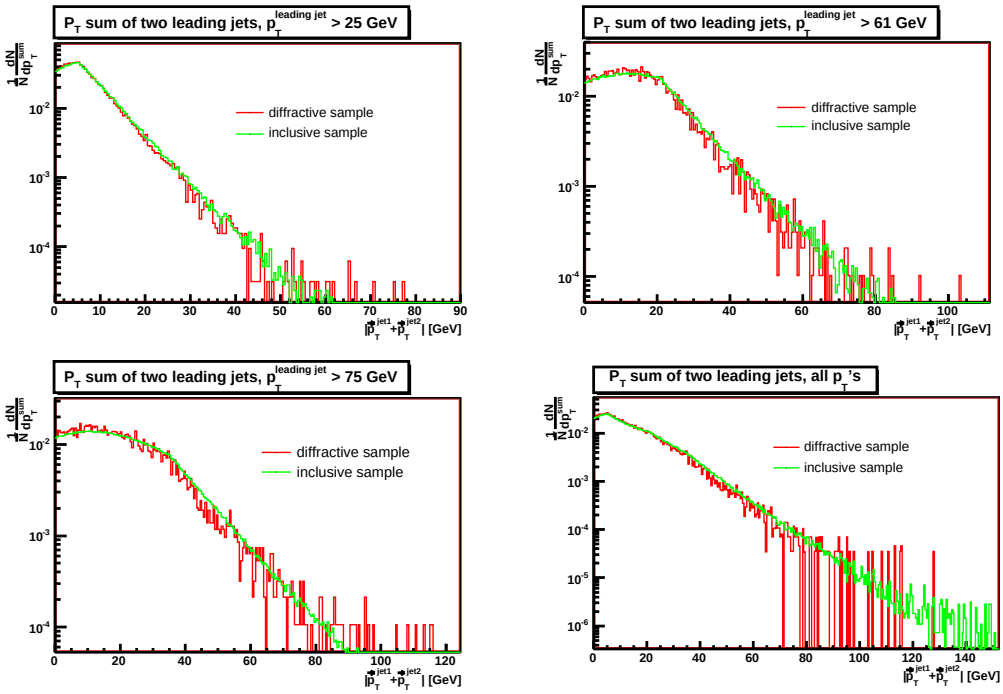

Figure 8.2: A sum of p_T's of first two leading jets for inclusive and diffractive samples.

The jet properties of leading and second leading jets are shown in Figures 8.3-8.10

The event selection variables are shown in Fig. 8.11-8.13

The p_T, ϕ and rapidity distributions are shown in Figures 8.14-8.19

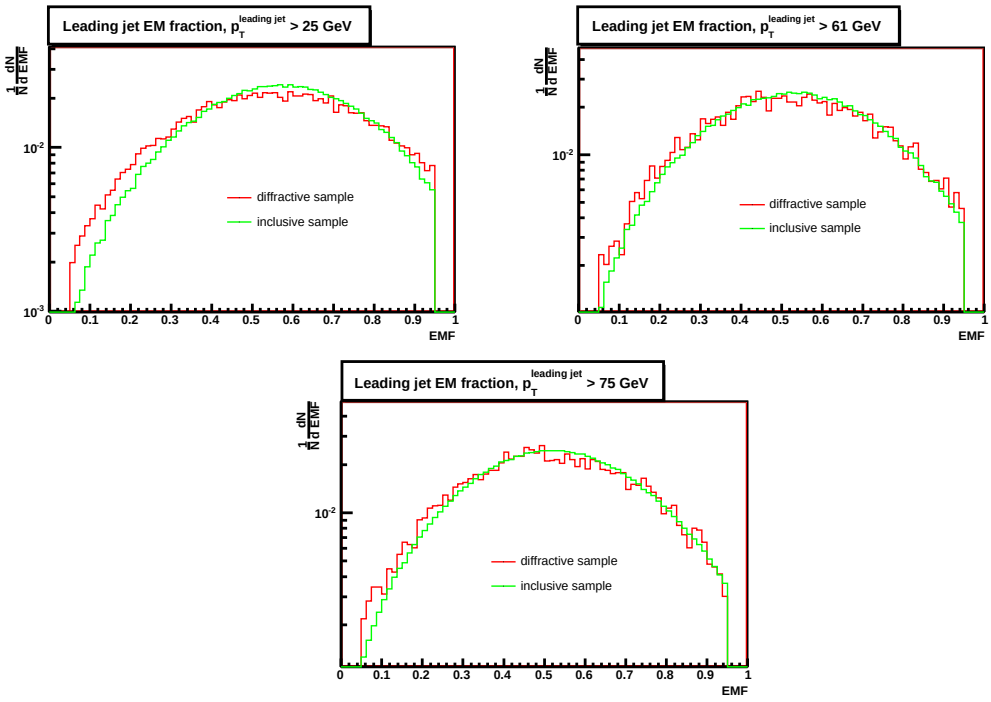

Figure 8.3: EM fraction of the leading jet for inclusive and diffractive samples.

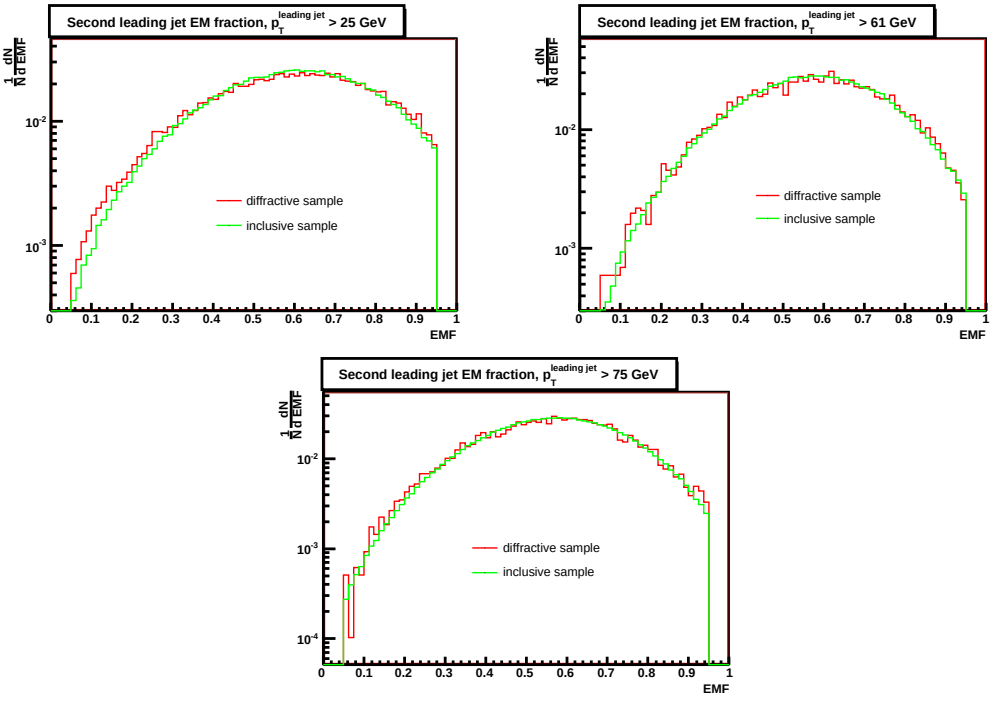

Figure 8.4: EM fraction of the second leading jet for inclusive and diffractive samples.

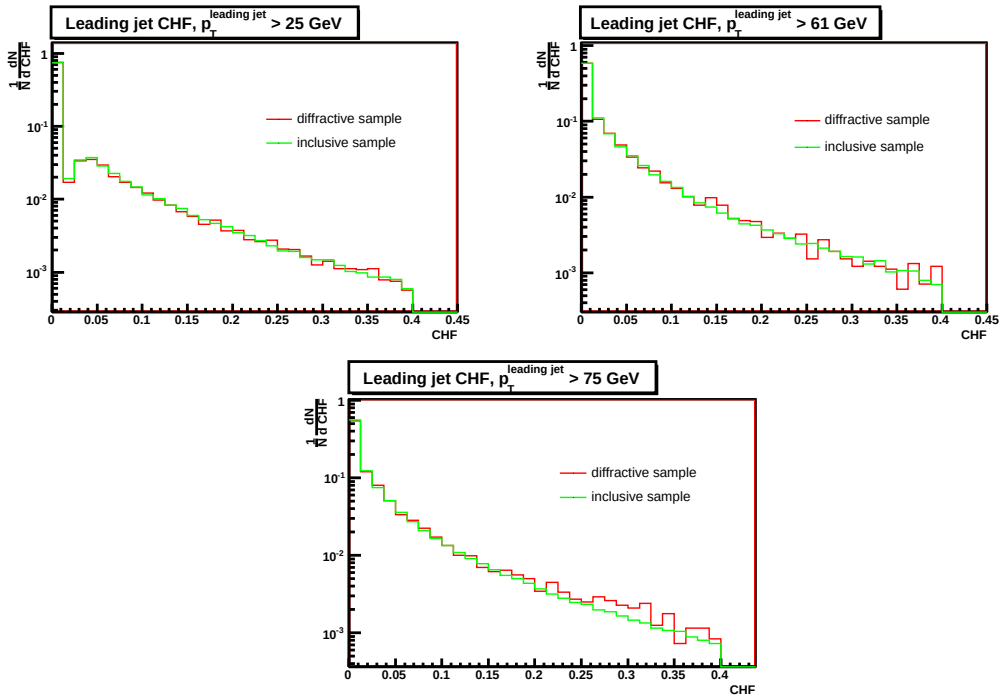

Figure 8.5: CH fraction of the leading jet for inclusive and diffractive samples.

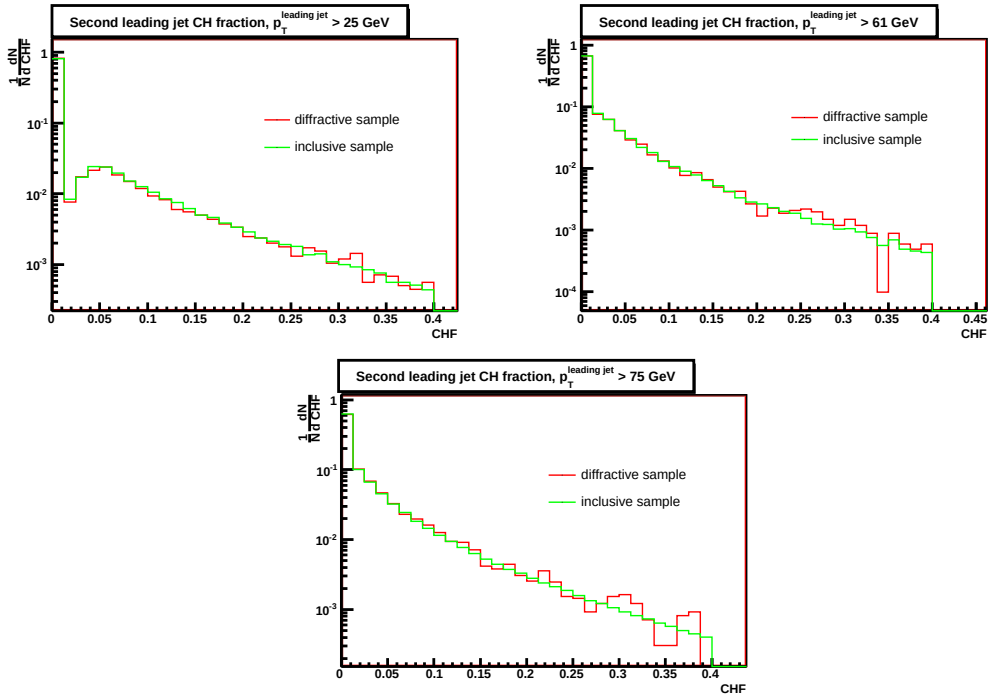

Figure 8.6: CH fraction of the second leading jet for inclusive and diffractive samples.

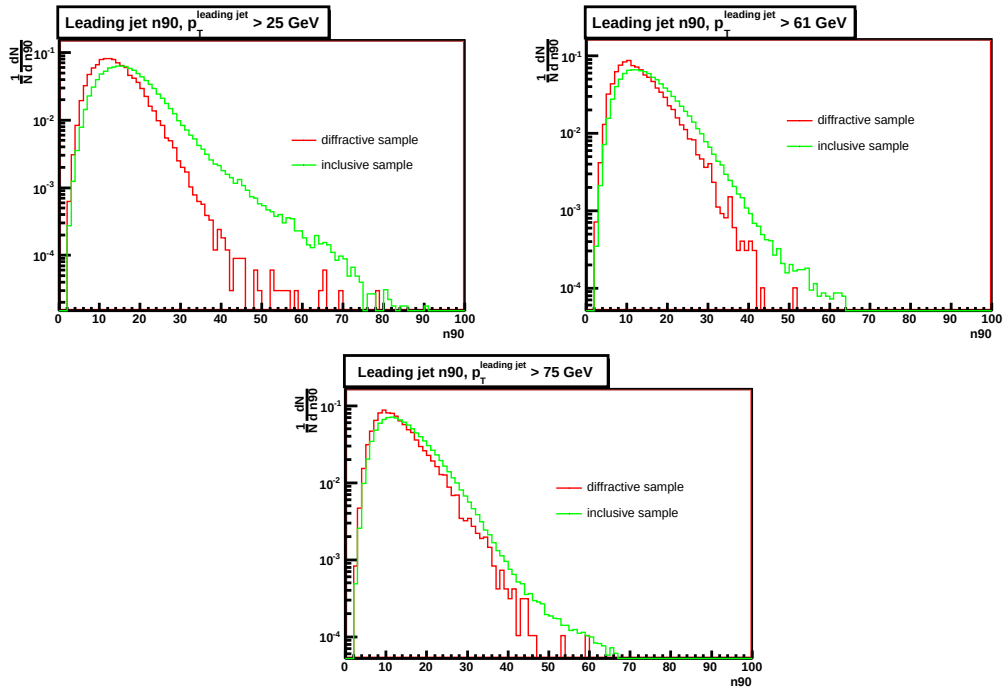

Figure 8.7: n90 variable of the leading jet for inclusive and diffractive samples.

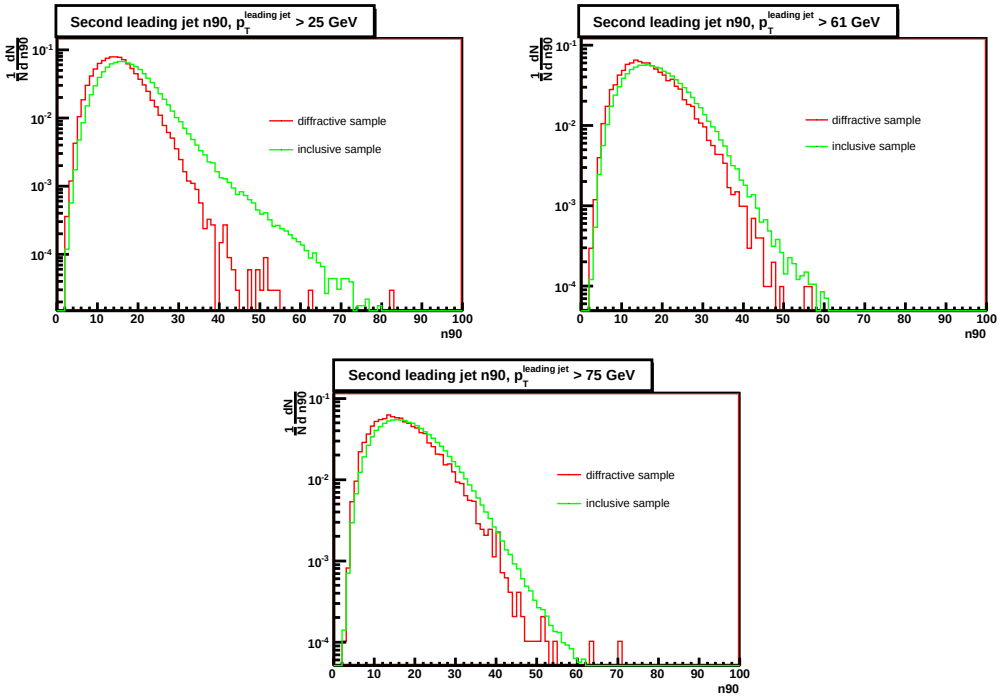

Figure 8.8: n90 variable of the second leading jet for inclusive and diffractive samples.

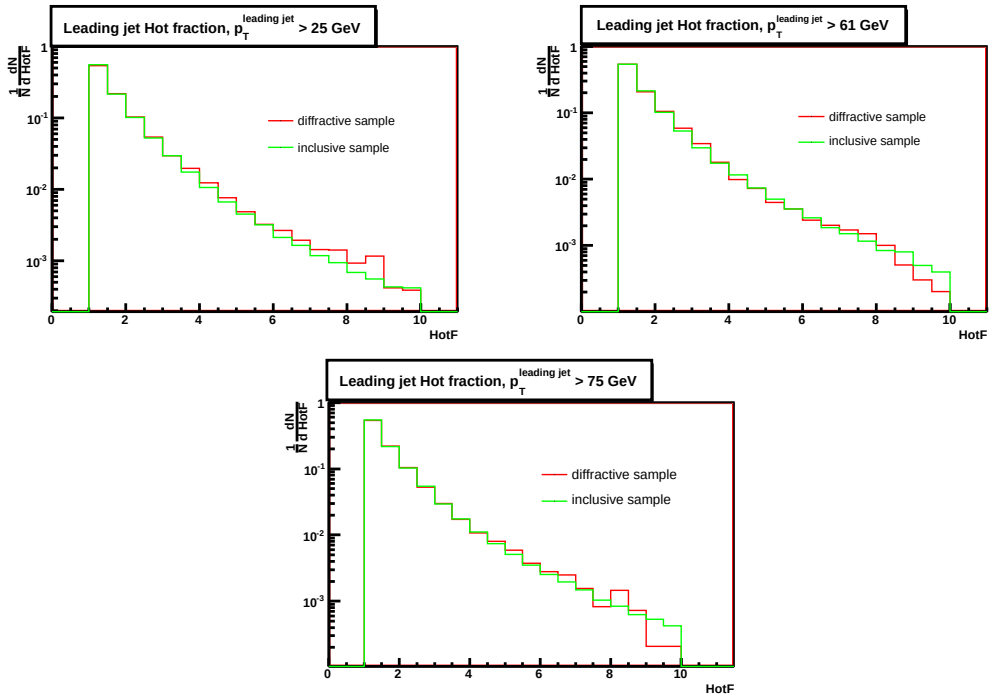

Figure 8.9: Hot cell fraction of the leading jet for inclusive and diffractive samples.

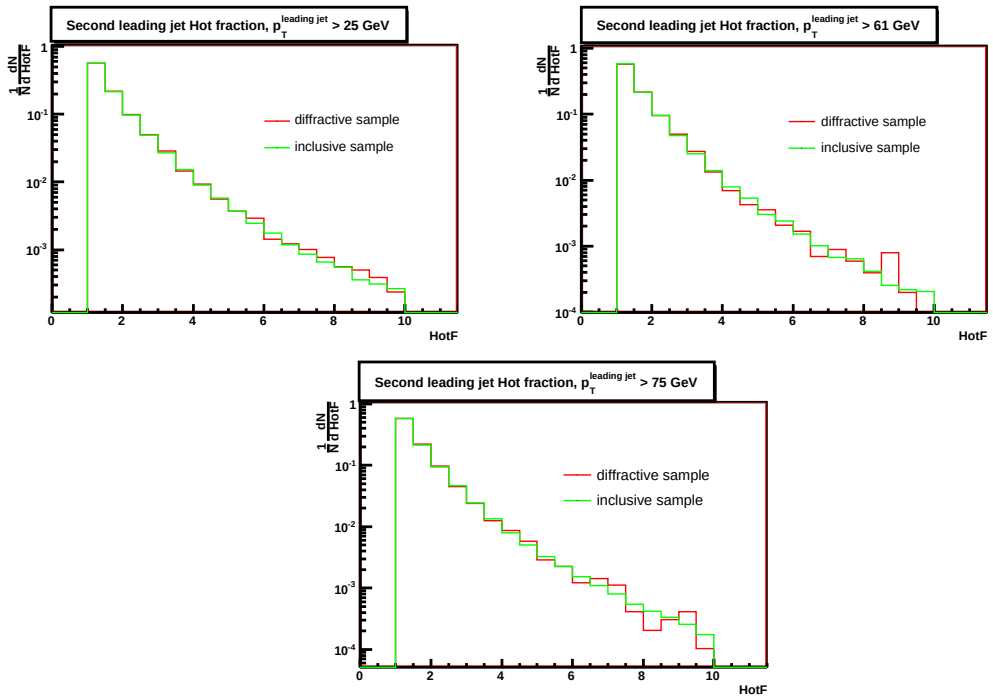

Figure 8.10: Hot cell fraction of the leading jet for inclusive and diffractive samples.

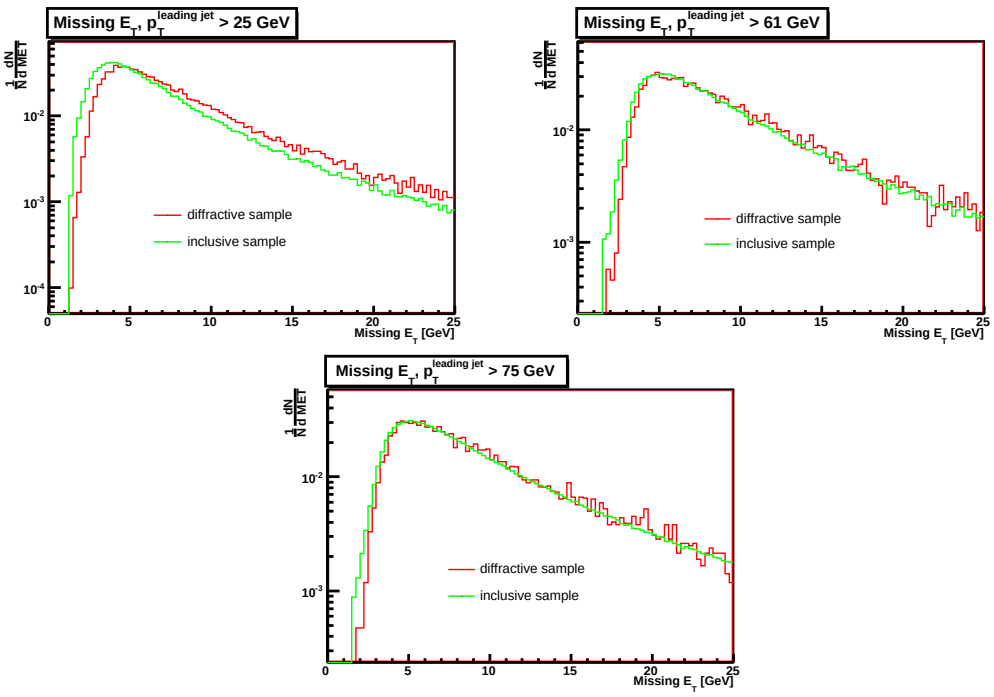

Figure 8.11: Missing E_T in the inclusive and diffractive events.

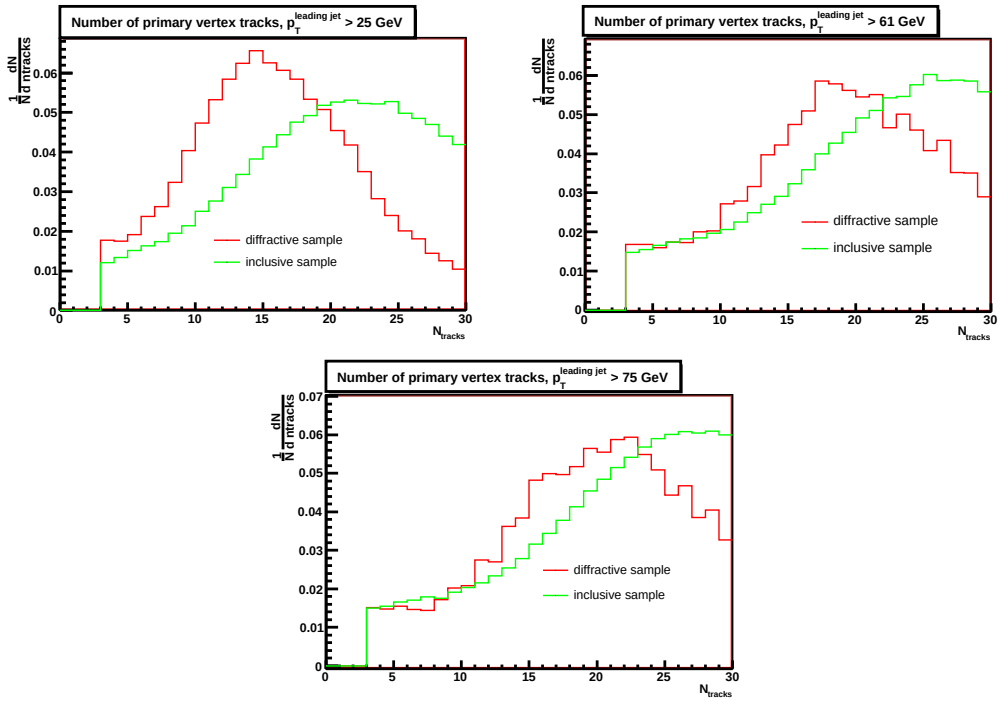

Figure 8.12: Number of tracks associated with the primary vertex in the inclusive and diffractive events.

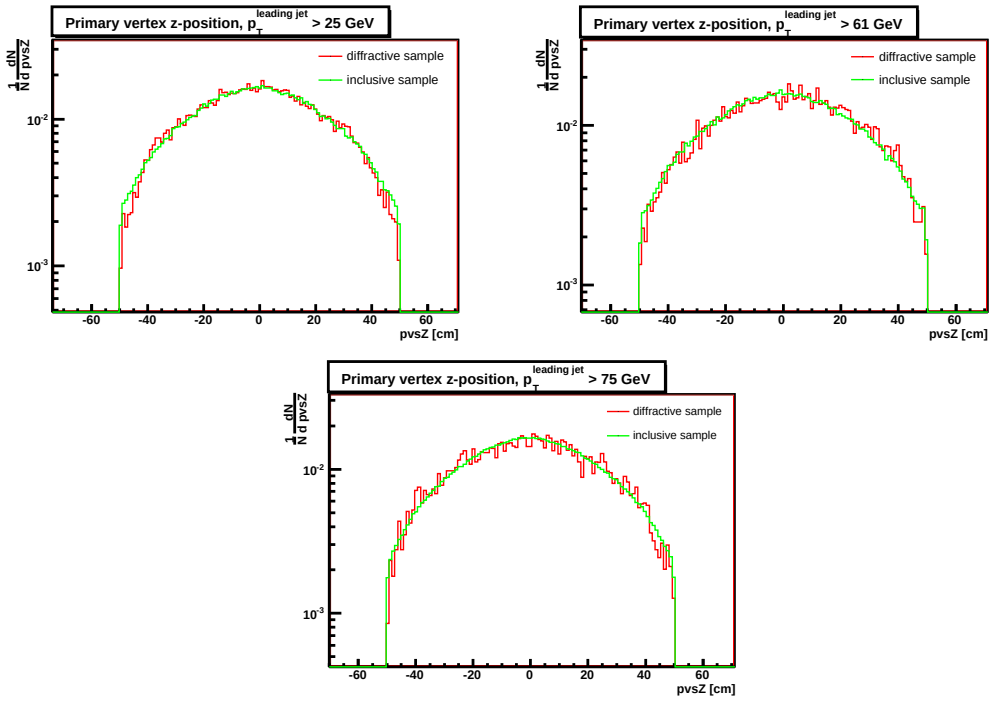

Figure 8.13: Z-position of the primary vertex in the inclusive and diffractive events.

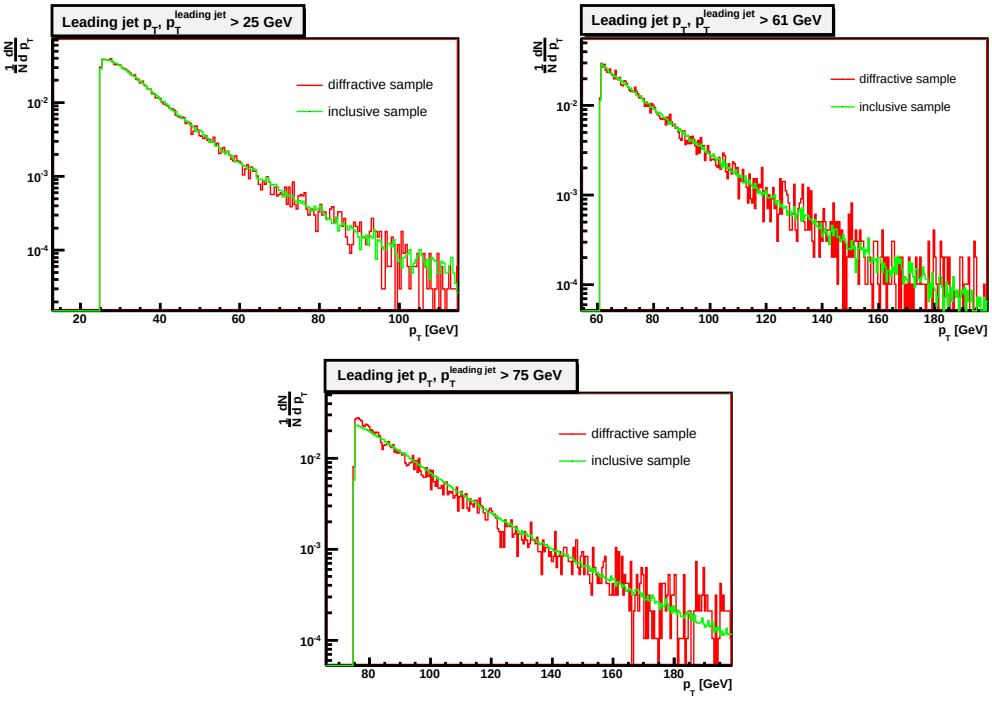

Figure 8.14: The distribution of p_T of the leading jet in the inclusive and diffractive sample.

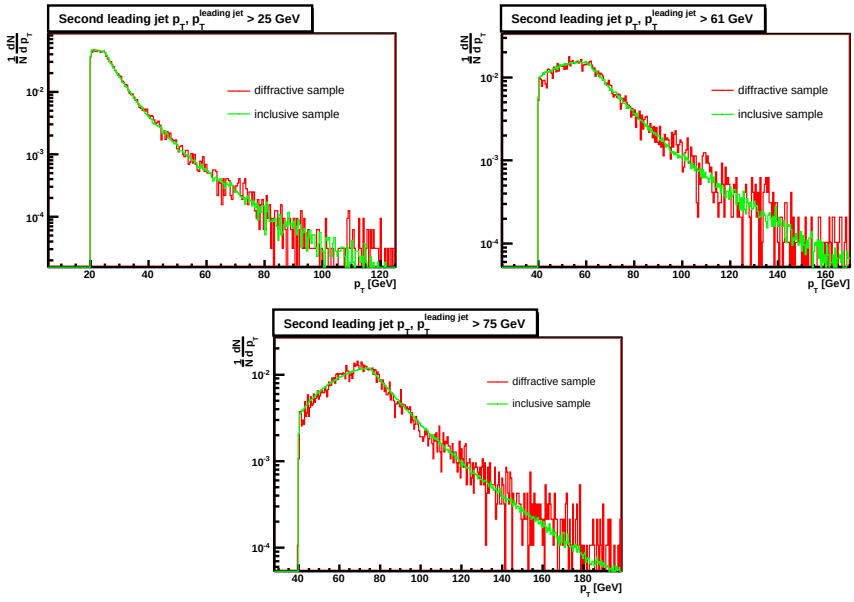

Figure 8.15: The distribution of p_T of the second leading jet in the inclusive and diffractive sample.

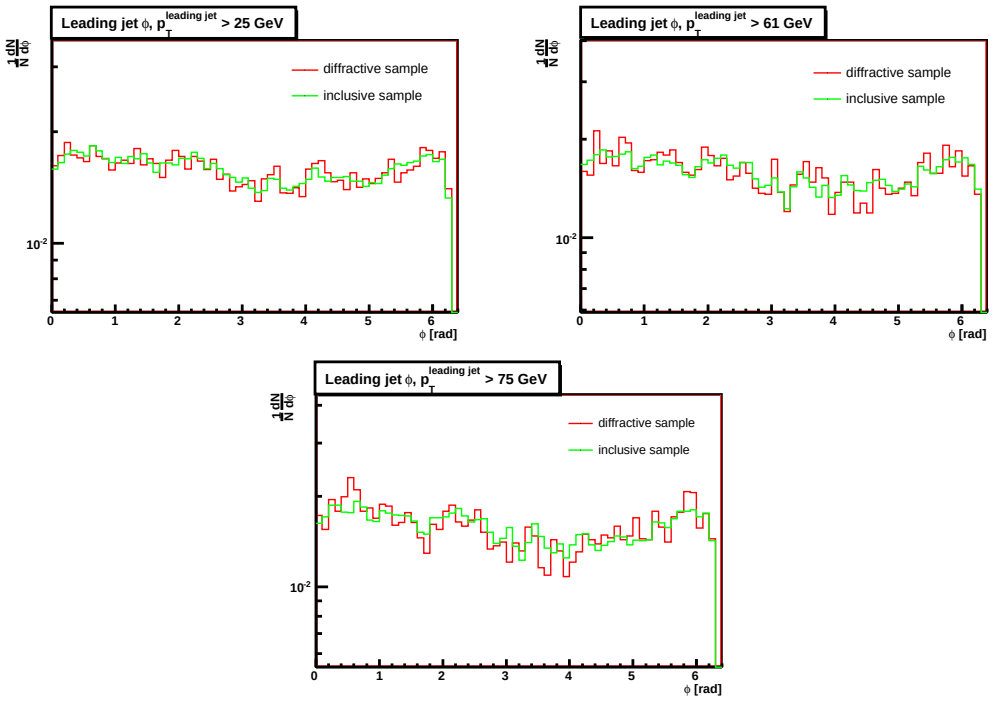

Figure 8.16: The distribution of the azimuthal angle of the leading jet in the inclusive and diffractive sample.

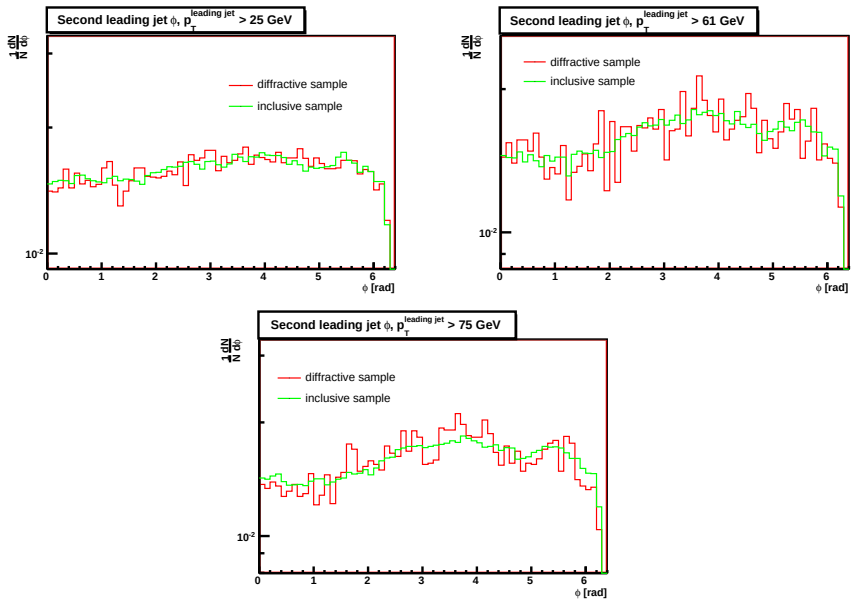

Figure 8.17: The distribution of the azimuthal angle of the second leading jet in the inclusive and diffractive sample.

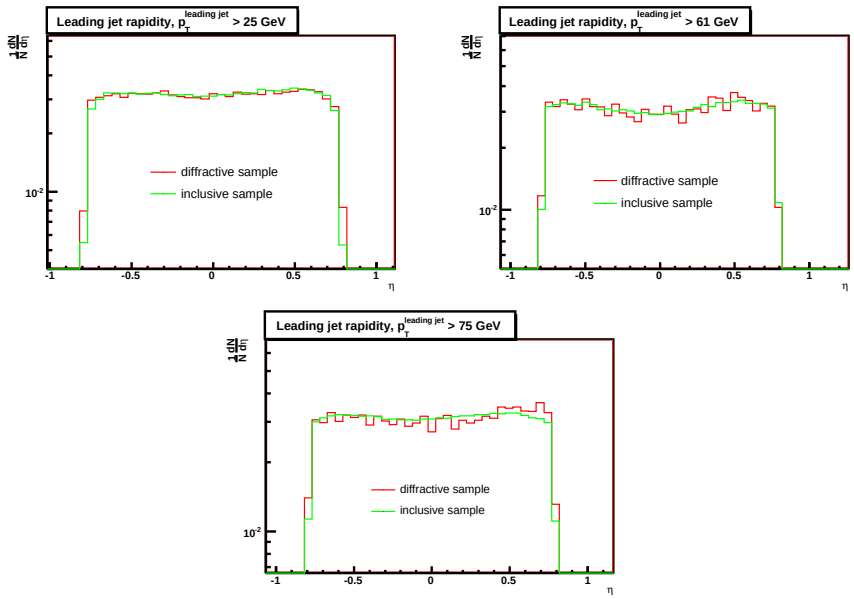

Figure 8.18: The distribution of the pseudorapidity of the leading jet in the inclusive and diffractive sample.

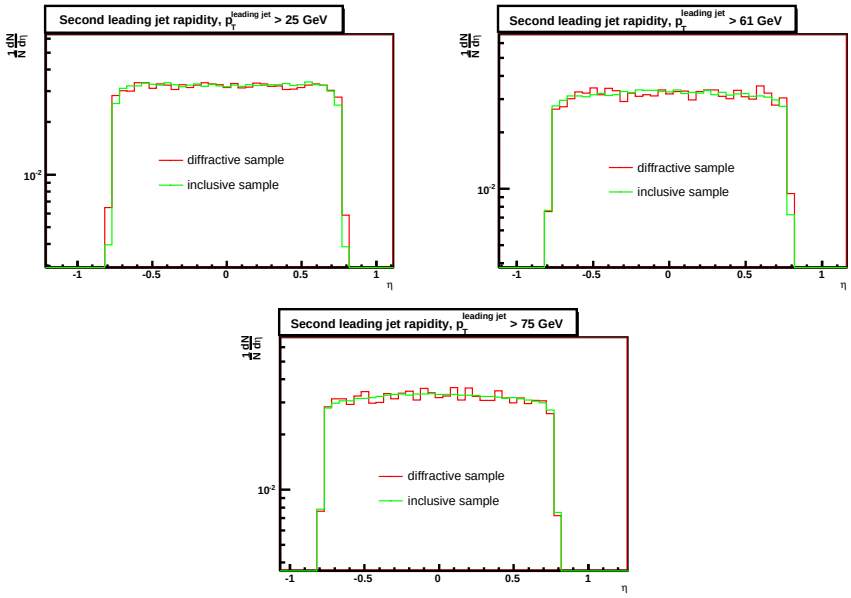

Figure 8.19: The distribution of the pseudorapidity of the second leading jet in the inclusive and diffractive sample.

Chapter 9

Conclusions

As the diffraction theory is still poorly understood, it is important to analyze as many properties of diffractive processes as possible to find the correct description of diffraction. One such measurement was the main goal of this thesis, in which a first analysis of diffractive high p_T central dijet events was presented.

The diffractive processes in this thesis are searched using the rapidity gap approach. Definition of a rapidity gap (or a region of low particle activity) is not uniquely determined, therefore we could have derived two different definitions. Using a first definition, we get a diffractive sample with the lowest systematical errors. A diffractive sample selected by the second definition has the lowest contamination from non-diffractive processes, but there is also a high rejection of diffractive events.

Using the gap definition, the $\Delta\phi$ distribution was precisely analyzed. This variable is sensitive to the inner dynamics of a process and indeed, the main results as seen in previous chapters showed the dependence of this distribution on the type of process. The D0 Run II results on inclusive dijet $\Delta\phi$ measurement presented in [33] were redone in this thesis using a bigger statistical sample. Comparison with diffractive distribution confirmed the different behaviour in diffractive processes. Our measurement is consistent with the previous CDF results on diffractive $\Delta\phi$ measurements [38], where low p_T jets were used.

On top of the $\Delta\phi$ measurement, we have compared the diffractive and inclusive distributions of other variables - dijet mass, azimuthal angle, missing E_T, pseudorapidity, primary vertex properties and jet properties. We can conclude that most of the event and jet properties seem to be similar within the errors for both samples. But there is a remarkable difference in the distributions of n90 variable (number of calorimeter towers which hold 90% of the jet energy) and number of tracks associ-

ated with the primary vertex. This can be understood as that the diffractive jets are narrower as compared to inclusive QCD jets.

It was also shown that distributions of $\Delta\phi$ and other variables depend on the leading jet p_T. Generally, the lower jet p_T, the bigger difference between diffractive and inclusive samples.

Monte Carlo generators Pomwig and Herwig with various input parameters were used to compare the theoretical predictions with the measured properties of diffractive and inclusive data respectively. The results agreed well, but the necessary change in the default Pomwig parameters needs further studies.

Bibliography

[1] T. Regge, Nuovo Cim. 14 (1959) 951

[2] T. Regge, Nuovo Cim. 18 (1960) 947

[3] A. Donnachie and P. V. Landshoff, Phys. Lett. B 296 (1992) 227, arXiv:hep ph/9209205

[4] I. Y. Pomeranchuk, Zh. Eksp. Teor. Fiz. 34 (1958) 725

[5] G. F. P. Chew and S. C. Frautschi, Phys. Rev. Lett. 7 (1961) 394

[6] G. F. P. Chew and S. C. Frautschi, Phys. Rev. Lett. 8 (1962) 41

[7] M. Froissart, Phys. Rev. 123, 1053 (1961)

[8] A. Martin, Nuovo Cim. A42, 930 (1965)

[9] C. Adlo et al. [H1 Collaboration], Nucl. Phys. B 497 (1997) 3 [arXiv:hep . ex/9703012]

[10] J. Breitweg et al., [ZEUS Collaboration], Phys. Lett. B 407 (1997) 432 [arXiv:hepex/9707025]

[11] M. Derrick at al., [ZEUS Collaboration], *Observation of events with a large rapidity gap in deep inelastic scattering at HERA*, Phys. Lett. B 315 (1993) 481

[12] T. Ahmed at al, [H1 Collaboration], *Deep inelastic scattering events with a large rapidity gap at HERA*, Nucl. Phys. B429, 477 (1994)

[13] R. Bonino at al., [UA8 Collaboration], *Evidence for transverse jets in high-mass diffraction*, Phys. Lett. B 211, 239 (1988)

[14] A. Brandt at al., [UA8 Collaboration], *Evidence for a super-hard pomeron structure*, Phys. Lett. B 297, 417 (1992)

[15] A. Donnachie and P. V. Landshoff, Phys. Lett. B 437 (1998) 408 [arXiv:hep f, ph/9806344]

[16] J. D. Bjorken, SLACPUB6949

[17] S. Abatzis et al. [WA91 Collaboration], Phys. Lett. B 324 (1994) 509

[18] *The D0 detector*, Nucl. Instr. and Methods, A338, 185 (1994), FERMILAB-PUB-93/179-E-PS

[19] M. Strang, *First observation of dijet events with an antiproton tag at* $\sqrt{s} = 1.96$ *TeV using the D0 forward proton detector*, PhD. thesis, University of Texas at Arlington, 2005

[20] http://www-bd.fnal.gov/public/chain.html

[21] P. D. B. Collins, *An introduction to Regge theory and high-energy physics*, Cambridge University Press, 1977

[22] A. Kupco, *Measurement and QCD analysis of inclusive dijet mass cross section in* $p\bar{p}$ *collisions at* $\sqrt{s} = 1.96$ *TeV*, PhD. thesis, Charles University, Prague, 2003

[23] T. Edwards, *Diffractively produced Z bosons in the muon decay channel in* $p\bar{p}$ *collisions at* $\sqrt{s} = 1.96$ *TeV, and the measurement of the efficiency of the D0 Run II Luminosity Monitor*, PhD. thesis, University of Manchester, 2005

[24] U. Bassler, G. Bernardi, *Towards a Coherent Treatment of Calorimetric Energies: Missing Transverse Energy, Jets, E.M Objects and the T42 Algorithm*, D0 note 4124, 2002

[25] M.Adams, N.Amos, S. Chopra, at al, *Design Report of the Central Preshower Detector for the D0 Upgrade*, 1996

[26] http://d0server1.fnal.gov/users/qianj/CPS/index.htm, Central Preshower Details

[27] G. C. Blazey, J. R. Dittmann, S. D. Ellis, at al., *Run II Jet Physics*, hep-ex/0005012v2, 2000

[28] J. Huth et al., in E. L. Berger (ed.), *Research Directions for the Decade*, Snowmass 1990, (World Scientific, Singapore, 1992), p. 134

[29] http://www-d0online.fnal.gov/www/groups/cal/how_to_identify_hot_cells.html, D0 private page

[30] http://www-d0.fnal.gov/phys_id/jes/d0_private/jes.html, D0 private page

[31] http://www-d0.fnal.gov/phys_id/jets/jetID_p14_pass2.html, D0 private page

[32] K. Goulianos, *Diffractive interactions of hadrons at high-energies*, Phys. Rept. 101:169, 1983

[33] A. Kupco, M. Begel, P. Demine, et al., *Measurement of dijet azimuthal angle distribution in $p\bar{p}$ collisions at $\sqrt{s} = 1.96$ TeV*, D0 note, 2004

[34] Brian Cox, Jeff Forshaw, *Pomwig: Herwig for Diffractive Interactions*, hep-ph/0010303v3, 2001

[35] A. Kupco, P. Demine and C. Royon, *Jet angular resolutions in the central part of calorimeter for R = 0.7 cone*, D0 Note 4384, 2004

[36] J. - L. Agram and C. Royon, *Jet p_T resolution using JES v05-02-00*, D0 Note 4396, 2004

[37] K. Hatakeyama, *Measurement of the Diffractive Structure Function of the Antiproton in Proton-Antiproton Collisions at $\sqrt{s} = 1800$ GeV and 630 GeV*, PhD. thesis, p. 10

[38] http://www-cdf.fnal.gov/physics/new/qcd/run2/diffractive/diff_bless/run2_diff_bless.html, CDF Run II blessed results on diffractive dijet production